Energy Efficient Position Tracking Control of a Discrete Displacement Cylinder

31th of MAY
2019

BREAKING NEW GROUND
AALBORG UNIVERSITY

10th semester - Master's Thesis
Group MCE4-1023
Mechatronic Control Engineering
Department of Energy Technology

Studienævn for Energi

Title: Energy Efficient Position Tracking Control of a Discrete Displacement Cylinder
Semester: 10th semester
Semester theme: Master's Thesis in Mechatronic Control Engineering
Project period: 02.02.19 to 31.5.19
ECTS: 30
Supervisor: Anders Hedegaard Hansen
Project group: MCE4-1023

Jesper Smidt Philipsen

Mitchell Uhrskov Mateos Amez

SYNOPSIS:

In this thesis a position tracking controller capable of reducing energy losses has been developed. The system this controller is used on is a digital displacement cylinder (DDC) controlled by digital flow control units. The cylinder consist of 3 chambers connected to 3 different leveled pressure lines. Furthermore a hydraulic load cylinder system is connected to the piston of the DDC. A model of the hydraulic system is derived and validated. A real life application case is constructed in order to generate a position reference. A Knuckle Boom crane was chosen for this application case.
The control structure used is a PI controller. The DDC can produce discrete forces and thus the controller output has to be discretized. This is done together with adding a force switch algorithm in order to reduce the energy losses. Three algorithms are tested. The algorithm that showed the best result is a algorithm where the force switch is chosen based on the energy optimal switch within a given force band of 10 kN when sampled with a sampling time off 0.06 s. This reduced the energy loss by 59% compared to a benchmark test.

Printings:	2
Number of pages:	90
Appendices:	4
Supplements:	None

By accepting the request from the fellow students who uploads the study group's project report in Digital Exam System, you confirm that all group members have participated in the project work, and thereby all members are collectively liable for the contents of the report. Furthermore, all group members confirm that the report does not include plagiarism.

Preface

This master thesis is written in the spring of 2019, by project group MCE4-1023 on 10th semester from the Department of Energy Technology at Aalborg University. The software used in this project is:

- *Microsoft Visio* - Illustrations and schematics.
- *MATLAB* - Data analysis and plotting.
- *Simulink* - Modelling and simulation of dynamic systems.
- *LabVIEW* - Running the experiment setup in the laboratory.

Reader's Guide: The literature used in this report encompasses textbooks, web pages, technical reports and note collections. A list of the literature is presented in the bibliography. IEEE Style of referencing has been applied when citing information sources - displaying the citation with a number in squared brackets the source can then be found in the bibliography. If a citation is presented after paragraphs and equations, it covers the section above. If a citation is presented within a sentence, it covers that sentence.

Figures, tables and equations are numbered according to the chapter in question followed by sequential numbers.

A nomenclature list of used symbols, acronyms and constants is presented. The list shows the descriptions and units of the symbols. Unless otherwise is specified, all units are SI-units.

Appendices are included in this report, and are found after the bibliography.

Summary

In this thesis a control strategy for a digital displacement cylinder (DDC) is investigated. The goal of this control strategy is to perform a position tracking while reducing the energy loss of the system.

The DDC used is part of an experiment setup provided by Aalborg University. The setup consist of a three chambered hydraulic cylinder, connected to three pressure lines by nine digital flow control units (DFCU). The cylinder is then connected by a sleigh to a symmetric hydraulic cylinder connected to its own pressure system. The multi-chambered cylinder will be used to control the position of the sleigh while the symmetric cylinder will provide a disturbance force. The way the multi-chambered cylinder is set up increases the difficulty of the control as it is capable of producing 27 discrete output force levels while having nine inputs.

A model of the hydraulic system has been derived in order to be able to design and test different control strategies. The model was validated by conduction experiments and comparing them with the simulation results. It was concluded that model mirrored the real system to a satisfactory degree. Furthermore to be able to design a more realistic disturbance profile and controller reference, a test case based on a real life application was designed. The application case was chosen to be a Knuckle Boom crane and from this a maximum allowable RMS position tracking error was determined to be 0.02 m.

With a model and application case determined, different control strategies could be tested. Two control structures were tested. The first control structure was a linear quadratic controller. This controller was found not to be a viable solution for this system and control problem. The other control structure that was tested was the classical PI controller. This PI controller was designed to have the position error as input and the force as output. The controller was then combined with an algorithm choosing the closest available discrete force to the controller output.

In total four types of algorithms were tested. One where the number of opened valves in each DFCU where varied, this proved not to be useful as it increased the energy cost. Two others where the force switches were optimized, and the last where only the update rate of the algorithm was changed. The three last algorithms all proved as viable options to reduce the energy loss when compared to a benchmark test. The best option was found to be a force switching algorithm where a force band of 10 kN with a sample time of 0.06 s is used. This algorithm chooses the force switch based on the force switch that costs the least amount of energy within the force band. Using this algorithm the total energy loss was reduced by 59% when compared to the benchmark.

Nomenclature

In this nomenclature all constants used in the project are defined. Some of the constants' symbols are defined multiple times, with different meanings. It should be clear from the different chapters and sections, which constant is used.

Acronyms

AAU	*Aalborg University*	
DDC	*Discrete Displacement Cylinder*	
DFCU	*Digital Flow Control Unit*	
HP	*High Pressure*	
LP	*Low Pressure*	
LQC	*Linear Quadratic Controller*	
MISO	*Multiple Input Single Output*	
MP	*Medium Pressure*	
MPC	*Model Predictive Control*	
PWM	*Pulse Width Modulation*	
RMS	*Root Mean Square*	
SISO	*Single Input Single Output*	

Greek symbols

α	Angle in crane model	[deg]
β_a	Bulk modulus of the air	[Pa]
β_{eff}	Effective bulk modulus of the oil	[Pa]
β_F	Bulk modulus of the oil	[Pa]
$\epsilon_{air,0}$	Volumetric ratio of air in oil at atmospheric pressure	[-]
ϵ_{air}	Volumetric ratio of air in oil	[-]
γ_{fric}	Slope for Coulomb friction	[-]

κ	Adiabatic constant	[-]
μ	Viscosity of the oil	[Pa s]
ω_n	natural frequency	$[\frac{\text{rad}}{\text{s}}]$
ρ	Density of the oil	$[\frac{\text{kg}}{\text{m}^3}]$
θ	Joint angle	[deg]
ξ	Loss coefficient	[Pa s]
ζ	Damping coefficient	[-]

Latin symbols

$\ddot{x}_i$	Acceleration	$[\frac{\text{m}}{\text{s}^2}]$
$\dot{P}_i$	Pressure gradient	$[\frac{\text{Pa}}{\text{s}}]$
$\dot{Q}_i$	Flow gradient	$[\frac{\text{m}^3}{\text{s}^2}]$
$\dot{V}$	Volume change	$[\frac{\text{m}^3}{\text{s}}]$
$\dot{x}_i$	Velocity	$[\frac{\text{m}}{\text{s}}]$
$\tilde{u}$	Virtual input	[-]
A_i	Cross-sectional area	[m^2]
B_c	Viscous friction constant	$[\frac{\text{N s}}{\text{m}^2}]$
e	Error	[-]
E_i	Energy	[J]
$F_{Coulomb}$	Coulomb friction constant	[N]
F_e	Force error	[N]
F_i	Force	[N]
$K_{v,i}$	Valve gain	$[\frac{\text{m}^3}{\text{Pa}^{0.5}\text{s}}]$
L	Length of transmission line element	[m]
m_{tot}	Mass of the system	[Kg]
n_i	Number of valves in a DFCU	[-]
NO	Number of switchings	[-]
P_i	Pressure	[Pa]
Q_i	Flow	$[\frac{\text{m}^3}{\text{s}}]$
t_d	Delay	[s]
V_i	Volume	[m^3]
x_{eq}	Equivalent valve input	[-]
x_i	Position	[m]
$x_{v,i}$	Valve input	[-]

List of Figures

1.1 Implementation of a digital four-way valve with switching control. 2
1.2 Working principle of a DFCU. 3
1.3 Implementation of a digital four-way valve with DFCU's. 3
1.4 Different implementation of parallel connected cylinders. 5
1.5 Basic implementation of multi-pressure line system. 5

3.1 Sketch of the experimental setup. 9
3.2 Test setup at AAU facilities. 10
3.3 Test setup at AAU facilities. 10
3.4 Discrete force range profile. 10
3.5 Knuckle Boom crane example [1]. 11
3.6 Example sketch of a Knuckle Boom crane. 12
3.7 Sketch of Knuckle Boom crane focused on first joint. 14
3.8 Sketch of Knuckle Boom crane focused on second joint. 15
3.9 Simplified sketch of a Knuckle Boom crane. 16
3.10 Map of static force for all cylinder positions. 17
3.11 Position trajectory of crane end effector with boundary limits. 18
3.12 Trajectory of crane in cylinder space. 18
3.13 Force profile of trajectory reference. 19

4.1 Sketch of the experimental setup. 21
4.2 Sketch for the primary actuator side. 22
4.3 Sketch of the multi-chamber cylinder. 23
4.4 Block diagram of the valve dynamics for DFCU valves. 25
4.5 Lumped parameter model. 25
4.6 Sketch of the Load subsystem to be modelled. 27
4.7 Block diagram of the valve dynamics for both the Parker and Moog valve. . . . 29
4.8 Frequency response for the Moog valve [2]. 29
4.9 Frequency response for the Parker valve [3]. 29
4.10 Sketch of mechanical system with forces. 30
4.11 Switching loss between different pressure states when x_c = 1 m, P_l = 20 bar, P_m = 100 bar and P_h = 180 bar 32
4.12 Switching loss as a function of x_c when switching between P_l = 20 bar and P_m = 100 bar. 33
4.13 Switching loss for each chamber for different positions and velocities when switching from 180 to 100 bar with T_p = 40 ms. 34
4.14 Throttle loss as a function of sleigh velocity. 35

5.1 Cylinder position for Moog valve using the valve gain from the data sheet. . . . 38
5.2 Cylinder position for Parker valve using the valve gain from the data sheet. . . 38
5.3 Valve gains for the Moog valve used in the look-up table. 38

5.4 Valve gains for the Parker valve used in the look-up table. 38
5.5 Cylinder position for Moog valve with new look-up table. 38
5.6 Cylinder position for Parker valve with new look-up table. 38
5.7 Cylinder velocity for Moog valve at a step of 4 volt. 39
5.8 Cylinder velocity for Parker valve at a step of 1.1 volt. 39
5.9 Load pressure for Moog valve at a step of 3 volt. 39
5.10 Load pressure for Parker valve at a step of 1.3 volt. 39
5.11 Experimental and simulated pressure for Chamber A together with the given input. 40
5.12 Chamber 1 pressure at a step from 20 bar to 100 bar. 41
5.13 Chamber 1 pressure at a step from 100 bar to 20 bar. 41
5.14 Chamber 2 pressure at a step from 100 bar to 180 bar. 41
5.15 Chamber 2 pressure at a step from 180 bar to 100 bar 41
5.16 Chamber 3 pressure at a step from 20 bar to 100 bar. 41
5.17 Chamber 3 pressure at a step from 100 bar to 20 bar. 41
5.18 Chamber 1 pressure right after the manifold. 42
5.19 Chamber 2 pressure right after the manifold. 42
5.20 Chamber 3 pressure right after the manifold. 42
5.21 Position of the cylinder during the DDC experiment. 42

6.1 Load pressure comparison between reduced order model and nonlinear model. . 44
6.2 Velocity comparison between reduced order model and nonlinear model. 44
6.3 Position comparison between linear and non-linear model, with an input of 0.104. 46
6.4 Velocity comparison between linear and non-linear model, with an input of 0.104. 46
6.5 Position comparison between linear and non-linear model, with an input of 0.11. 46
6.6 Velocity comparison between linear and non-linear model, with an input of 0.11. 46
6.7 Block diagram for the load side control system. 47
6.8 Open loop bode diagram for the uncompensated system. 48
6.9 Reference tracking of the closed loop system with a controller gain of one. . . . 49
6.10 Reference load pressure and actual load pressure of the system using the designed controller. 49

7.1 Trajectory of crane in cylinder space. 51
7.2 LQC tracking result. 53
7.3 LQC controller inputs. 53

8.1 Block diagram of force control concept. 55
8.2 Bode diagram of the uncompensated system. 56
8.3 Bode diagram of system with P compensator. 57
8.4 Bode diagram of system with PI compensator. 57
8.5 Continuous force reference with available discrete forces. 57
8.6 Tracking result for P controller, $e_{RMS} = 0.236$ m. 58
8.7 Tracking result for PI controller, $e_{RMS} = 0.028$ m. 58
8.8 Comparison between old and tuned controller. 59
8.9 Force Band Algorithm with a force band of 75 kN. 61
8.10 Bar plot showing total energy loss and RMS error for different sample times. . 62
8.11 Bar plot showing total switching loss and number of switches for different sample times. 62
8.12 Comparison of velocity for a sample time of 0.08 s and 0.16 s. 62
8.13 Comparison of output force for a sample time of 0.08 s and 0.16 s. 62
8.14 Bar plot showing total energy loss and RMS error for different sample times. . 63

8.15 Bar plot showing total switching loss and number of switches for different sample times. 63
8.16 Bar plot showing total energy loss and RMS error for different sample times. . 63
8.17 Bar plot showing total switching loss and number of switches for different sample times. 63
8.18 Bar plot showing total energy loss and RMS error for different force bands. . . 64
8.19 Bar plot showing total switching loss and number of switches for different force bands. 64
8.20 Bar plot showing total energy loss and RMS error for different sample times. . 65
8.21 Bar plot showing total switching loss and number of switches for different sample times. 65
8.22 Comparison of velocity for a sample time of 0.08 s and 0.12 s. 65
8.23 Comparison of output force for a sample time of 0.08 s and 0.12 s. 65
8.24 Cylinder chamber pressures. 66
8.25 Bar plot showing total energy loss and RMS error for different sample times. . 66
8.26 Bar plot showing total switching loss and number of switches for different sample times. 66
8.27 Bar plot showing total energy loss and RMS error for different sample times. . 67
8.28 Bar plot showing total switching loss and number of switches for different sample times. 67
8.29 Comparison of tracking abilities for the two force shifting algorithms. 67
8.30 Tracking result of different algorithms. 68
8.31 Position error of different algorithms. 68
8.32 Zoomed version of tracking result for the different algorithms. 68
8.33 Output force of different algorithms. 68

9.1 Velocity of the benchmark together with velocity reference. 69
9.2 Block diagram for the control system with force controller and valve switching algorithm. 70
9.3 Benchmark velocity compared to Velocity using Minimum valve algorithm. . . . 71
9.4 Benchmark velocity compared to Velocity using Switch valve algorithm. 71
9.5 RMS position error caparison for the new algorithms. 71
9.6 Throttling loss for the new algorithms. 71

A.1 Calculated valve gains for the Moog valve and the mean valve gains. 80
A.2 Calculated valve gains for the Parker valve and the mean valve gains. 80

C.1 Data-points together with the polynomial fit for the Moog valve. 86
C.2 Data-points together with the polynomial fit for the Parker valve. 86
C.3 Inputs to both the Parker and Moog valve as a function of the equivalent input. 86
C.4 Valve gains as a function of the equivalent input and individual inputs. 86

D.1 LQC tracking result. 90

D.2 LQC controller inputs. 90

List of Tables

1.1 Binary coded combination table with three valves. 4
1.2 PNM coded combination table with three valves. 4

8.1 Control parameters. 57
8.2 Energy loss, tracking error and number of switches for designed controller . . . 59

B.1 DDC side parameters. 81
B.2 General parameters. 82
B.3 Load side parameters. 82
B.4 Transmission line parameters. 83

Contents

Summary **v**

1 Introduction **1**
1.1 Digital valves . . . 1
1.2 Parallel Connected Cylinders and Multiple Pressure Lines . . . 4

2 Problem Statement **7**

3 System Description **9**
3.1 Test Case . . . 11

4 Model **21**
4.1 Digital Displacement cylinder subsystem . . . 22
4.2 Load subsystem . . . 27
4.3 Mechanical movement . . . 30
4.4 Energy losses . . . 31

5 Validation of Model **37**
5.1 Load side validation . . . 37
5.2 DDC side validation . . . 40

6 Load side controller **43**
6.1 Reduced order model . . . 43
6.2 Linear Load model . . . 45
6.3 Controller design . . . 46

7 Control Considerations **51**
7.1 System Considerations . . . 52
7.2 Control Strategy . . . 52

8 Force controller **55**
8.1 Design of the controller . . . 55
8.2 Switching Algorithms . . . 59
8.3 Results . . . 62

9 Valve switching algorithm **69**

10 Conclusion **73**

11 Future works **75**

Bibliography **77**

Appendix A Valve Gain Experiments **79**

Appendix B Model Parameters **81**

Appendix C Valve Splitting Algortihm **85**

Appendix D LQC design for the Digital Displacement Cylinder **87**

1 Introduction

In the heavy machine industry, hydraulic systems are popular as an actuation solution due to the high power to size ratio that is achievable using such system [4]. The electrical counterparts often has to rely on large gear ratios in order to achieve the same power which are more prone to failures. The hydraulic systems used today are conventionally controlled using proportional valves, that with the use of throttling achieve the desired motion control performance. This throttling of the flows in and out of the cylinder chambers is a source of loss due to low efficiency at part loads [5].

Due to this low efficiency at partial loads digital hydraulics has been receiving attention, in the attempts to improve the system efficiency by assuring that the hydraulic components operates at peak efficiency, even with changing pressures and partial loads. There are a number of ways of implementing digital hydraulics in a fluid power system. Digital valves, parallel connected cylinders and multiple pressure lines are some of the more common setups [6]. Research has been made in all these concepts and shown improvement in efficiency when comparing to the traditional hydraulic system. A digital hydraulic system will almost always consist of digital on/off valves making this the key component, however parallel connected cylinders or secondary control systems has been designed using proportional valves intended to work as on/off valves. A description of the three options will be given in the following sections.

1.1 Digital valves

In a digital hydraulic system the traditional proportional valves are replaced with individually controlled fast acting on-off valves. The advantages of using these digital on/off vales compared to the proportional valves is that they are fast acting and leak free, more reliable and flexible due to programability options [6]. The functionality of digital valve systems is created by software and can be updated for the purpose of the application. This means that the same digital valve type can be used as a directional valve, pressure relief valve, flow control etc. depending on software control code. This limits the number of different components needed to "copy" an analog solution of the same system. This could make the production of the system easier and cheaper due to the possibility of mass production.

As each valve can work and be controlled independently of each other the digital hydraulic systems are considered flexible. This individuality makes it possible to work with arbitrary flow values effectively, thus having good efficiency at partial loads.

A state of the art digital on/off valve has an switching time of 2 ms [7] and as mentioned the same valve type can be used for almost any application improving the overall system response time.

A disadvantage of the digital valve is that the control of the valve is more complex when compared to traditional proportional valves. Where proportional valves can be seen as continuous when controlling it [6,p.28] is more discrete in nature. The complexity of controlling digital valves is depending on how many digital valves are used and the function that the valves are trying to emulate. With a rising amount of digital valves the complexity of the needed control also increases. The reason for this is that different combinations, also called states, of the valves can result in the same performance of the system. There are two common ways of incorporating digital valves in a hydraulic system. One is parallel connection, where multiple connected valves are placed in parallel, and the other is using switching technologies.

Switching Digital Valves

A picture of a PWM switching on/off valve system representing a traditional 4/3 valve can be seen in Figure 1.1.

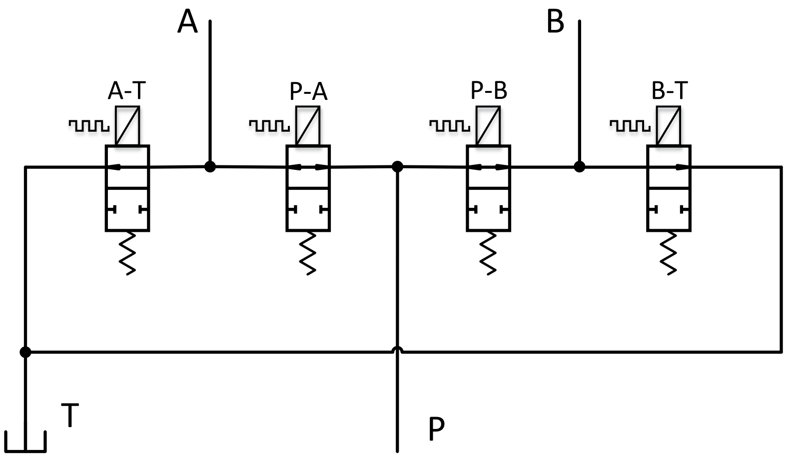

Figure 1.1: Implementation of a digital four-way valve with switching control.

When controlling a valve using switching the output is controlled by fast and continuous switching modulation techniques such as pulse width modulation (PWM) adjusting the duty cycle to adjust the output. Using switching technology to control the actuating valves will require fewer components compared to parallel connected systems and the output will approach a continuous signal. The drawbacks of the switching valve is the large number of switches required to approach a continuous signal which would add mechanical fatigue and maybe reduce lifetime of the valve.

Parallel Connected Digital Valves

The other possibility is parallel connected valves where a valve block is composed of multiple parallel connected on/off valves. This structure is also usually called a digital flow control unit (DFCU). A schematic representation of a DFCU can be seen in Figure 1.2 and how to implement a similar function of a conventional 4/3 valve can be seen in Figure 1.3.

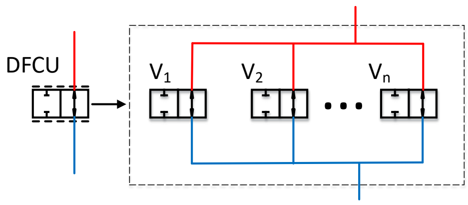

Figure 1.2: Working principle of a DFCU.

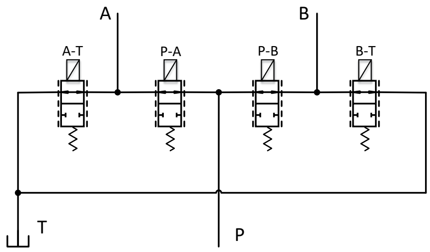

Figure 1.3: Implementation of a digital four-way valve with DFCU's.

With DFCU's the output is controlled by changing whether each individual valve is in its on or off state, which will generate a number of discrete output values. An advantage of parallel connection is that no switching is needed to maintain its state, switching is only required when switching from "on" to "off" or "off" to "on" which reduces mechanical fatigue compared to the PWM control.

The total flow through one DFCU is the sum of the flow through each individual open valve in the DFCU block. An important factor on the steady state flow is the coding scheme of the DFCU. There are different ways of coding the DFCU, the most common method is binary coding [6]. For the binary coding scheme the flow capacities are doubled for every valve, meaning that the flow ratio is 1:2:4:8. Another less common method of coding the DFCU is the pulse number modulation(PNM) where each valve opening has the same size (1:1:1:1). Both method result in the DFCU being scaleable as the total flow can be increased by adding more valves.

Regardless of the selected coding method a DFCU has 2^n opening combinations or states. With binary coding each state has a different flow capacity compared to PNM where some redundant states exist. A combination table using three valves in one DFCU can be seen in table 1.1 and 1.2. Note that the states for both coding schemes are the same, and only the output flow is different. Normally the redundant states in the PNM coding i.e. states that gives the same output flow, are omitted but they are shown here for explanatory purposes.

Valve 1, Q	Valve 2, Q	Valve 3, Q	Net flow
0	0	0	0
1	0	0	1xQ
0	1	0	2xQ
1	1	0	3xQ
0	0	1	4xQ
1	0	1	5xQ
0	1	1	6xQ
1	1	1	7xQ

Table 1.1: Binary coded combination table with three valves.

Valve 1, Q	Valve 2, Q	Valve 3, Q	Net flow
0	0	0	0
1	0	0	1xQ
0	1	0	1xQ
1	1	0	2xQ
0	0	1	1xQ
1	0	1	2xQ
0	1	1	2xQ
1	1	1	3xQ

Table 1.2: PNM coded combination table with three valves.

In the table the net flow for each case is shown, Q is the total flow through the smallest valve, which means that if the 3 valves are on, indicated by a "1", the net flow would be either 7 or 3 times Q depending on the scheme. This means that in order to achieve the same resolution as with binary using PNM a larger number of valves are needed. I.e. in order to achieve the same net flow as 3 valves using binary coding, 7 valves would be necessary. The advantage of using PNM instead of binary is that it reduces undesired pressure peaks. Pressure peaks arises when the switching time of the on/off valves are inconsistent. If some valves closes or opens before the next one, a short period of undesired flow error occurs, which could cause a pressure peak. When switching states using binary some valves are closed and others opened and if the switching times are not exact the output is unpredictable during the period where the switching happens. With PNM to switch from one state to another a valve is either closed or opened which eliminates the transient uncertainty and thus reduces the risk of these pressure peaks [8].

Another benefit of using parallel connected valves is that it introduced a feature of being fault tolerant and thus more reliable. In most cases if one valve break the system will still function with slightly reduced performance. Here PNM coded DFCUs are also more fault tolerant compared to binary which due to the scaling factors of the valves.

1.2 Parallel Connected Cylinders and Multiple Pressure Lines

Parallel connected cylinders is another approach of implementing digital hydraulics. An easy way to achieve such system is by connecting multiple cylinders in parallel however more compact solutions exist with more integrated cylinder chambers added in one cylinder. Some different methods of implementing a parallel connected cylinder system can be seen in Figure 1.4.

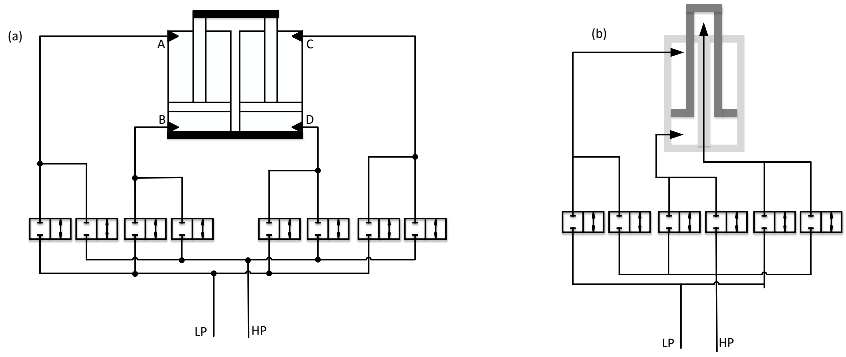

Figure 1.4: Different implementation of parallel connected cylinders.

From the figure (a) is a parallel connected cylinder using two individual cylinders and (b) is a compact solution with a multi-chambered cylinder. Combining a multi-chambered cylinder with on/off valves will result in a discrete number of force outputs depending on the valve state combination. The number of chambers will contribute to the number of discrete force outputs, more chambers equals higher resolution. Multi-chambered cylinder systems has proven to have a much higher efficiency compared to conventional hydraulic setups [9]. One challenge with digital hydraulic cylinder actuators is the compressibility losses that are occurring when the chambers are pressurized and de-pressurized. The loss occurs due to the pressure difference when the chamber pressure is switching from either HP to LP or LP to HP. These losses would not occur if no pressure difference between HP and LP are present, hence increasing the number of different pressure lines would minimize loss [10]. More pressure lines would equal smaller pressure drop, which would lower the losses. A simple diagram of how a multi-pressure system, can be seen in Figure 1.5.

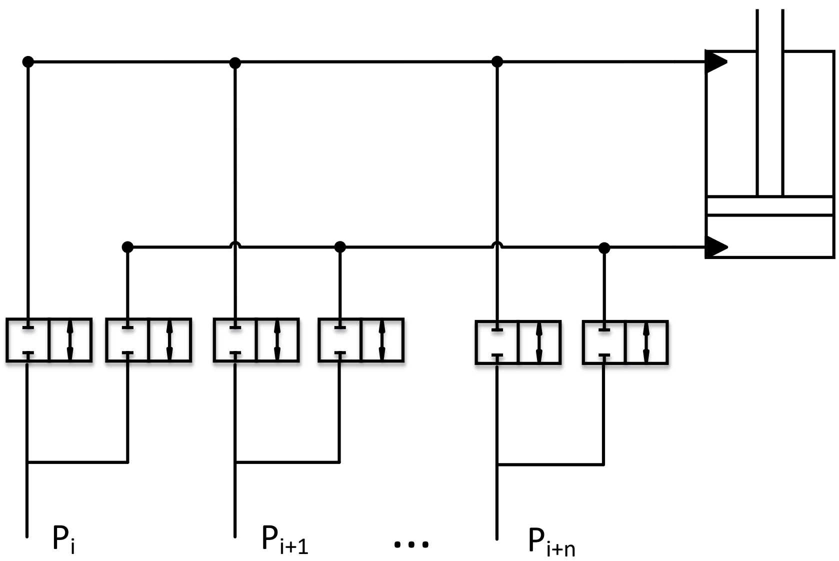

Figure 1.5: Basic implementation of multi-pressure line system.

Ideally having infinitely many pressure lines would result in close to no losses. Creating different pressure levels efficiently is complicated and therefore systems with many different pressure lines are not often seen. In [10] a system with three pressure lines has been studied showing that the efficiency of using three pressure lines is much more efficient compared to conventional hydraulic systems.

To summarize the benefits of using digital hydraulics compared to convectional hydraulics are.

- Simple and reliable components
- Higher degree of flexibility and programmability
- Better performance because of faster valves
- Better energy efficiency

One of the challenges with digital hydraulics is the complicated control that are often required. As already mentioned having many parallel connected valves would add multiple input/output connections which increase the complexity. Multiple input/output system allows many different control possibilities in regards to the control scheme that are used to control the on/off valves [11]. Therefore if proper energy efficient control of such system could be applied the overall efficiency of digital hydraulics could be improved even further when comparing to conventional methods. A lot of investigation is focused on this task. The goal when controlling digital on/off valves connected in parallel is to find the best possible opening combination for each time the controller samples to achieve optimal control. Different approaches have already been made where model predictive control is a popular choice [6,p.139]. But as such system as mentioned is composed of multiple input output combinations other control methods could turn out to be equally efficient. Trying to find the best possible combination of valve openings will always be a compromise between the tracking error and energy consumption.

This thesis will investigate how to improve the reduce energy losses of a digital hydraulic system by testing different control methods. At Aalborg University (AAU) there is a setup composed of a multi-chambered cylinder, with three chambers and three connected pressure levels controlled by multiple DFCU's. The objective will be to design and apply a control structure for a position controller that potentially is able to minimize energy cost.

2 | Problem Statement

As stated in Chapter 1 the goal of this thesis is to design a position controller that also reduces energy losses in the system. This leads to the following problem statement

How can a position controller be designed in order to reduce energy losses without compromising performance for a digital flow control unit (DFCU) controlled multi-chamber cylinder?

Methodology

In order to answer the problem statement of how a position controller can be designed firstly a application system in which the multi-chambered cylinder is a part of is defined. The system chosen will be to simulate a real life application and to help define both control performance and system disturbances. Therefore a Knuckle Boom crane will be looked into as it fits such a hydraulic system. From this crane a system requirement in regards to the allowable position error is achieved. This error are found from the crane industry and for the cylinder used in this thesis the maximum allowable error is $\pm$ 0.02 m.

When a system has been defined a model of the experimental setup from AAU will be developed. This model will contain cylinder, hoses and pipe lines and modelling of the DFCU on/off valves. Furthermore this modelling will also include the hydraulic energy losses of the system. The model is then validated by performing and comparing experimental test made on the physical system to simulations of the developed model.

Lastly the different control strategies will be described, developed and tested theoretically before being compared to find the best suitable energy efficient solution answering the problem statement.

3 System Description

As mentioned in Chapter 1 there is a test setup located at the AAU facilities, capable of testing different control strategies for a digital hydraulic system, with a multi-chambered cylinder and multiple pressure lines. This system was mainly designed to test Power Take Off for a Wave Energy Converter but can be used in a number of other hydraulic applications, such as hydraulic cranes. The idea and thought process behind the design can be found in [12], and only the main components will be presented and described. From [12] the only difference between the designed system and current system is the valves used in the manifold. These valves are now DFCU's using a PNM coding scheme instead of proportional valves.

A simplified schematic of the setup can be seen in Figure 3.1

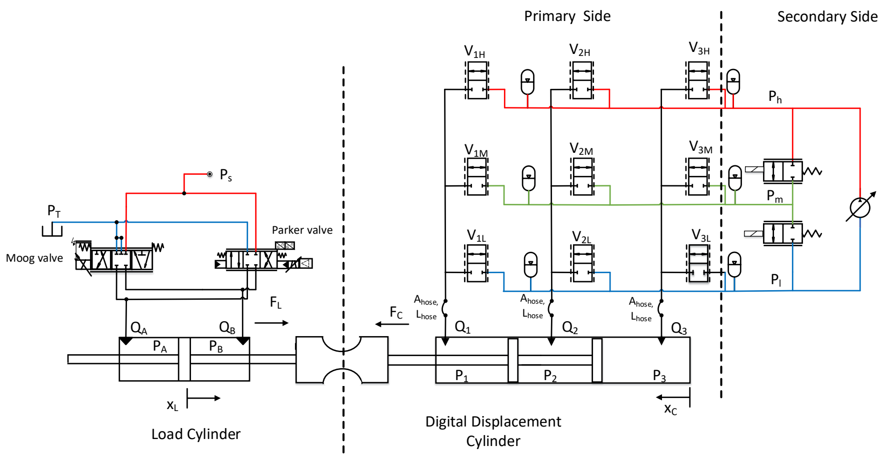

Figure 3.1: Sketch of the experimental setup.

The hydraulic system consist of two opposing cylinders connected by a sleigh. On one side a multi-chamber cylinder combined with three pressure lines is placed. The multi-chamber cylinder consist of five chambers where two chambers are connected in parallel to form one chamber and another chamber is connected to air at atmospheric pressure. This makes the cylinder an operational three chambered discrete displacement cylinder (DDC). The other side consist of a symmetric hydraulic cylinder controlled by two proportional valves. A picture of the test bench placed at the AAU facilities can be seen in Figures 3.2 and 3.3.

Figure 3.2: Test setup at AAU facilities.

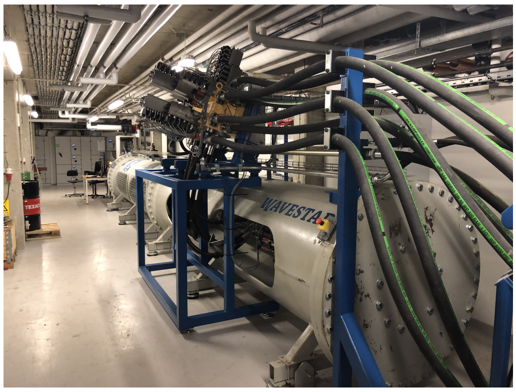

Figure 3.3: Test setup at AAU facilities.

The DDC system is divided into a primary and secondary side. On the primary side the multi-chambered cylinder is placed with the three operating chambers sized to be able to deliver approximately same absolute force in both directions, which is approximately 380 kN when operating with 180 bar of high pressure. The cylinder has a total stroke length of 2 m, however at each end approximately 0.2 m from the end stop a software implemented damping procedure will commence stopping the system to avoid hammer effects and potential damage. The effective operative stroke length is thus 1.6 m. The chambers are connected to the three different pressure levels controlled by a manifold with nine DFCU's all consisting of Bucher WS22GDA-10 on/off valves. For each chamber three DFCU's (one for each pressure level) is connected. The number of valves in each DFCU is sized to match the flow areas of the entire cylinder meaning the flow capacity in and out of each side of the cylinder are approximately the same, in order to have symmetrical velocity profile. Therefore the three DFCU's connected to chamber 1 consist of 18 valves, the three DFCU's connected to chamber 2 and 3 consist of 10 and 8 valves each, respectively. As there is three pressure levels combined with three chambers this will result in $3^3 = 27$ available discrete force outputs. The force range profile of the system can be seen in Figure 3.4.

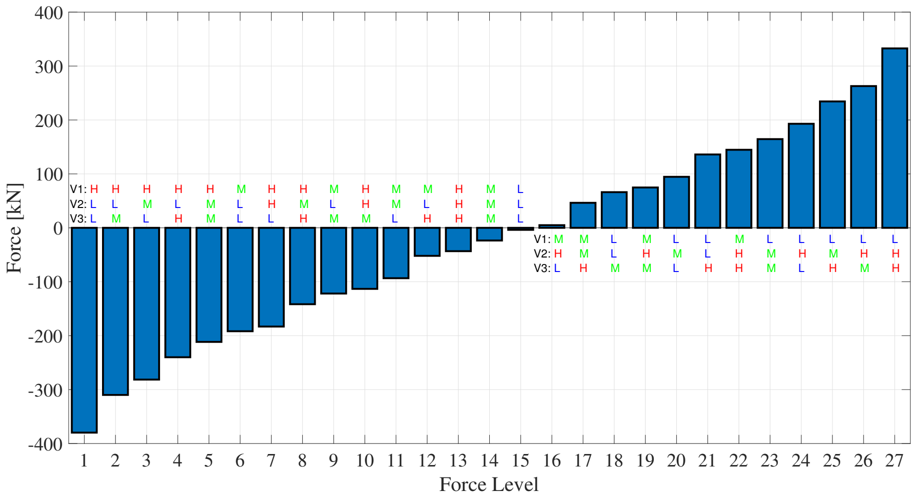

Figure 3.4: Discrete force range profile.

The secondary side of the DDC system is consisting of variable displacement pump/motor designed to supply the three pressure lines with constant pressure levels. The pump is connected to high and low pressure while the mid pressure level is created by two proportional valves connected in between the high and low pressure line. Each line have an accumulator connected with an capacity of 25 L to reduce undesired pressure peaks mentioned in the introduction. The DDC system is also containing 2-4 m of transmission lines between the manifold to the cylinder as the manifold is mounted externally on the tube so components can be easily accessed.

The load side cylinder is a symmetrical cylinder which has a stroke length of 3 m, the center is however aligned with the center of the DDC which means the cylinder never will reach its end stop (unless its due to a rupture). The flow is controlled by two different 4/3 proportional valves in parallel. One is a Parker D111FP which has a rated flow of 1000 L/min at 5 bar and an overlap of 10 % around the center. To compensate for the overlap the other valve is a Moog D634 with a rated flow of 100 L/min at 35 bar. The supply pressure is created by two variable displacement pumps and is furthermore fitted with two accumulators of 28 L.

3.1 Test Case

In order to evaluate the developed controllers a real life scenario is desired as the true potential is more comparable. Therefore a application system such as a knuckle boom crane has been looked into. Knuckle boom cranes are a popular choice in the offshore machine industry and are characterized by its high force a and low speed operation. It is thus seen as a good match for such a hydraulic cylinder system. A picture of a knuckle boom crane can be seen in Figure 3.5.

Figure 3.5: Knuckle Boom crane example [1].

Some data from a real offshore crane has been provided, however the used cylinders are able to sustain 1000 kN which can not be achieved using the cylinders available on the experimental setup used in this thesis. Therefore the crane has been scaled down and some of the variables has been fitted with imaginary numbers, such that the produced forces for the test case can be achieved by the experimental setup. This means that the crane model can not be validated but it will still somewhat simulate a real application as most of the parameters are down scaled and not generated entirely from a imaginary case. A model of the crane system has to be set up to calculate the force profile of the crane. A sketch of a crane could be as depicted in Figure 3.6.

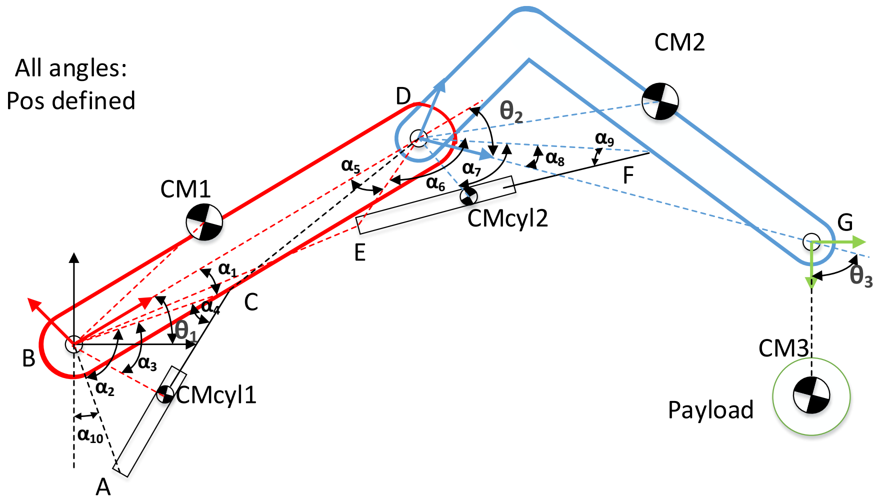

Figure 3.6: Example sketch of a Knuckle Boom crane.

In this section a crane model for the sketched crane will be derived. the purpose of this model is twofold. Firstly to derive a realistic working movement for the crane for the cylinders. Secondly to derive a disturbance force profile, that can be used during the position control. As the crane consist of 2 links with 2 revolute joints, a payload and 2 cylinders the system can be seen as a system with 5 different center of masses (CM's) all moving relatively to each other. As the crane model is only used as a disturbance model only the static force generated by the crane at different positions will be of concern. In the sketch in Figure 3.6 two cylinders are present in the system, however in this thesis only one cylinder will be of concern. The cylinder of concern will be the first cylinder connected to the first link. A force map will be generated while changing attack angles of both links as the needed force of the concerned cylinder is affected by this.

The crane is modeled by describing the positions of the CM's in relation to the joint angles of the system $\theta_1, \theta_2, \theta_3$. To describe a CM the rotational matrix from the global reference frame located in point B is multiplied with the length vector to the respective CM. Each CM's position can be described as Eq. 3.1

$$\boldsymbol{P_{CM1}} = \boldsymbol{R_1 L_1}, \quad \boldsymbol{P_{CM2}} = \boldsymbol{R_1 L_2} + \boldsymbol{R_2 L_3}, \quad \boldsymbol{P_{CM3}} = \boldsymbol{R_1 L_2} + \boldsymbol{R_2 L_4} + \boldsymbol{R_3 L_5}$$
$$\boldsymbol{P_{CM_{cyl1}}} = \boldsymbol{R_4 L_6}, \quad \boldsymbol{P_{CM_{cyl2}}} = \boldsymbol{R_1 L_2} + \boldsymbol{R_5 L_7} \tag{3.1}$$

Where:

$\boldsymbol{L_i}$	is length vector	$[m]$
$\boldsymbol{R_i}$	is the rotational matrix	[m]
$\boldsymbol{P_{CM,i}}$	is the position describing the i'th C	[m]

Here the rotational matrices are given by:

$$
\begin{aligned}
\boldsymbol{R_1} &= \begin{bmatrix} \cos\theta_1 & -\sin\theta_1 \\ \sin\theta_1 & \cos\theta_1 \end{bmatrix} \\
\boldsymbol{R_2} &= \begin{bmatrix} \cos\theta_1+\theta_2 & -\sin\theta_1+\theta_2 \\ \sin\theta_1+\theta_2 & \cos\theta_1+\theta_2 \end{bmatrix} \\
\boldsymbol{R_3} &= \begin{bmatrix} \cos\theta_1+\theta_2+\theta_3 & -\sin\theta_1+\theta_2+\theta_3 \\ \sin\theta_1+\theta_2+\theta_3 & \cos\theta_1+\theta_2+\theta_3 \end{bmatrix} \\
\boldsymbol{R_4} &= \begin{bmatrix} \cos\theta_1-\alpha_3-\alpha_1 & -\sin\theta_1-\alpha_3-\alpha_1 \\ \sin\theta_1-\alpha_3-\alpha_1 & \cos\theta_1-\alpha_3-\alpha_1 \end{bmatrix} \\
\boldsymbol{R_5} &= \begin{bmatrix} \cos\theta_1+\theta_2-\alpha_{10}+\alpha_2 & -\sin\theta_1+\theta_2-\alpha_7+\alpha_8 \\ \sin\theta_1+\theta\_\alpha_7+\alpha_8 & \cos\theta_1+\theta_2-\alpha_7+\alpha_8 \end{bmatrix}
\end{aligned}
\tag{3.2}
$$

Similarly the length vectors can be described as:

$$
\begin{aligned}
&\boldsymbol{L_1} = \begin{bmatrix} L_{B,CM1_x} \\ L_{B,CM1_y} \end{bmatrix}, \boldsymbol{L_2} = \begin{bmatrix} L_{B,D} \\ 0 \end{bmatrix}, \boldsymbol{L_3} = \begin{bmatrix} L_{D,CM2_x} \\ L_{D,CM2_y} \end{bmatrix}, \boldsymbol{L_4} = \begin{bmatrix} L_{D,G} \\ 0 \end{bmatrix} \\
&\boldsymbol{L_5} = \begin{bmatrix} L_{G,CM3} \\ 0 \end{bmatrix}, \boldsymbol{L_6} = \begin{bmatrix} L_{B,CMcyl1} \\ 0 \end{bmatrix}, \boldsymbol{L_7} = \begin{bmatrix} L_{D,CMcyl2} \\ 0 \end{bmatrix},
\end{aligned}
\tag{3.3}
$$

As only the static forces will be considered only the force created by the potential energy due to gravity, will be affecting the system. The general equation of potential energy is $\mathcal{P} = MgH$, when related to the CM's of the crane the potential energy of the system is given by Eq. 3.4.

$$
\begin{aligned}
&\mathcal{P} = \boldsymbol{g}^T \left(\boldsymbol{P_{CM1}} \cdot m_1 + \boldsymbol{P_{CM2}} \cdot m_2 + \boldsymbol{P_{CM3}} \cdot m_3 + \boldsymbol{P_{CM_{cyl1}}} \cdot m_{cyl1} + \boldsymbol{P_{CM_{cyl2}}} \cdot m_{cyl2}\right), \\
&\boldsymbol{g} = \begin{bmatrix} 0 & g \end{bmatrix}
\end{aligned}
\tag{3.4}
$$

In the above listed equations the expressed symbols are denoting:

$L_{i,j}$	Distance from point i to j	[m]
m_i	Mass of links, cylinders or payload	[kg]
θ_i	Rotation angle of the different revolute joints	[rad]
α_i	Different angles of the crane (Illustrated in Figure 3.6)	[rad]

In order to describe the force in actuator space the piston position needs to be related to the joint angles. The relation between force and piston position in the two joints actuated by a cylinder can be found by simple trigonometric calculations. For the payload angle, θ_3 the calculations requires a bit more use of trigonometry as the angle should be related to both cylinder positions. By looking at the triangle composed of the first cylinder actuator and the first revolute joint (ABC), seen in Figure 3.7, it can be seen that θ_1 can be defined as in Eq. 3.5.

$$\theta_1 = \alpha_1 + \alpha_2(x_{c1}) + \alpha_{10} - \pi/2 \tag{3.5}$$

where:

x_{c1} Is the piston position of cylinder 1 [m]

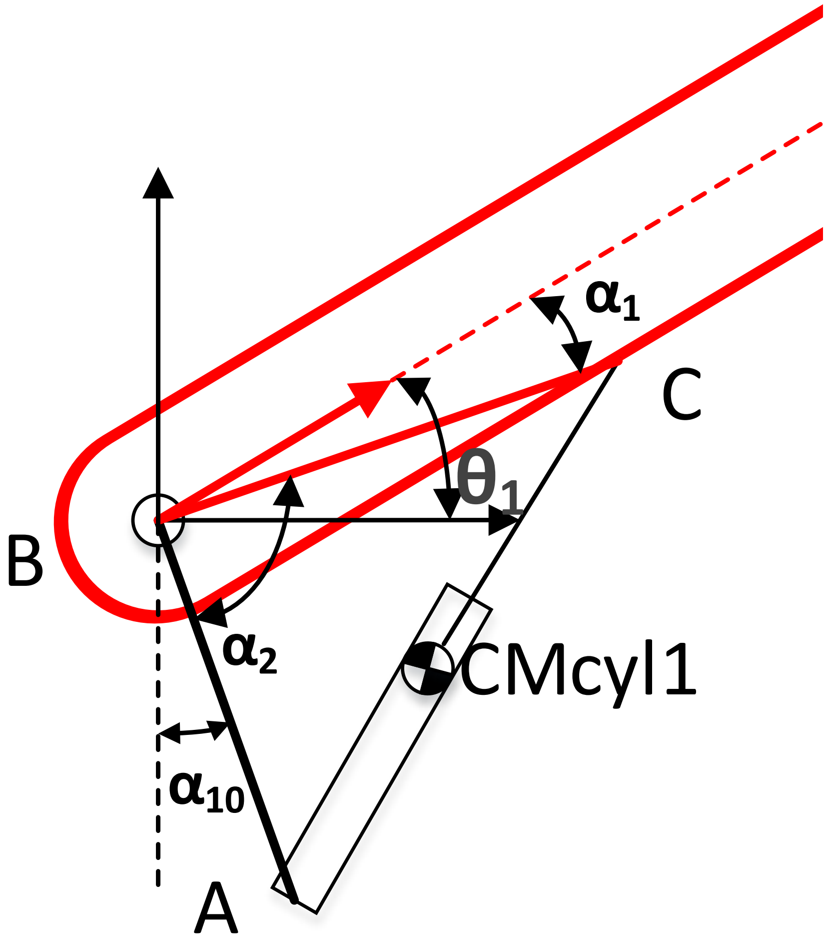

Figure 3.7: Sketch of Knuckle Boom crane focused on first joint.

The angle α_2 can be found by using the cosine relation in the triangle. It can be expressed as in Eq 3.6.

$$\alpha_2 = \cos^{-1}\left(\frac{BA^2 + BC^2 - AC(x_{c1})^2}{2BA \cdot BC}\right) \tag{3.6}$$

The length AC is composed of the minimum length of the cylinder (fully retracted) plus the extension.

Using the same approach to define θ_2 the sketched triangle (DEF) depicted in Figure 3.8 can be used.

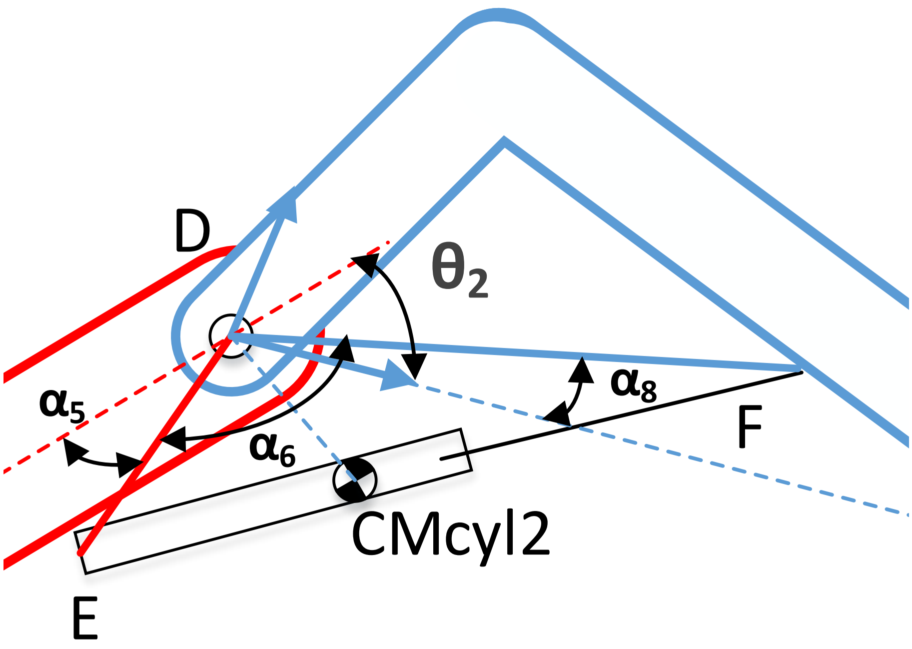

Figure 3.8: Sketch of Knuckle Boom crane focused on second joint.

It can be seen that θ_2 can be defined as:

$$\theta_2 = \alpha_6(x_{c2}) + \alpha_5 - \alpha_8 - \pi \tag{3.7}$$

Again using the cosine relation the angle α_6 can be found.

$$\alpha_6 = \cos^{-1}\left(\frac{DE^2 + DF^2 - EF(x_{c2})^2}{2DE \cdot DF}\right) \tag{3.8}$$

In order to define θ_3 as a function of the piston position of the two cylinders the simple sketch of the crane depicted in 3.9 can be used.

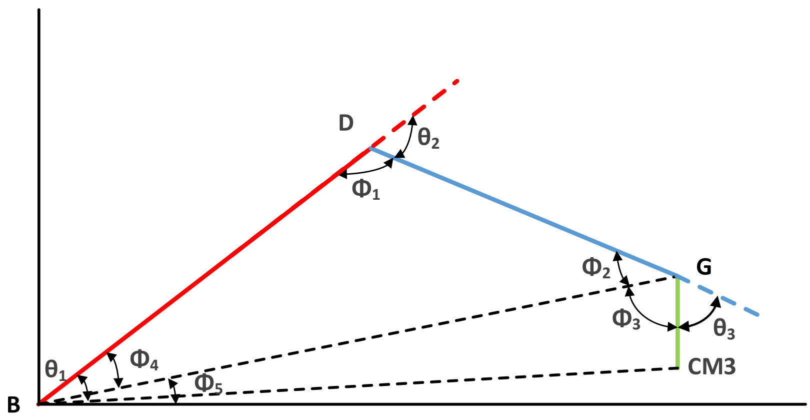

Figure 3.9: Simplified sketch of a Knuckle Boom crane.

Knowing that the angle ϕ_1 will always be equal to $180 - \theta_2$ the length BG can be found using a rewritten cosine relation.

$$BG = \sqrt{BD^2 + DG^2 - 2BD \cdot BG \cdot \cos\phi_1} \tag{3.9}$$

When having all length in the triangle BDG together with one angle the remaining two angles can be found using the sine relation.

$$\phi_2 = \sin^{-1}\frac{BD \cdot \sin\phi_1}{BG}, \quad \phi_4 = \arcsin\frac{DG \cdot \sin\phi_1}{BG} \tag{3.10}$$

With the angles defined, the angle ϕ_5 in the triangle BDG can be expressed. The angle ϕ_3 is also obtainable as GCM3 would always be perpendicular to the horizontal axis from B. The angles ϕ_3 and ϕ_5 can be expressed as in Eq. 3.11.

$$\phi_5 = \theta_1 - \phi_4, \quad \phi_3 = 180 - 90 - \phi_5 \tag{3.11}$$

Lastly the angle θ_3 can be described as:

$$\theta_3 = 180 - \phi_2 - \phi_3 \tag{3.12}$$

Which makes it dependant on x_{c1} and x_{c2}. With these trigonometric relations derived the force of the system can be described. The total potential energy of the system is given in

Eq. 3.13.

$$\begin{aligned}\mathcal{P} = g \cdot (m_3(L_{D,G}\sin(\theta_1+\theta_2)) + L_{B,D}\sin(\theta_1) + L_{G,CM3}\sin(\theta_1+\theta_2++\theta_3)) \\ + m_1(L_{B,CM1_y}\cos(\theta_1) + L_{B,CM1_x}\sin(\theta_1)) + m_{cyl2}(L_{D,CMcyl2}\sin(\alpha_8-\alpha_7+\theta_1+\theta_2) \\ + L_{B,D}\sin(\theta_1)) + m_2(L_{D,CM2_y}\cos(\theta_1+\theta_2) + L_{D,CM2_x}\sin(\theta_1+\theta_2) + \\ L_{B,D}\sin(\theta_1)) - L_{B,CMcyl1}m_{cyl1}\sin(\alpha_1+\alpha_3-\theta_1))\end{aligned} \tag{3.13}$$

In order to convert the potential energy to a force the derivative with respect to θ_1 is taken, this will result in the force of the first cylinder [13].

$$F = -\frac{d\mathcal{P}}{d\theta_1} \tag{3.14}$$

With a model constructed it is now possible to find the static force generated by the crane at each piston position. By sweeping every position of the both cylinders with a step of 0.01 m a contour of the force is obtained which can be seen in Figure 3.10.

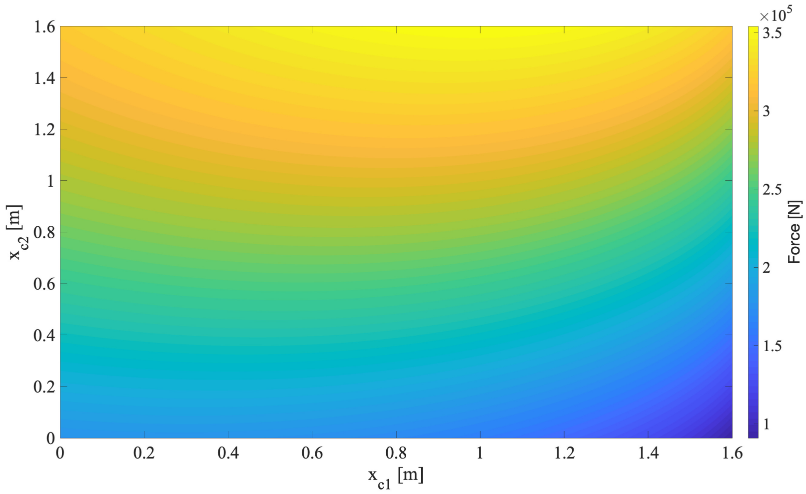

Figure 3.10: Map of static force for all cylinder positions.

It can be seen that the force will never surpass the 380 kN max allowable force. With the system defined in cylinder space a simple trajectory can be set up. As mentioned only one cylinder will be of interest but both cylinders will be moved as the force is depending on the position of both cylinders. The second cylinder will be seen as having perfect tracking. A trajectory could look like as in Figure 3.11.

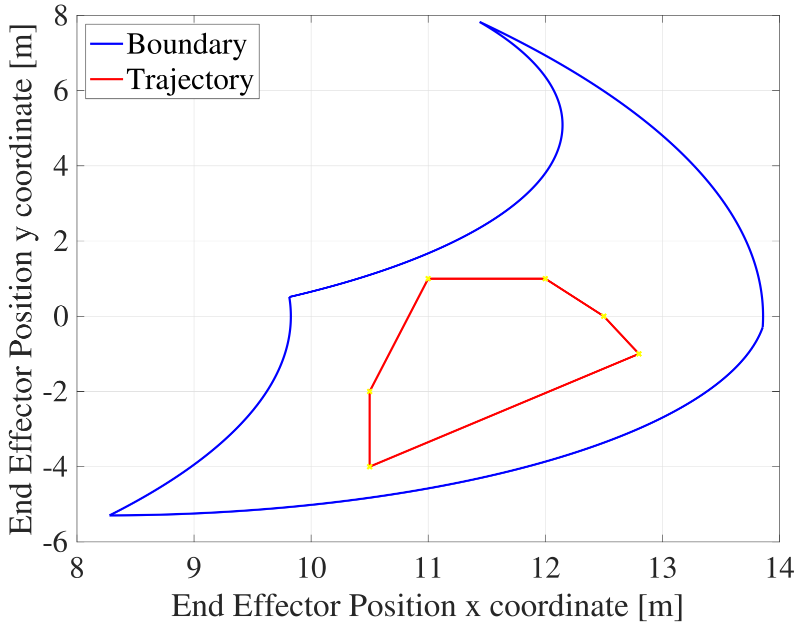

Figure 3.11: Position trajectory of crane end effector with boundary limits.

The path that is followed is the red path while the green line is seen as a initialization only actuated once. If the trajectory is converted into cylinder space the position that the cylinder has to follow can be obtained. This is depicted in Figure 3.12.

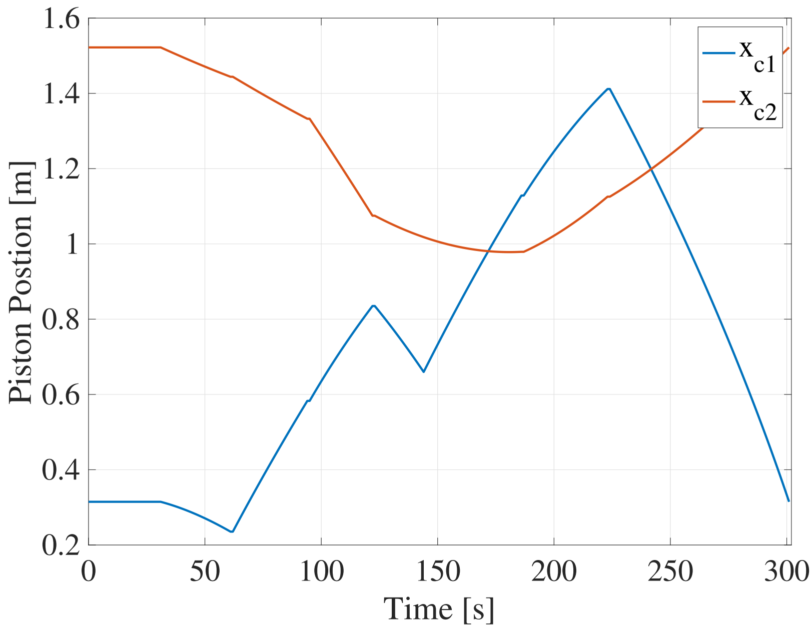

Figure 3.12: Trajectory of crane in cylinder space.

The trajectory that are of focus is the blue line in Figure 3.12. The force profile of the system when following this trajectory can be seen in Figure 3.13.

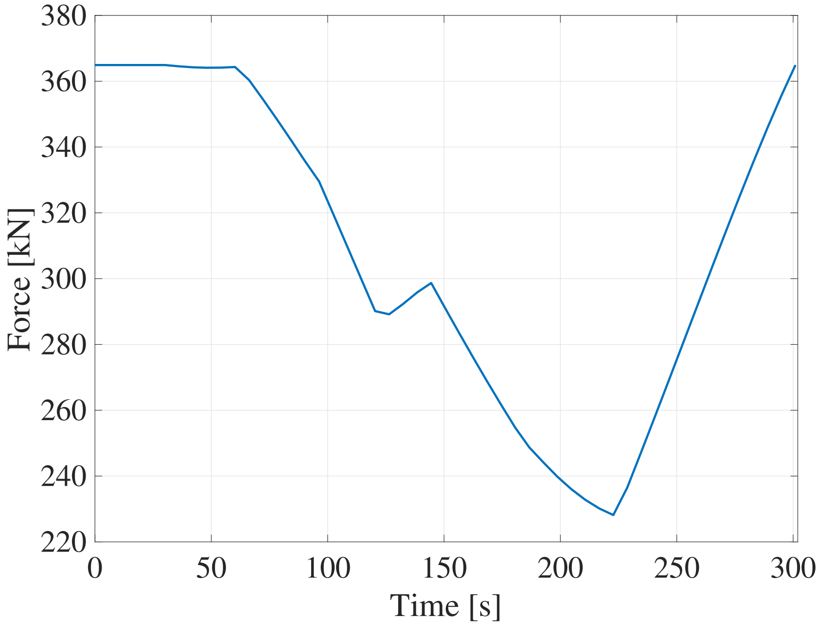

Figure 3.13: Force profile of trajectory reference.

With the desired trajectory and disturbance profile established the model of the system will be elaborated.

4 | Model

In this chapter the model for experiment setup described in Chapter 3 will be derived. The modelling of the system is split up in to four sections, these sections are: Load subsystem, DDC subsystem, Mechanical movement and Energy losses.

In Figure 4.1 a diagram of the overall system can be seen.

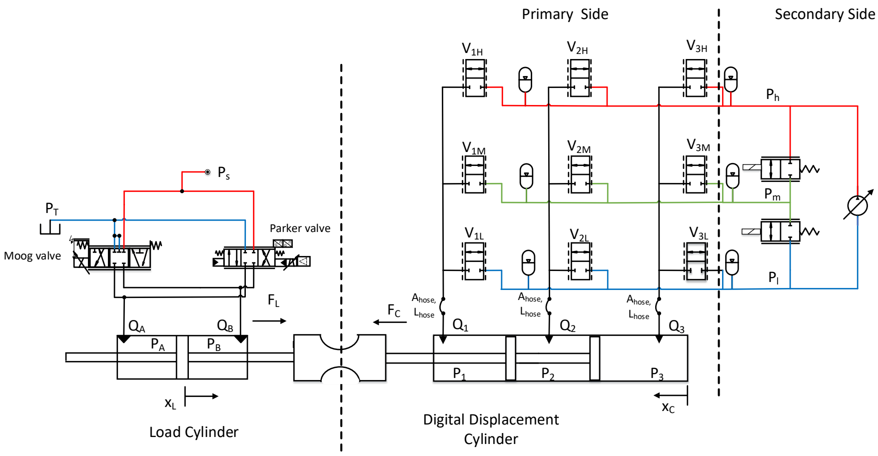

Figure 4.1: Sketch of the experimental setup.

From the figure it is evident that the total system can be categorized into two subsystems. One for each cylinder side, i.e. the DDC subsystem and the Load subsystem. Furthermore the DDC subsystem can be split into two sides, the primary and secondary side. The purpose of the secondary side is, as described in Chapter 3, to maintain a constant pressure in the three pressure lines. As the control of the pressure lines pressure has already been implemented this thesis will not model the secondary side of the DDC subsystem and instead it is assumed that the pressure lines all have a constant supply pressure.

4.1 Digital Displacement cylinder subsystem

In this section the model for the DDC subsystem is derived, this system can be seen in Figure 4.2.

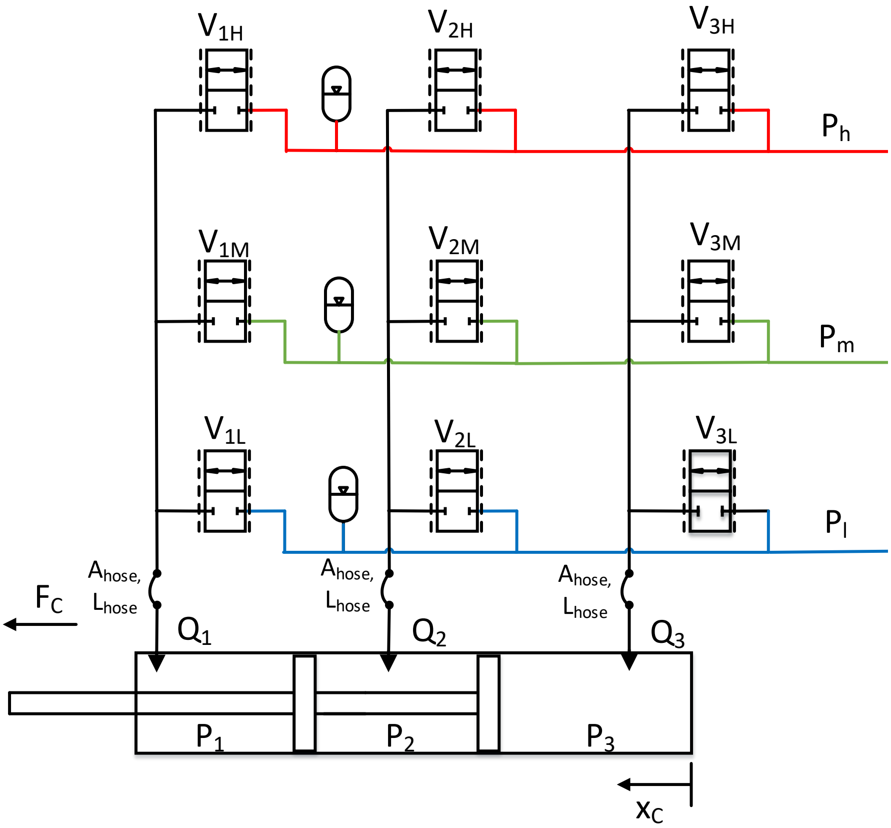

Figure 4.2: Sketch for the primary actuator side.

The DDC system that is to modelled can be seen to consist of nine DFCU's i.e. the manifold, three transmission lines connecting the manifold to the cylinder and the multi-chambered cylinder.

4.1.1 Multi-chamber cylinder

The cylinder is a five chamber cylinder. One of the chambers is vented to air, and two of chambers are connected in parallel effectively making it a three chamber cylinder. The cylinder can be seen in Figure 4.3

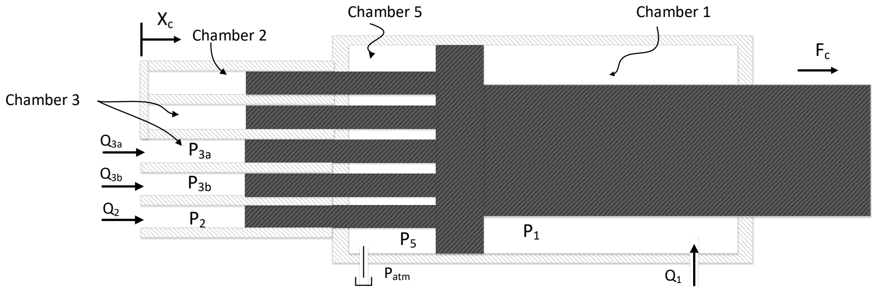

Figure 4.3: Sketch of the multi-chamber cylinder.

Where chamber 3a and 3b are the two chambers in parallel. In [14] it was shown that the pressure build up in the two chambers where approximately equal. They can therefore be modelled as a single chamber, and will from this point on in the thesis only be denoted as a single chamber i.e. chamber 3. Furthermore the starting position of the piston, i.e. $x_c = 0$, is defined at the end stops of the cylinder where the cylinder is fully retracted (see Figure 4.3).

The pressure build up in each chamber is modelled using the continuity equation:

$$\dot{p}_1 = \frac{\beta_{eff}(p_1)}{V_{1.0} - x_c A_1}(Q_1 + \dot{x}_c A_1) \tag{4.1}$$

$$\dot{p}_2 = \frac{\beta_{eff}(p_2)}{V_{2.0} + x_c A_2}(Q_2 - \dot{x}_c A_2) \tag{4.2}$$

$$\dot{p}_3 = \frac{\beta_{eff}(p_3)}{V_{3.0} + x_c A_3}(Q_3 - \dot{x}_c A_3) \tag{4.3}$$

Where:

Q_i	is the flow in/out of each chamber	[m^3/s]
β_{eff}	is the effective bulk modulus of the oil in each chamber	[Pa]
x_c	is the piston position	[m]
$\dot{x}_c$	is the piston velocity	[m/s]
$V_{i.0}$	is the dead volume in each chamber when $x_c = 0$	[m^3]
A_i	is the cross-sectional area of each chamber	[m^2]
$\dot{p}_i$	is the pressure gradient in each chamber	[Pa/s]
p_i	is the pressure in each chamber	[Pa]

Where i denotes the cylinder chamber i.e. $i = \{1, 2, 3\}$.

The effective bulk modulus is affected by the amount of entrapped air in the oil and is modelled by the following equation:

$$\beta_{eff}(p) = \frac{1}{\dfrac{1}{\beta_f} + \dfrac{\epsilon_a(p)}{\beta_a}} \tag{4.4}$$

Where:

β_f	is the bulk modulus of the pure oil	[Pa]
β_a	is the air stiffness	[Pa]
ϵ_a	is the volumetric ratio of entrapped air in the oil	[-]

The stiffness and volumetric ratio of the air in the oil are modelled using:

$$\beta_a = \kappa\, p \tag{4.5}$$

$$\epsilon_a(p) = \left(\frac{P_0\ \epsilon_{a.0}}{p}\right)^{\frac{1}{\kappa}} \tag{4.6}$$

Where:

κ	is the adiabatic constant set to 1.4	[-]
P_0	is the atmospheric pressure	[Pa]
$\epsilon_{\mathrm{a},0}$	is the volumetric ratio of air at atmospheric pressure	[-]

As a rule of thumb the bulk modulus in a moving cylinder is upper limited to 10000 bar [15] and $\epsilon_{a,0}$ is used as a soft parameter to fit the model during the validation of the model.

4.1.2 Manifold

The manifold consist of a total of nine DFCU's which controls the flow to the cylinder chambers.

The flow through a single DFCU can be modelled using the orifice equation:

$$Q_{i,j} = n_i\ k_{v,c}\ x_{v,c}\sqrt{|P_j - p_i|}\ \mathrm{sign}(P_j - p_i) \tag{4.7}$$

Where the subscript j denotes the pressure line, i still denotes the cylinder chamber and:

P_j	is the pressure in the pressure line	[Pa]
$\mathrm{x}_{v,c}$	is the state of valve. 1 = open, 0 = closed	[-]
$\mathrm{k}_{v,c}$	is the valve gain	$[\mathrm{m}^3/s/\mathrm{Pa}^{0.5}]$
n_i	is the number of valves in the DFCU	[-]

As each chamber is connected to three DFCU's the total flow to a chamber is the sum through each of the three DFCU's:

$$Q_i = \sum_{j=1}^{3} Q_{i,j} \tag{4.8}$$

The valve gain for each of the on/off valves used in the DFCU is estimated from the ΔP-Q characteristics of the valve.

Valve dynamics

The valve dynamic for the valves in the DFCU is modelled using a second order transfer function and a opening and closing delay:

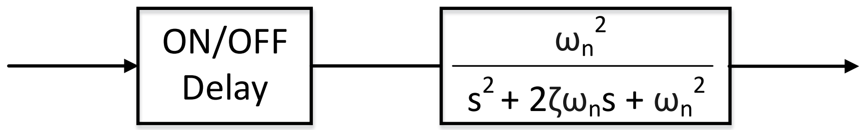

Figure 4.4: Block diagram of the valve dynamics for DFCU valves.

Both the closing/opening delay and the second order dynamics was found from experimental measurements provided by Bucher Hydraulics. The opening and closing delay is found to be 9ms. The damping is found to be 0.95 and the natural frequency is 630 rad/s.

4.1.3 Transmission line

As mentioned in Chapter 3 the manifold is placed on the outside of the experiment setup, and 2-4 meter long transmission lines are used to connect the manifold to the cylinder chambers. Due to the fast on/off nature of the valves used in the manifold, pressure oscillations are expected, and transmission line models are included to capture these dynamics. The transmission line model used in this thesis is a lumped parameter model. In the lumped parameter model used, each transmission line is split up into a fixed amount of lumps and the pressure and flow is calculated for each lump. A figure representing the principle behind the lumped parameter model can be seen in Figure 4.5.

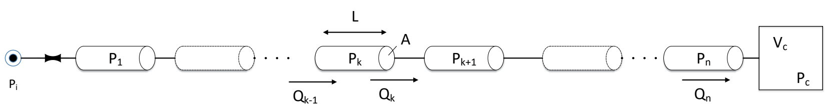

Figure 4.5: Lumped parameter model.

From the figure it is noted the Q_k is the flow from the k'th lump to the k+1 lump. Q_0 is the flow entering the transmission line from the manifold, and Q_n is the flow entering the chamber, where n is the total number of lumps in the model. Likewise p_k is the pressure of the k'th lump and p_{n+1} is the pressure of the cylinder chamber.

The acceleration of the flow is calculated using Newtons second law, where it is exploited that the mass can be written as the density multiplied with the volume. The volume is equal to the cross sectional area of the transmission line multiplied with the length. Finally the cross sectional area multiplied with the acceleration gives the flow acceleration. To calculate the pressure change the continuity equation is used.

For the k'th lump the equations are expressed as:

$$\dot{Q}_k = \frac{A(p_k - p_{k+1} - \Delta p_{fric,k})}{L\rho} \tag{4.9}$$

$$\dot{p}_k = \frac{\beta_{eff}(p_k)}{A\ L}(Q_{k-1} - Q_k) \tag{4.10}$$

Where:

A	is the cross sectional area of the transmission line lump	[m^2]
L	is the length of the transmission line lump	[m]
ρ	is the density of the oil	[kg/m^3]
Δp_{fric}	is the pressure loss due to friction	[Pa]

The effective bulk modulus is calculated using Eq. 4.4. The transmission lines are consisting of hoses and pipes, and the maximum bulk modulus is set to 7000 bar for the hoses and 15000 bar for the pipes. This is done to include the stiffness of the hoses and pipes into the model. [16]

The pressure loss due to friction, i.e. Δp_{fric} is a combination of the pressure loss due to the flow in each lump, and the pressure loss in the fittings of the transmission lines. The pressure loss due to the flow can be calculated using Darcy's equation which for laminar and turbulent flow respectively can be expressed as:

$$\Delta p_{Laminar} = \frac{128\mu L}{\pi d^4} Q_k \tag{4.11}$$

$$\Delta p_{Turbulent} = 0.242 \frac{\mu^{0.25}\rho^{0.75} L}{d^{4.75}} Q_k^{1.75} \tag{4.12}$$

Where:

μ	is the dynamic viscosity of the oil	[Pa s]
d	is the diameter transmission line lump	[m]

The flow is defined as a laminar flow if the Reynolds number is below 2000 and turbulent flow if Reynolds number is above 2400 [15]. Where Reynolds number is calculated as:

$$Re = \frac{4\rho}{d\pi\mu} Q_k \tag{4.13}$$

To account for the transition area between the laminar and turbulent flow a hyperbolic tangent function is used:

$$\Delta p_{p\_loss} = \Delta p_{Laminar} \frac{1 - \tanh\left(\frac{Re - 2200}{50}\right)}{2} + \Delta p_{Turbulent} \frac{\tanh\left(\frac{Re - 2200}{50}\right) + 1}{2} \tag{4.14}$$

In this function 2200 is used, as it is the middle point between the laminar and turbulent state of the fluid. and its divided by 50, as the function will give ≈ -1 if Re $=$ 2000 and ≈ 1 if Re $=$ 2400. [12]

The pressure loss due to the fittings are calculated as:

$$\Delta p_{fitting,k} = \frac{\xi \rho}{2} \left(\frac{Q_k}{\frac{1}{4} d^2 \pi} \right)^2 \tag{4.15}$$

Where:

ξ is the loss coefficient for the fitting [Pa s]

The total friction loss in the k'th lump can then be calculated as:

$$\Delta p_{fric,k} = \Delta p_{p\_loss,k} + \Delta p_{fitting\_1,k} + \Delta p_{fitting\_2,k} + ... + \Delta p_{fitting\_m,k} \tag{4.16}$$

Where m is the total number of fittings for the lump in question.

4.2 Load subsystem

The load subsystem consist of a symmetric cylinder and two proportional valves controlling the flow supplied to the cylinder chambers. The Load subsystem can be seen in the following figure:

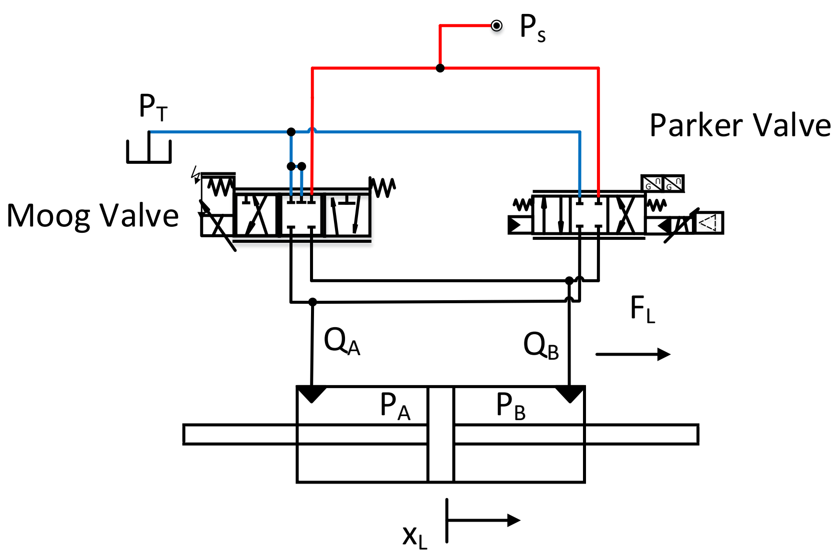

Figure 4.6: Sketch of the Load subsystem to be modelled.

The pressure in each chamber is calculated using the continuity equation:

$$\dot{p}_a = \frac{\beta_{eff}(p_a)}{V_{a.0} + x_L A_L} (Q_a - \dot{x}_L A_L) \tag{4.17}$$

$$\dot{p}_b = \frac{\beta_{eff}(p_b)}{V_{b.0} - x_L A_L}(\dot{x}_L A_L - Q_b) \tag{4.18}$$

Where:

x_L	is the piston position	[m]
$\dot{x}_L$	is the piston velocity	[m/s]
$V_{i.0}$	is the dead volume in each chamber when $x_L = 0$	[m^3]
A_L	is the cross-sectional area of each chamber	[m^2]

The β_{eff} is again calculated using Eq. 4.4. The zero position of the load cylinder is defined as the middle position of the load cylinder, but as the load cylinder and actuator cylinder are connected using a sleigh, their position is also related to each other. This relation is given as:

$$x_L = \frac{x_{c,max}}{2} - x_c \tag{4.19}$$

Where:

$x_{c,max}$	is the maximum stroke length of the actuator cylinder	[m]

The two proportional valves controlling the flow to the cylinder chambers are a Parker D111FP valve and a Moog D634 valve. As mentioned in Chapter 3 the Parker valve has an overlap of 10% around its neutral position, and the Moog valve is connected in parallel in order to compensate for this. The flow through both valves are calculated using the orifice equation:

For the Moog valve the flow is calculated as:

$$Q_{a,M} = \begin{cases} -k_{v,M} x_{v,M} \sqrt{|P_s - p_a|}\,\mathrm{sign}(P_s - p_a) & , \quad x_{v,M} \geq 0 \\ -k_{v,M} x_{v,M} \sqrt{|p_a - P_t|}\,\mathrm{sign}(p_a - P_t) & , \quad x_{v,M} < 0 \end{cases} \tag{4.20}$$

$$Q_{b,M} = \begin{cases} -k_{v,M} x_{v,M} \sqrt{|p_b - P_t|}\,\mathrm{sign}(p_b - P_t) & , \quad x_{v,M} \geq 0 \\ -k_{v,M} x_{v,M} \sqrt{|P_s - p_b|}\,\mathrm{sign}(P_s - p_b) & , \quad x_{v,M} < 0 \end{cases} \tag{4.21}$$

Where:

$k_{v,M}$	is the valve gain for the Moog valve	[$m^3/s/Pa^{0.5}$]
P_s	is the supply pressure	[m/Pa]
P_t	is the tank pressure	[Pa]
$x_{v,M}$	is the normalized position of the Moog valve	[-]

And for the Parker valve:

$$Q_{a,P} = \begin{cases} k_{v,P}(x_{v,P}) \sqrt{|P_s - p_a|}\,\mathrm{sign}(P_s - p_a) & , \quad x_{v,P} \geq 0 \\ -k_{v,P}(x_{v,P}) \sqrt{|p_a - P_t|}\,\mathrm{sign}(p_a - P_t) & , \quad x_{v,P} < 0 \end{cases} \tag{4.22}$$

$$Q_{b,P} = \begin{cases} k_{v,P}(x_{v,P}) \sqrt{|p_b - P_t|}\,\mathrm{sign}(p_b - P_t) & , \quad x_{v,P} \geq 0 \\ -k_{v,P}(x_{v,P}) \sqrt{|P_s - p_b|}\,\mathrm{sign}(P_s - p_b) & , \quad x_{v,P} < 0 \end{cases} \tag{4.23}$$

Where:

$k_{v,P}(x_{v,P})$	is the valve gain as a function of spool position	$[m^3/s/Pa^{0.5}]$
$x_{v,P}$	is the normalized position of the Parker valve	[-]

To make sure that the cylinder chambers get the right flow, a flow sharing algorithm is used. This flow sharing algorithm has been developed and implemented in an earlier project [12] and it will therefore not be derived in this project. The valve splitting algorithm used is explained in Appendix C.

Valve dynamics

The dynamics of both the Parker and the Moog valve has been modelled using a second order transfer function:

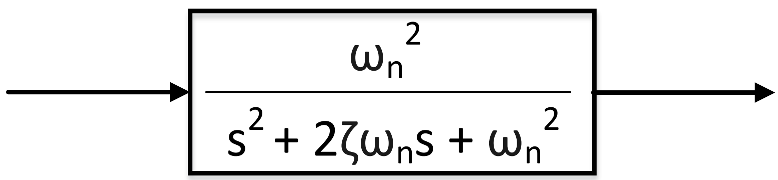

Figure 4.7: Block diagram of the valve dynamics for both the Parker and Moog valve.

Both the damping and the natural frequency of the valves are found from the data sheets where frequency response for the valve is given for different strokes. These frequency responses can be seen in the following figures:

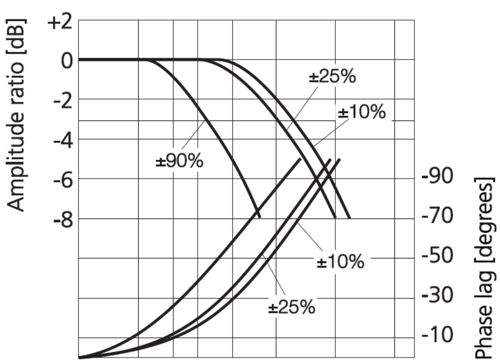

Figure 4.8: Frequency response for the Moog valve [2].

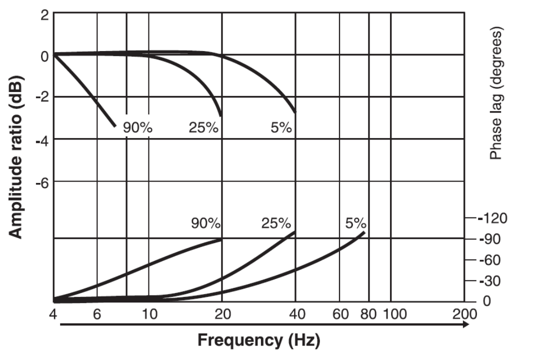

Figure 4.9: Frequency response for the Parker valve [3].

For the Moog valve a stroke length of 25% is used, with a damping of 0.8 and a natural frequency of 310 rad/s. For the Parker valve a stroke length of 5% is used, with a damping of 0.8 and a natural frequency of 250 rad/s. The reason for choosing an amplitude of 5% for the Parker valve is because lager amplitudes are not expected. For the Moog valve however is expected to be used with larger amplitude and an amplitude of 25% is therefore used here.

4.3 Mechanical movement

The mechanical system consist of the pistons of both the load cylinder and the DDC cylinder and the sleigh connecting them both. This can be seen in Figure 4.10.

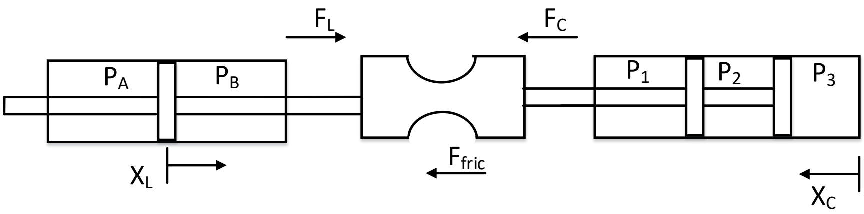

Figure 4.10: Sketch of mechanical system with forces.

The force equilibrium for the system can be set up using Newtons second law:

$$m_{tot}\ddot{x}_c = F_c - F_L - F_{fric} \tag{4.24}$$

Where:

m_{tot}	is the total mass of the mechanical system	[kg]
F_c	is the force created by the actuator cylinder	[N]
F_L	is the force created by the load cylinder	[N]
F_{fric}	is the friction force due to the movement	[N]
$\ddot{x}_c$	is the acceleration of the actuator cylinder	[m/s]

Where the forces from the two cylinders can be expressed as:

$$F_c = p_2A_2 + p_3A_3 + P_{atm}A_{idle} - p_1A_1 \tag{4.25}$$

$$F_L = A_p(p_a - p_b) \tag{4.26}$$

Lastly the friction force, is calculated as a combination of both a vicious friction and the Coulomb friction:

$$F_{fric} = B_c\dot{x}_c + F_{Coulomb}\tanh\left(\frac{\dot{x}_c}{\gamma_{fric}}\right) \tag{4.27}$$

The friction coefficients B_c, $F_{Coulomb}$, and γ_{fric}, are used as fitting parameters during the validation of the model.

4.4 Energy losses

In this section the system energy losses present in the system are investigated. In the hydraulic test setup there are two main losses that will be of focus. These losses are associated with the valve-manifold in form of compressibility losses, that occurs every time there is a shift between pressure levels, and the losses due to throttling of the valves. Other losses could be leakage losses but as it is assumed no leakage occur over the DDC system this is neglected.

4.4.1 Compressibility losses for fixed chamber volume

When a volume at a given pressure is connected to a pressure line with a different pressure a power loss is created. This power loss is defined as the difference between energy supplied by the fixed pressure line, E_s and the potential pressure energy saved in the volume, E_p. This compressibility loss can be described as in Eq. 4.28 assuming the bulk modulus to be constant [11].

$$E_{sw} = E_s - E_p = \frac{1}{2}\Delta p^2 \frac{V}{\beta} \tag{4.28}$$

β	is the effective bulk modulus of oil in the chamber	[Pa]
V	is the volume of the chamber	[m^3]
Δp	is the pressure change between the old and new pressure in the control chamber [m^2]	[Pa]

The total switching loss of the DDC is then the sum of the losses in each cylinder chamber.

$$E_{sw} = \sum_{i=1}^{3} \frac{1}{2}\Delta p^2 \frac{V_i(x_c)}{\beta} \tag{4.29}$$

It can be noted form Eq. 4.29 that the energy loss is dependent on the cylinder position and the pressure difference. In Figure 4.11 the loss from switching between each pressure state can be seen at a piston position of 1 m.

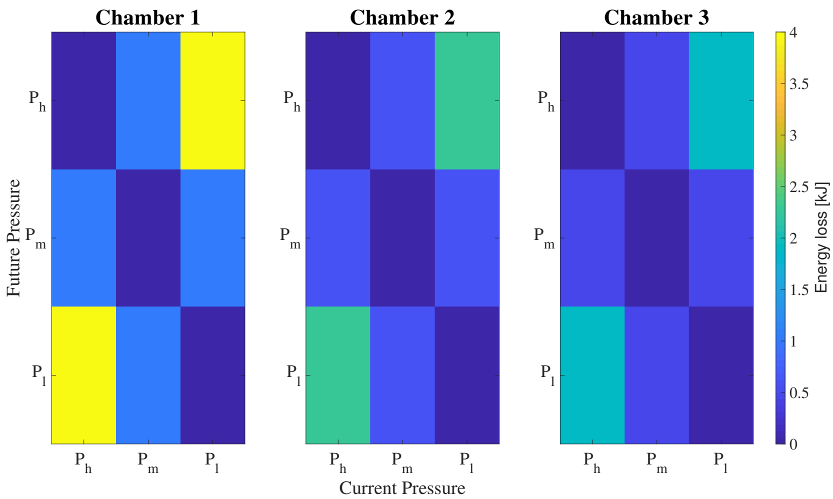

Figure 4.11: Switching loss between different pressure states when $x_c = 1$ m, $P_l = 20$ bar, $P_m = 100$ bar and $P_h = 180$ bar .

From the figure it can be seen that the switching loss is highest when switching from the LP to HP or vice versa. An interesting observation is that changing from LP to HP has less loss if the medium pressure, (MP), level is used as an intermediate step. An example of this can be seen from chamber 1, where switching from P_h to P_l have a energy loss of ≈ 4 kJ. Subsequently switching from P_h to P_m and then from P_m to P_l would result in an energy loss of $\approx 1{+}1 = 2$ kJ. This can also be proven mathematically which can be seen in the Equations in 4.30.

$$\begin{aligned}
&\frac{1}{2}(P_h - P_l)^2\frac{V}{\beta} > \left(\frac{1}{2}(P_h - P_m)^2\frac{V}{\beta} + \frac{1}{2}(P_m - P_l)^2\frac{V}{\beta}\right) \\
&\Rightarrow (P_h - P_l)^2 > \left((P_h - P_m)^2 + (P_m - P_l)^2\right) \\
&\Rightarrow P_h^2 + P_l^2 - 2P_hP_l > P_m^2 + P_l^2 - 2P_mP_l + P_h^2 + P_m^2 - 2P_hP_m \\
&\Rightarrow -P_hP_l > P_m^2 - P_mP_l - P_hP_m \\
&\Rightarrow 0 > P_l(P_h - P_m) + P_m(P_m - P_h) \\
&\Rightarrow 0 > P_l(P_h - P_m) - P_m(P_h - P_m)
\end{aligned} \tag{4.30}$$

Since $P_h > P_m$ it must be that $(P_h - P_m) > 0$ and since $P_m > P_l$ the inequality is true.

As the energy loss is also position dependent the energy loss as a function of cylinder position is investigated for a constant pressure switch from P_l to P_m with a pressure difference of 80 bar. The result can be seen in Figure 4.12.

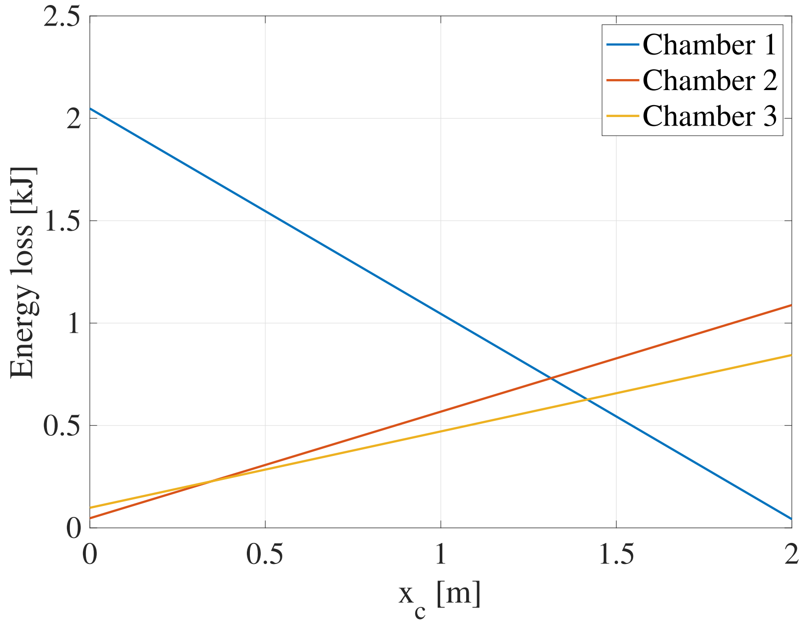

Figure 4.12: Switching loss as a function of x_c when switching between $P_l = 20$ bar and $P_m = 100$ bar.

The tendency would be the same if other pressure values were used. It can be seen that chamber 1 has the biggest energy loss due to the bigger volume.

4.4.2 Compressibility losses for changing chamber volume

When a chamber volume is changing during a pressure shift the pressure profile in the chamber becomes relevant to the energy loss across the valve. This is due to the throttling loss associated with the volume expansion.

The energy loss for a changing volume is given in Eq. 4.31.

$$E_{sw} = \frac{1}{2}\Delta P^2 \frac{V}{\beta} + \frac{1}{2}\Delta P^2 \dot{V} T_p + \frac{13}{70}\Delta P^2 \frac{\dot{V}}{\beta} T_p \tag{4.31}$$

The proof of the equation can be found in [17]. It can seen that the first term of the equation is the energy loss from the fixed volume chamber. The second term is seen dependent on the pressure change, volume gradient and the time duration of the pressure shift, T_p. The last term is dependent on the volume gradient, bulk modulus, T_p and the square of the pressure change with a proportionality constant. In figure 4.13 the energy loss has been calculated for different positions and velocities.

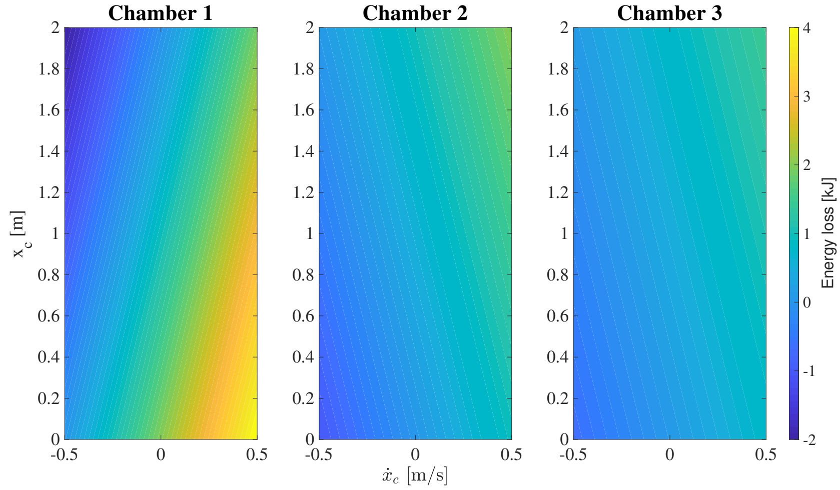

Figure 4.13: Switching loss for each chamber for different positions and velocities when switching from 180 to 100 bar with $T_p = 40$ ms.

It can be seen how the energy loss is varying when changing both the position and the velocity and thus influencing the loss associated with a pressure change.

4.4.3 Throttling losses

The other loss evaluated is the throttling losses. Each chamber is always connected to one pressure line through the valve-manifold, and a throttling loss will therefore always be present if the cylinder is moving. The throttling loss is associated with the loss through each of these valves. It can be described as the total flow and pressure drop across each DFCU.

$$E_{th} = \sum_{i=1}^{3} Q_i \Delta p = \sum_{i=1}^{3} \frac{|A_i v_c|^3}{(n_i k_v)^2} \tag{4.32}$$

A_i	Ai is the piston area of the i'th chamber	[m^2]
n_i	is the number of valves in the DFCU connecting the i'th chamber	$[-]$
k_v	is the valve gain for the valves used in the DFCUs	[m$^3/s/$Pa$^{0.5}$]

It can be noted that the throttling loss is dependent on the piston velocity cubed, and independent of the chamber pressures. The throttling losses from the resulting flow for each chamber and the total loss as function of the sleigh velocity are shown in the Figure 4.14.

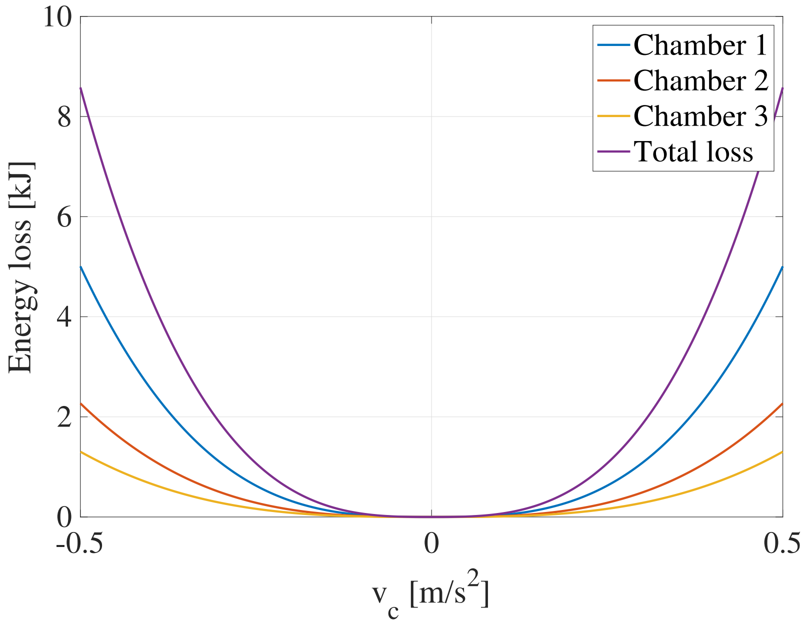

Figure 4.14: Throttle loss as a function of sleigh velocity.

It can be seen that the throttling loss is low for piston velocities under $\pm$ 0.2 m/s.

5 | Validation of Model

In this Chapter the non linear model of the system is validated. In order to validate the model three different experiments were performed and the experimental results are compared to the simulations.

The three experiments performed were:

- Moog valve - In this experiment only the Moog valve on the load side was actuated. On the DDC side the low pressure line was connected to all the chambers.
- Parker valve - Same as for the Moog valve, but this time only the Parker valve was actuated.
- DDC side - In this experiment both the Parker and Moog valve was kept closed while different force step were given to the DDC side.

In order to fit the model to the experimental results the following three unknown soft parameters were varied until an satisfactory fit was found:

- Air in the oil: $\epsilon_{air,0}$
- Coulomb friction: $F_{Coulomb}$
- Viscous friction: B_c

All the parameters used for the model together with the final value of the soft parameters can be found in Appendix B.

5.1 Load side validation

In this section the results from the Parker experiment and Moog experiment will be presented. The main goal of both experiments is to validate the valve gains, the position of the cylinder, together with the pressure dynamics for both of the load side chambers.

At first the valve gains from the data sheets were used however it was found that the gains were not accurate when compared to the experiments. This can be seen in Figure 5.1 and 5.2.

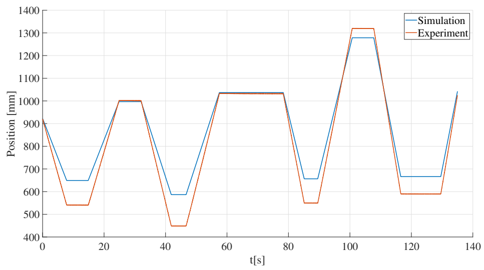

Figure 5.1: Cylinder position for Moog valve using the valve gain from the data sheet.

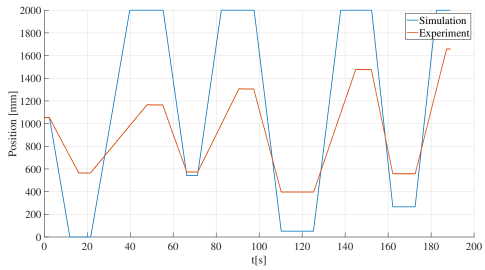

Figure 5.2: Cylinder position for Parker valve using the valve gain from the data sheet.

To correct this, two experiments were performed, one for each of the two valves, in order to experimentally determine the correct valve gains. These experiments are described in Appendix A and resulted in two look-up tables for the valve gains. The two look-up tables can be seen in the two following figures.

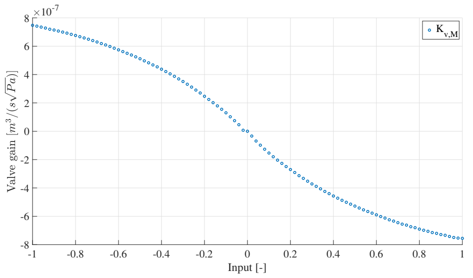

Figure 5.3: Valve gains for the Moog valve used in the look-up table.

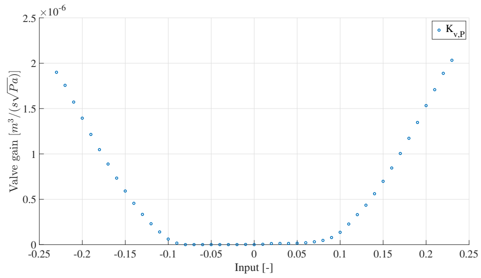

Figure 5.4: Valve gains for the Parker valve used in the look-up table.

The valve gains for inputs not covered in the experiment is found using linear interpolation. Furthermore it can be seen that for the Parker valve only experimental values up to 2.3 volt is found, as it was not possible to find a steady state velocity for higher inputs. This however should not be a problem as higher inputs for the Parker valve is not expected.

The position for both valves when the look-up tables are implemented can be seen in Figure 5.5 and 5.6.

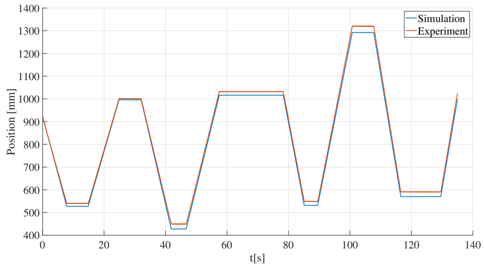

Figure 5.5: Cylinder position for Moog valve with new look-up table.

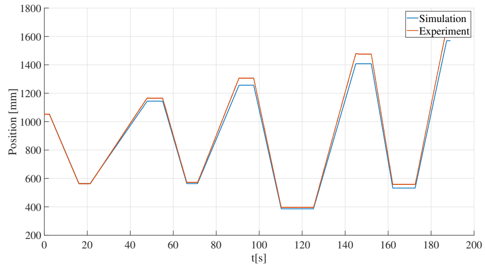

Figure 5.6: Cylinder position for Parker valve with new look-up table.

As it can be seen from the figures the drift has disappeared and there is only a small stationary error of 20mm for the Moog valve and 70mm for the Parker valve.

After confirming that the new look-up tables for the valve gains are accurate the velocity and pressure dynamics for both valve experiments are validated. In Figure 5.7 and 5.8 the velocity dynamics can be seen.

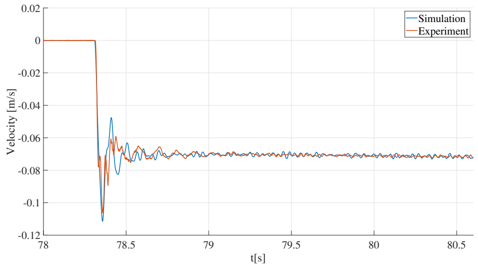

Figure 5.7: Cylinder velocity for Moog valve at a step of 4 volt.

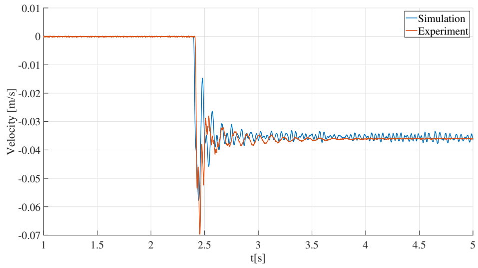

Figure 5.8: Cylinder velocity for Parker valve at a step of 1.1 volt.

From the velocity it can be seen that the model is not a perfect fit. Even though the model is not a perfect fit, the frequency of the oscillations from the model match the experiment

In Figure 5.9 and 5.10 the pressure dynamics for the load pressure can be seen i.e. the pressure difference between chamber A and B.

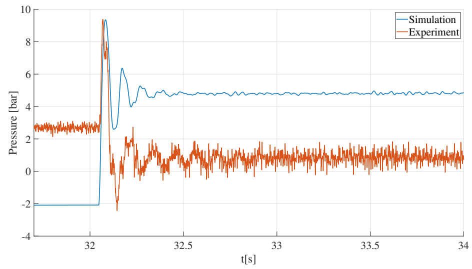

Figure 5.9: Load pressure for Moog valve at a step of 3 volt.

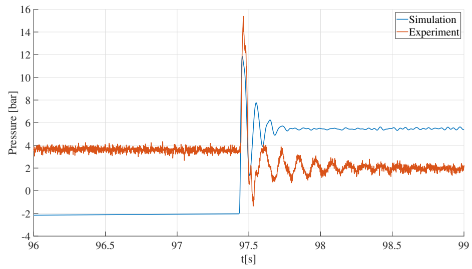

Figure 5.10: Load pressure for Parker valve at a step of 1.3 volt.

As with the velocity the model is not a perfect fit for the load side pressure. The static pressure does not match between the model and experiment, but again the oscillations frequency match with the model being a little more damped than the experiment.

One thing that was found when validating the pressure dynamics for both experiments was that several pressure rises were present in the experimental data. These pressure rises can clearly be seen in Figure 5.11 where the pressure for chamber A can be seen together with the given input and the simulation result, e.g from 55 to 80 seconds.

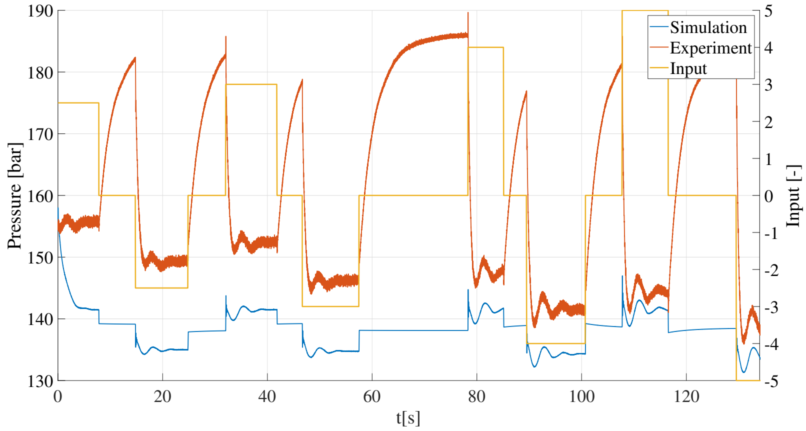

Figure 5.11: Experimental and simulated pressure for Chamber A together with the given input.

These pressure rises can be seen to happen every time that no input is given to the valve. Similar results are happening for chamber B and for the Parker valve experiment. These pressure spikes indicates that some leakage over the two load valves are present that is not accounted for in the model. To rectify this an more elaborate valve model for both valves will have to be developed, but due to time limitations this will not be done in this thesis.

Even though the leakage and therefore the pressure for the two chambers of the load cylinder is not modelled correctly when the two valves are closed, the developed model is still accepted as a valid model. The reason for this is twofold, firstly the position and the dynamics for both the pressure and velocity are similar to the experimental results. Secondly the purpose of the load side model is to help create a controller that will control the disturbance force on the DDC cylinder, and a difference between the modeled force and the actual force, can be seen as yet another form of disturbance.

5.2 DDC side validation

In this section the DDC side of the model will be validated. The main goal of this experiment is to validate the pressure dynamics in the three cylinder chambers, and to furthermore validate the transmission-line model. To do this different force steps were given. The result for the pressure dynamics in each chamber can be seen in the following figures at different force steps.

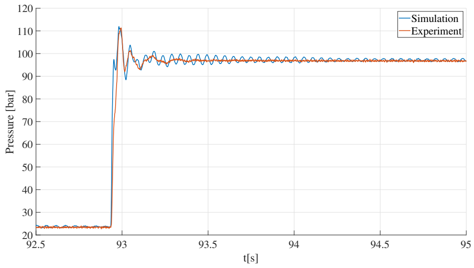

Figure 5.12: Chamber 1 pressure at a step from 20 bar to 100 bar.

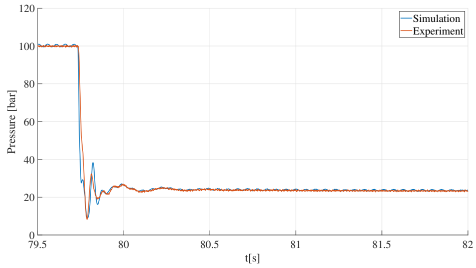

Figure 5.13: Chamber 1 pressure at a step from 100 bar to 20 bar.

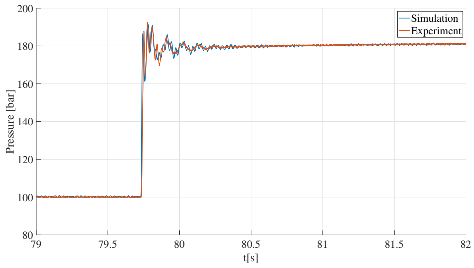

Figure 5.14: Chamber 2 pressure at a step from 100 bar to 180 bar.

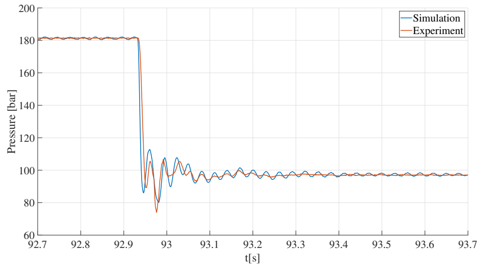

Figure 5.15: Chamber 2 pressure at a step from 180 bar to 100 bar

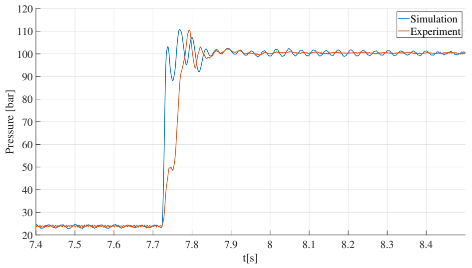

Figure 5.16: Chamber 3 pressure at a step from 20 bar to 100 bar.

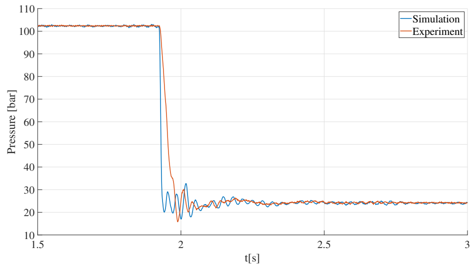

Figure 5.17: Chamber 3 pressure at a step from 100 bar to 20 bar.

When looking at the pressure dynamics for all three chambers, both when the pressure is increased and decreased, it can be seen that the model fits the experiment with the model being slightly lesser damped when compared to the experiment.

To validate the transmission line model, and to see the effects of the transmission line the measured pressure just after the manifold is compared to the pressure before the transmission line in the model. These results can be seen in the following figures.

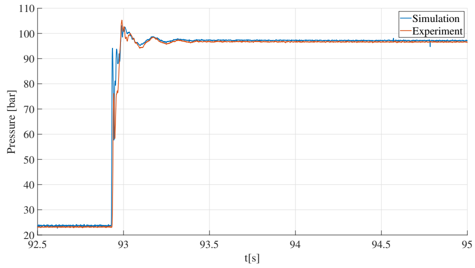

Figure 5.18: Chamber 1 pressure right after the manifold.

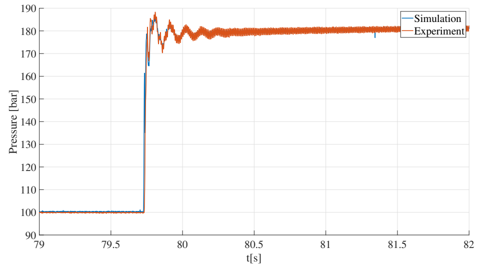

Figure 5.19: Chamber 2 pressure right after the manifold.

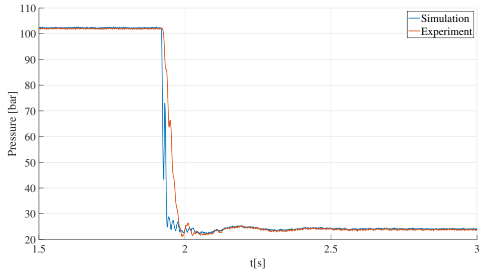

Figure 5.20: Chamber 3 pressure right after the manifold.

From Figure 5.18, 5.19 and 5.20 it can be seen that the model also fits the experiment before the transmission line indicating that the model for the transmission line is also correct.

Lastly the leakage mentioned for the Load side validation over the two load valves also affected the position of this experiment. This can be seen in figure 5.21.

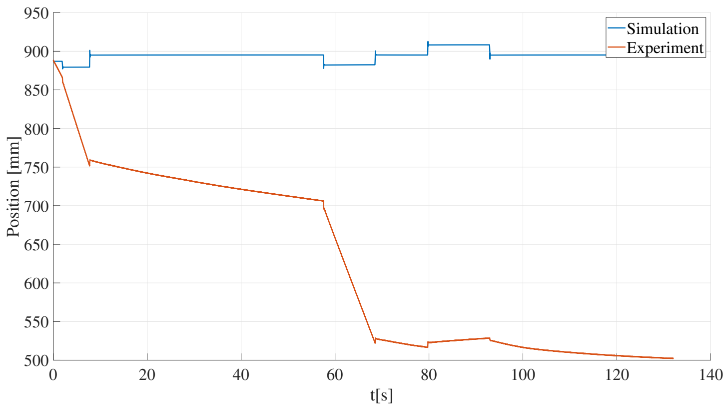

Figure 5.21: Position of the cylinder during the DDC experiment.

This effect is ignored though, as the load valves are firstly not expected to be closed during the control, and secondly the position controller designed should cancel this movement.

Over all the nonlinear model for the DDC side is concluded to be accurate enough, that it can be used to design position control.

6 Load side controller

In this chapter the force controller used to produce the load force is designed. The purpose of this force is to function as a disturbance on the position control for the DDC. Before the controller can be designed, first the load side model is changed into a reduced order model an hereafter it is linearized.

6.1 Reduced order model

Before a reduced order model can be developed the model for the two load-side valves are simplified into a single valve model:

$$Q_a = \begin{cases} -k_v(x_{eq})\sqrt{|P_s - p_a|}\,\mathrm{sign}(P_s - p_a) & , \quad x_{eq} \geq 0 \\ -k_v(x_{eq})\sqrt{|p_a - P_t|}\,\mathrm{sign}(p_a - P_t) & , \quad x_{eq} < 0 \end{cases} \tag{6.1}$$

$$Q_b = \begin{cases} -k_v(x_{eq})\sqrt{|p_b - P_t|}\,\mathrm{sign}(p_b - P_t) & , \quad x_{eq} \geq 0 \\ -k_v(x_{eq})\sqrt{|P_s - p_b|}\,\mathrm{sign}(P_s - p_b) & , \quad x_{eq} < 0 \end{cases} \tag{6.2}$$

Where:

$k_v(x_{eq})$	is the equivalent valve gain	$[\mathrm{m}^3/s/\mathrm{Pa}^{0.5}]$
x_{eq}	is the equivalent valve input	[-]

How the equivalent valve gain and valve input are calculated can be seen in Appendix C.

After simplifying the orifice equation the load pressure and load flow is defined:

$$P_L = P_a - P_b \tag{6.3}$$

$$Q_L = \frac{Q_a + Q_b}{2} \tag{6.4}$$

Assuming steady state conditions the load flow can be defined using the load pressure:

$$Q_L = \begin{cases} -k_v(x_{eq})\sqrt{\left|\frac{1}{2}(P_s - P_L - P_t)\right|}\,\mathrm{sign}(P_s - P_L - P_t) & , \quad x_{eq} \geq 0 \\ -k_v(x_{eq})\sqrt{\left|\frac{1}{2}(P_s + P_L - P_t)\right|}\,\mathrm{sign}(P_s + P_L - P_t) & , \quad x_{eq} < 0 \end{cases} \tag{6.5}$$

As it can be seen the only difference between the equation for a positive and negative metering edge is the sign of the load pressure. These two equations can therefore be combined into single equation:

$$Q_L = -k_v(x_{eq})\sqrt{\left|\frac{1}{2}(P_s - \frac{x_{eq}}{|x_{eq}|}P_L - P_t)\right|} \cdot sign(P_s - \frac{x_{eq}}{|x_{eq}|}P_L - P_t) \tag{6.6}$$

A continuity equation expressed using the load pressure can hereafter also be defined. This is done by inserting both of the chamber continuity equations into Eq. 6.4:

$$Q_L = \frac{1}{2}\left(\frac{V_{a,0} + x_L A_L}{\beta(P_a)}\dot{p}_a + 2\dot{x}_L A_L - \frac{V_{b,0} + x_L A_L}{\beta(P_b)}\dot{p}_b\right) \tag{6.7}$$

If it is then assumed that the the oil stiffness for the two chambers are equal, and that the cylinder is at center position, ($\beta(p_a) = \beta(p_b) = \beta$, $V_{a,0} = V_{b,0} = \frac{V_t}{2}$). The equation can be reduced to:

$$Q_L = \dot{x}_L A_L + \frac{V_t}{4\beta}\dot{P}_L \tag{6.8}$$

The final reduced order model for the load side is therefore given by the following three equations:

$$Q_L = -k_v(x_{eq})\sqrt{\left|\frac{1}{2}(P_s - \frac{x_{eq}}{|x_{eq}|}P_L - P_t)\right|} \cdot sign(P_s - \frac{x_{eq}}{|x_{eq}|}P_L - P_t) \tag{6.9}$$

$$\dot{P}_L = (Q_L - \dot{x}_L A_L)\frac{4\beta}{V_t} \tag{6.10}$$

$$\ddot{x}_L = \frac{1}{m_{tot}}\left(A_L P_L - B_c \dot{x}_L - F_{Coulumb} \cdot tanh\left(\frac{\dot{x}_L}{\gamma_{fric}}\right)\right) \tag{6.11}$$

In order to validate the reduced order model it has been compared to to developed nonlinear model. The comparison between the load pressure and velocity can be seen in Figure 6.1 and 6.2.

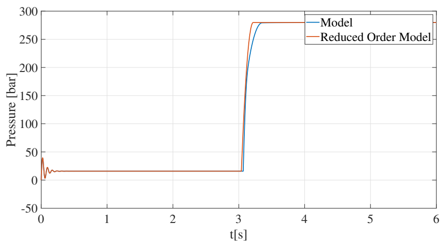

Figure 6.1: Load pressure comparison between reduced order model and nonlinear model.

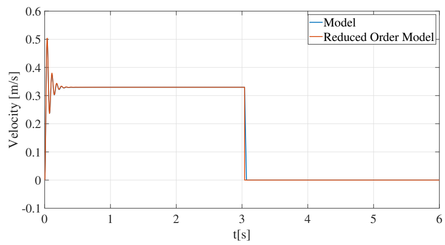

Figure 6.2: Velocity comparison between reduced order model and nonlinear model.

As it can be seen both the velocity and pressure is very similar between the two models, with only slight differences. These differences are believed to be due to the simplification done to the continuity equation. In spite of these small differences the model is accepted as valid.

6.2 Linear Load model

In order for a controller to be designed for the reduced order model, the model firstly needs to be linearized. The main part of the system equations that adds non-linearity is the orifice equation.

The orifice equation is linearized using a first order Taylor approximation:

$$Q_L = K_{qp}P_L + K_{qx}x_{eq} \tag{6.12}$$

Where the linearization constants are given as:

$$K_{qp} = \left.\frac{\partial Q_L}{\partial P_L}\right|_{x_{eq,0},P_{L,0}} = \frac{sign(x_{eq,0})k_v(x_{eq,0})}{4\sqrt{\left|\frac{1}{2}(P_s - sign(x_{eq,0})P_{L,0} - P_t)\right|}} \cdot sign(P_s - sign(x_{eq,0})P_{L,0} - P_t) \tag{6.13}$$

$$K_{qx} = \left.\frac{\partial Q_L}{\partial x_{eq}}\right|_{x_{eq,0},P_{L,0}} = -k_v(x_{eq,0})\sqrt{\left|\frac{1}{2}(P_s - sign(x_{eq,0})P_{L,0} - P_t)\right|} \cdot sign(P_s - sign(x_{eq,0})P_{L,0} - P_t) \tag{6.14}$$

Lastly the equation describing the movement of the cylinder is linearized by simply ignoring the Coulomb friction and the disturbance, i.e. the force from the DDC side.

$$\ddot{x}_L = \frac{1}{m_{tot}}(A_L P_L - B_c\dot{x}) \tag{6.15}$$

Using these linearized equations, two equations for the linear system can are set up:

$$\ddot{x}_L = \frac{1}{m_{tot}}(A_L P_L - B_c\dot{x}) \tag{6.16}$$

$$\dot{P}_L = (Q_L - \dot{x}_L A_L)\frac{4\beta}{V_t} \tag{6.17}$$

Inserting Eq. 6.12 into Eq. 6.17 yields:

$$\dot{P}_L = (K_{qp}P_L + K_{qx}x_{eq} - \dot{x}_L A_L)\frac{4\beta}{V_t} \tag{6.18}$$

6.2.1 Validation of the linear model

To validate the derived linear model, the position and velocity output for both the linear and non-linear model will be compared. In the comparison the linearization values for both the load pressure and the equivalent valve input were chosen to be $x_{eq,0} = 0.1$ and $P_{L,0} = 50$ bar. To test the model a similar input as the linearization point is used and the results can be seen in Figure 6.3 and 6.4. The input used for the equivalent valve input is a step of 0.104.

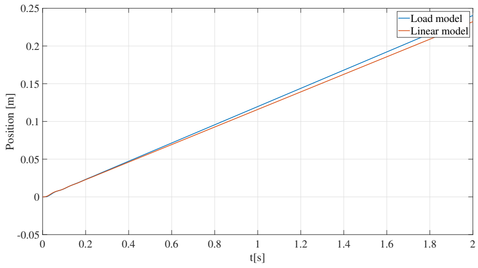

Figure 6.3: Position comparison between linear and non-linear model, with an input of 0.104.

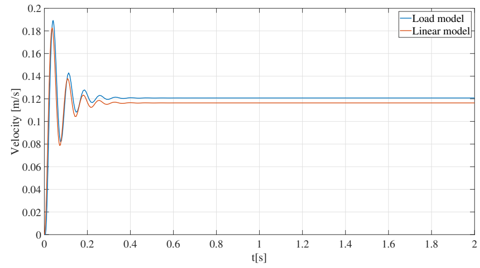

Figure 6.4: Velocity comparison between linear and non-linear model, with an input of 0.104.

As it can be seen both the steady state value and the frequency for the velocity are comparable, and the linear model can therefore be concluded to be valid if similar input as the linearization points is used.

Due to the high non-linearity of the orifice equation, a slightly bigger difference between the input signal and the linearization point will no longer give comparable results. This can be seen in the following figures were an input of 0.11 is used instead.

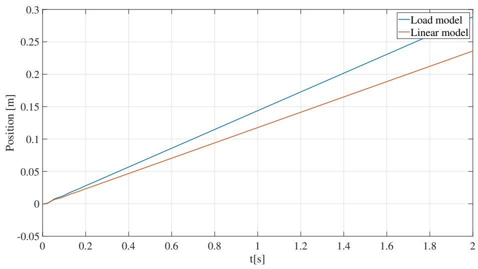

Figure 6.5: Position comparison between linear and non-linear model, with an input of 0.11.

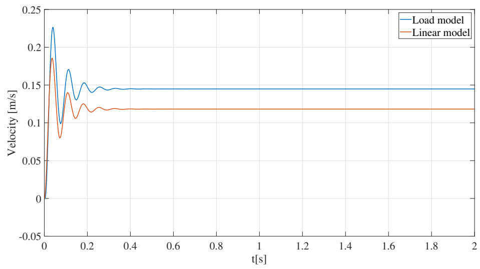

Figure 6.6: Velocity comparison between linear and non-linear model, with an input of 0.11.

In Figure 6.5 and 6.6 it can be seen that the frequency of the signal remains the same, but the steady state value is no longer the same.

6.3 Controller design

In this section the controller used to produce the load force used as a disturbance for the DDC control is going to be designed. As the purpose of the load force is to act as a disturbance, a perfect tracking is not needed. Hence all extra deviations will just be seen as extra disturbance, that the DDC controller will have to compensate for.

A valve flow compensator is introduced to minimize the influence of the linearization points for the linearized orifice equation. This valve flow compensator is done by introducing a virtual input $\tilde{u}$ proportional to the steady state velocity:

$$\tilde{u} = \frac{Q_L}{A_p} \tag{6.19}$$

This virtual input is then used in the orifice equation to determine a valve gain for a wanted input.

$$k_v(x_{eq}) = \frac{\tilde{u}A_p}{\sqrt{\frac{1}{2}|P_s - sign(x_{eq})P_L - P_t|}} \tag{6.20}$$

From this valve gain and using the valve splitting algorithm a look-up table can be set up to determine the equivalent valve input for all possible valve gains that can be obtained for the load side.

The block diagram for the load side control system, using this virtual input can be seen in the following figure:

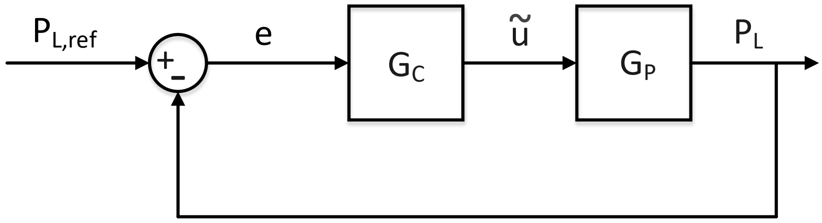

Figure 6.7: Block diagram for the load side control system.

In Figure 6.7, the signal e is the error between the load pressure reference and the load pressure of the system. This load pressure reference is determined from the force reference. $G_c(s)$ is the transfer function for the controller which determines the virtual input to the system. $G_p(s)$ is the transfer function for the plant i.e the load side. This transfer function $G_p(s)$ is determined by Laplace transforming the linear equations from Eq. 6.16 and 6.17:

$$X_c(s) = \frac{1}{m_{tot}s^2 + B_c s} A_p P_L(s) \tag{6.21}$$

$$P_L(s) = \frac{K}{s}(Q_L - A_p X_c(s)s) \tag{6.22}$$

where:

$$K = \frac{4\beta}{V_t} \tag{6.23}$$

Eq. 6.21 is inserted into Eq. 6.22 and the following transfer function is found:

$$G_p(s) = \frac{P_L(s)}{Q_L(s)} = \frac{Ks + K\dfrac{B_c}{m_{tot}}}{s^2 + \dfrac{B_c}{m_{tot}}s + K\dfrac{A_p^2}{m_{tot}}} \tag{6.24}$$

By then using Eq. 6.19 and inserting it instead of $Q_L(s)$ the final transfer function, $G_p(s)$ of the system is obtained.

$$G_p(s) = \frac{P_L(s)}{\tilde{U}(s)} = \frac{A_pKs + A_pK\dfrac{B_c}{m_{tot}}}{s^2 + \dfrac{B_c}{m_{tot}}s + K\dfrac{A_p^2}{m_{tot}}} \tag{6.25}$$

The frequency response for this transfer function can be seen in the following bode diagram;

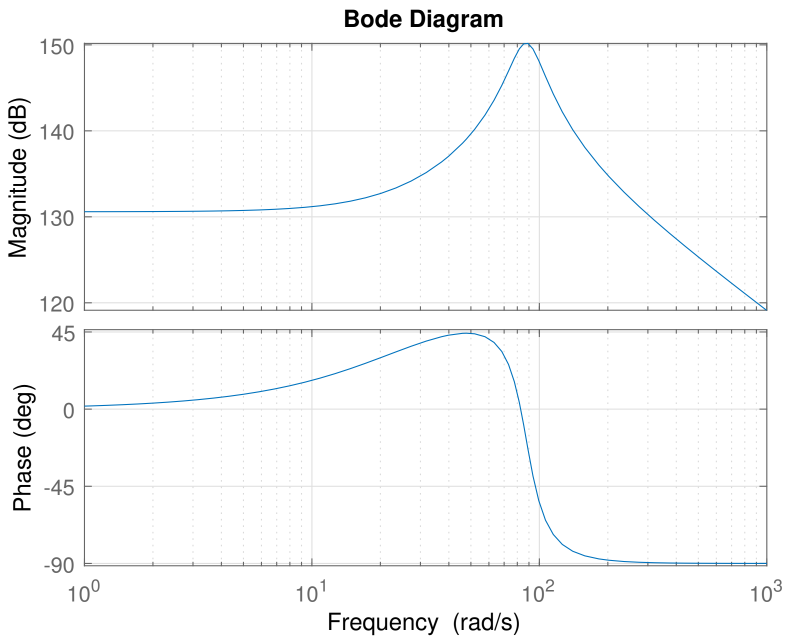

Figure 6.8: Open loop bode diagram for the uncompensated system.

From the bode diagram is can be seen that the system has a gain margin of infinity and a phase margin of 90 degrees indicating that the closed loop system is staple. The closed loop response with a controller gain of one for the system can be seen in Figure 6.9

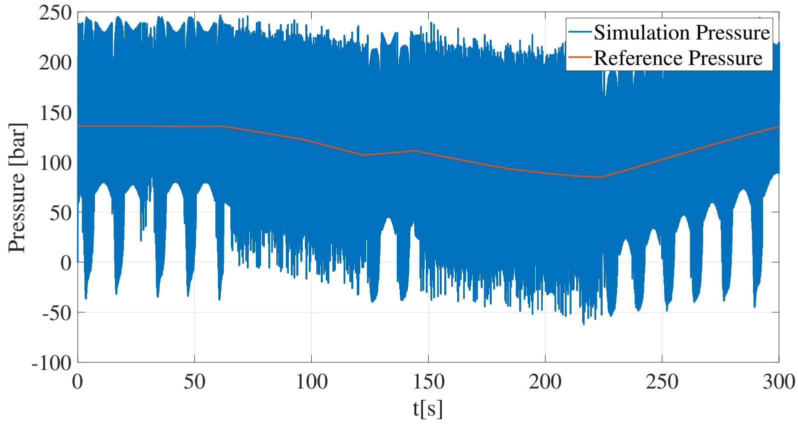

Figure 6.9: Reference tracking of the closed loop system with a controller gain of one.

As it can be seen in the figure the actual load pressure from the simulation oscillate with big spikes around the reference. To minimize these oscillations a proportional controller is designed. The reason for using a proportional controller is because a steady state error is allowed, and it simplifies the the design process of the controller. By using simple trial and error a controller with the gain of: $K_p = 6 \cdot 10^{-8}$ is designed and implemented using:

$$\tilde{u} = K_p \cdot e \tag{6.26}$$

The load pressure reference tracking for the system using this controller can be seen in the following figure:

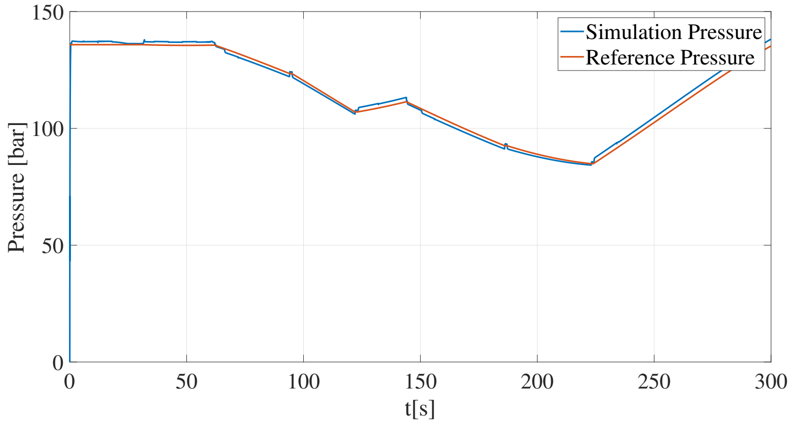

Figure 6.10: Reference load pressure and actual load pressure of the system using the designed controller.

As it can be seen from the figure using the designed controller results in the system being able to track the desired output. This controller will therefore be used to control the disturbance force used in the position control of the DDC cylinder.

7 Control Considerations

In this chapter the considerations for choosing a control structure are presented. These considerations take into account both the system that is actuated and the controller requirements that needs to be achieved.

The overall goal of the controller problem as described in Chapter 2 is to minimize the position tracking error of the trajectory for a Knuckle Boom crane. The trajectory to be followed is designed in Chapter 3 and the trajectory is shown again i Figure 7.1.

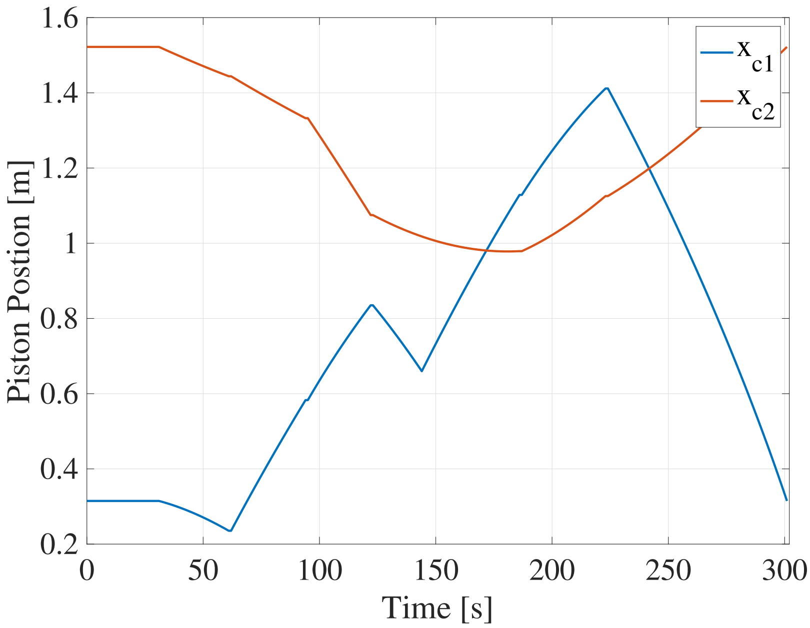

Figure 7.1: Trajectory of crane in cylinder space.

Another goal in this thesis is however also to reduce the energy cost during the position tracking. Theoretically reducing the energy cost of the system will lead to an increase of the tracking error as less energy is available. Therefore the control output will have to be a compromise between position tracking accuracy and the energy cost of the system.

To help determining if a designed controller still has an acceptable tracking error, even if the energy cost is reduced, a maximum allowable Root Mean Squared (RMS) tracking error is introduced. The RMS is taken from a Götting crane [18]. For this crane a maximum RMS error of 3 cm is allowable when looking at the position of the end effector. This error then has to be converted to an allowable error for the cylinder, this is done using inverse kinematics using the dimensions of the crane used in this thesis. Doing this the maximum allowable RMS error for the cylinder is found to be 2 cm.

As this thesis aims to minimize the energy losses it should be specified which system losses that should be taken into account. It is assumed that the two major sources of energy loss comes from the switching losses every time a pressure switch occurs, and from the throttling losses in the DFCU valves. Therefore the goal will be to minimize these. Losses occurring at the Load side cylinder, losses associated with keeping the pressure lines at a constant pressure and the electrical losses occurring every time a valve in the DFCU is turned on are neglected.

7.1 System Considerations

The system used for the position control is the DDC side of the experiment setup described in Chapter 3. In this chapter it was described how the DDC is not able to produce a continuous output force, instead it is able to produce 27 different discrete force outputs. In order for DDC to approach a continuous output switching between the available force levels is necessary. This switching is achieved by controlling the 9 DFCU's. As each DFCU consist of several valves all able to be controlled individually this complicates the control problem as the system is a effectively a multiple input single output (MISO) system. One thing that can be noted is that from Figure 4.2 in Chapter 4 is that each chamber in the DDC is connected to three DFCU's. Each of these DFCU's are connected to a different pressure line each with a different pressure level. If more than one DFCU for a single chamber are turned on it will create short circuit phenomenon for the flow. Looking at it from a energy saving perspective this short circuit phenomenon should result in huge loss. As the one goal is energy minimization the system will be limited to only having one operating DFCU for each chamber. By implementing this constraint on the system a delay will be introduced. This delay is due to the opening and closing of the DFCU valves. Each valve has a opening and closing time of 0.02 s thus when switching from one DFCU to another 0.04 s will pass before the desired output will be reached.

7.2 Control Strategy

As the test setup is not a novel constellation some different control strategies has already been examined. One control scheme that has shown great promise when considering both tracking and energy efficiency is the Model Predictve Control (MPC). When using MPC the basic idea is to use a system model to predict the future output inside a predetermined time horizon. The controller predicts the output based on the current measured state and future inputs that are then optimized with respect to a chosen criteria. The criteria could be e.g energy losses or tracking performance. The calculated output for the controller is then held until new information is available where the new optimal outputs are calculated again. An advantage of MPC is the possibility to control non-linear systems without having to make a linear approximations. The disadvantage is that it requires heavy computational power to recalculate the optimal solution in real time depending on how big a horizon that is desired. Most investigation has therefore been theoretical and not tested on a physical setup. In [11] it is concluded that based on simulations MPC could be a good control option. However due to the difficulties of implementation and the disadvantage of high computational power use, this thesis will focus on looking into other control options.

One other control option that could be considered to be a viable control strategy is the optimal controllers such as Linear Quadratic Controllers (LQC). This control type could be a possible solution as they are capable of handling MISO systems. One challenge with this controller is however that the energy cost needs to be converted to a system state in order for the controller to minimize it. If the energy can be transformed into a state the LQC can penalize high energy cost.

As LQC is normally used on continuous system a quick test is done to se if this type of controller is applicable on the considered discrete system. This simple test involved designing a LQC for position tracking without considering the energy cost or discretizing the output force. The design process of the LQC can be found in Appendix D. The result of the LQC position tracking and corresponding control inputs can be seen in Figure 7.2 and 7.3.

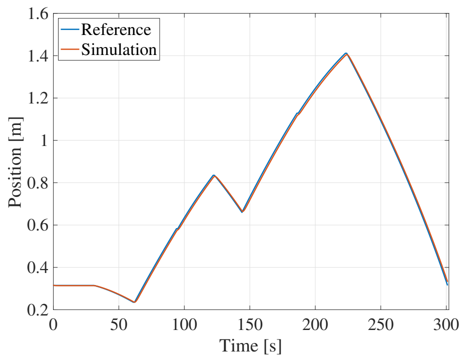

Figure 7.2: LQC tracking result.

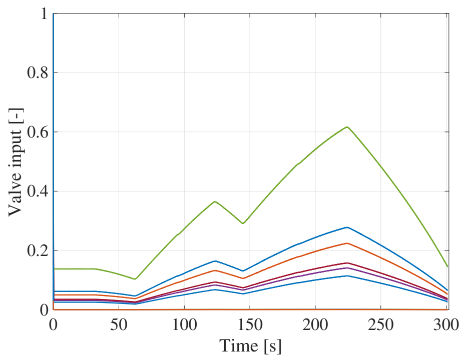

Figure 7.3: LQC controller inputs.

It is possible to develop a continuous LQC that can track the position reference, however the constraint of only opening a single DFCU for one chamber is clearly violated. As it can be seen in order to be able to track the controller opens more than one DFCU which was unwanted. A solution to this problem could not be found hence the LQC method was disregarded and a different control structure has to be chosen.

A well known control scheme is the linear PID controller. Using this control type on system can be a challenge as this type of controller is used for single input single output (SISO) systems. Therefore if using this control type some simplification of the system is needed to be done. Furthermore the energy cost is also needed to be Incorporated somehow. A control strategy using this PID controller will be examined in the following chapter.

8 Force controller

In this chapter the new control structure for the position controller will be developed. It was chosen to design a controller with force as an output and a position error as an input. This transforms the control problem from a MISO to a SISO control problem, thereby avoiding the problem of opening of multiple DFCU's for each chamber. As the controller output is continuous, the force output will also be a continuous signal. This can not be achieved with the DDC and thus the output force of the controller has to be converted to one of the 27 achievable forces of the DDC. This transformation from a continuous force to a discrete force output will be achieved by a switching algorithm. By then knowing the output force of the DDC, the input for the DFCU's are also known. Thus the problem of opening more than a single DFCU for each chamber at a time is avoided. The idea is sketched in the block diagram in Figure 8.1.

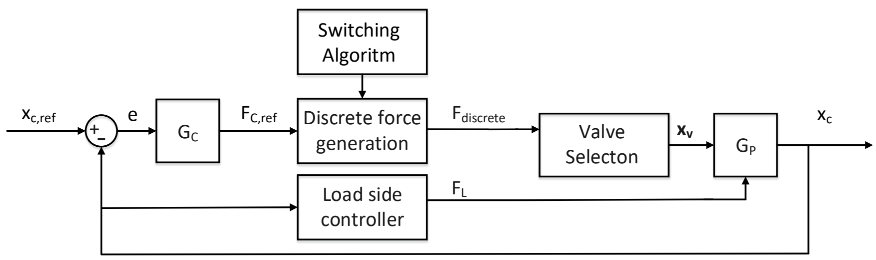

Figure 8.1: Block diagram of force control concept.

8.1 Design of the controller

In order to design the force controller a transfer function for the system has to be derived. This is done by linearizing the system equations. As the force is now an output the pressure dynamics are neglected and the overall system equation is thus only the equation of movement of the cylinder.

$$\ddot{x}_c = \frac{1}{m_{tot}}(F_C - B_c\dot{x}) \tag{8.1}$$

Hereafter Eq. 8.1 is Laplace transformed.

$$\frac{X(s)}{F(s)} = \frac{\frac{1}{M_{tot}}}{s^2 - \frac{B_c}{M_{tot}}s} \tag{8.2}$$

Furthermore as a delay of 0.04 s is needed in order to achieve a force switch due to the opening and closing times of the DFCU valves. This is added by modeling a delay in the Laplace domain. The transfer function of the system is given as in Eq. 8.3.

$$\frac{X(s)}{F(s)} = \frac{\frac{1}{M_{tot}}}{s^2 - \frac{B_c}{M_{tot}}s} \cdot e^{-t_d s} \tag{8.3}$$

The bode diagram of the system with and without delay can be seen in Figure 8.2.

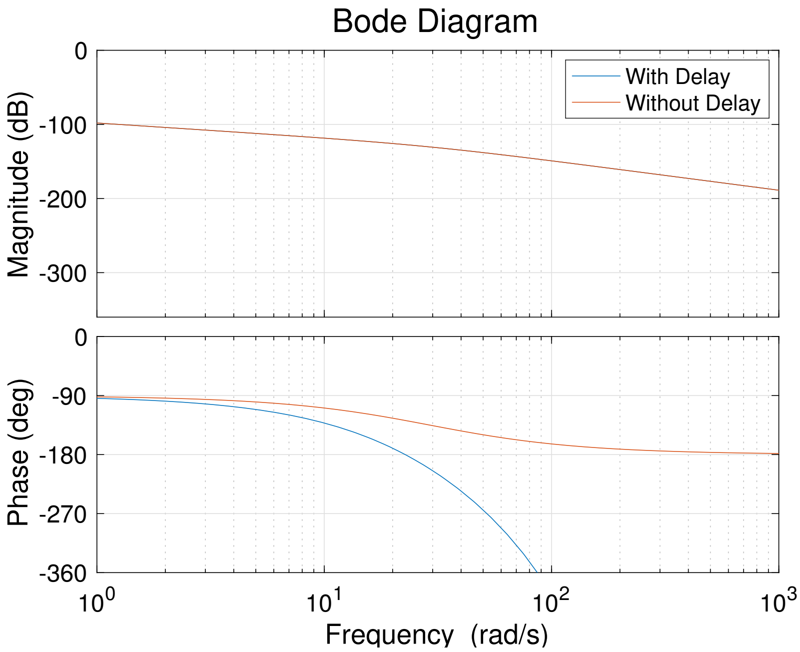

Figure 8.2: Bode diagram of the uncompensated system.

From the bode diagram the effects of the delay can clearly be seen on the phase which decreases rapidly compared to the transfer function without delay. Furthermore it can be noted that the gain margin is no longer infinite as there is a phase crossing of -180 deg for the system with delay.

Two different controllers are designed and tested using simulations, namely a P controller and a PI controller to find the one with the best performance in regards to reducing the steady state error of the position tracking.

Both controllers are designed using the bode plot shown above for the system with delay. The design requirements for the controllers are to achieve a phase margin around 45 deg and a gain margin of ≥ 6 dB [19]. The compensated bode blots together with the uncompensated bode plot can be seen in Figures 8.3 and 8.4.

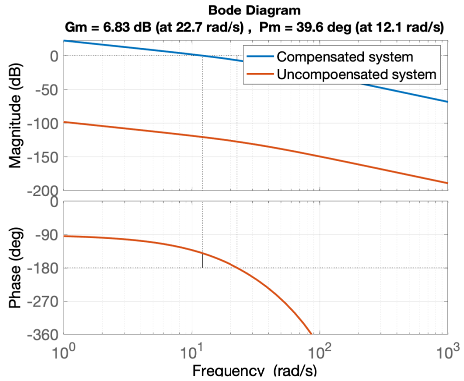

Figure 8.3: Bode diagram of system with P compensator.

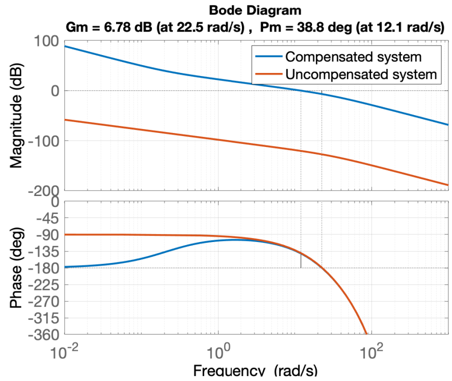

Figure 8.4: Bode diagram of system with PI compensator.

For both controllers the gain and phase margin lies in the desired region. The K values of the controllers are given in the table below.

	K_P	K_I
P	$10.49 \cdot 10^5$	NAN
PI	2.224e5	10.45e5

Table 8.1: Control parameters.

As a switching algorithm for converting the continuous controller output to a discrete force, the closet discrete force is chosen every time the controller samples. An illustration of this switching can be seen in Figure 8.5.

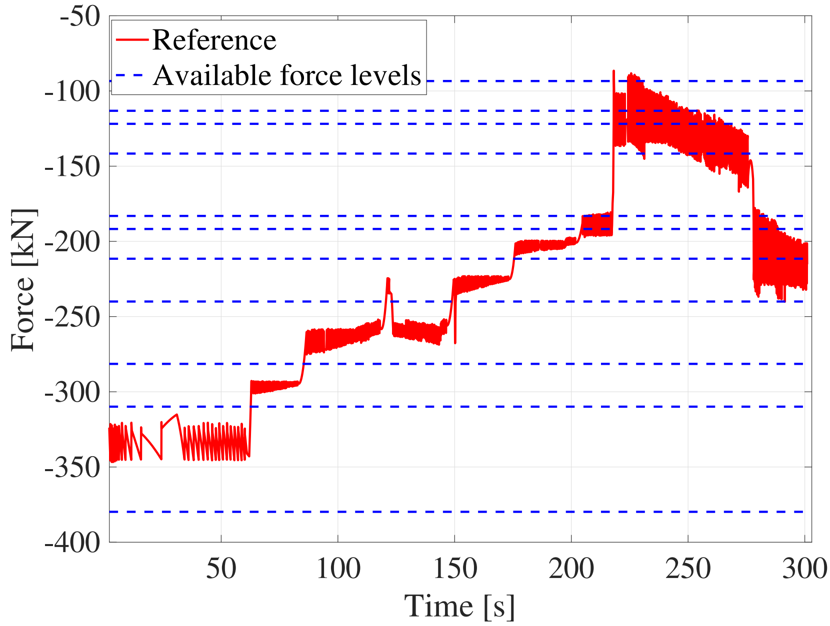

Figure 8.5: Continuous force reference with available discrete forces.

For this figure this will mean that the output force will always be chosen as the closet blue line to the red reference.

The system has then been tested with these controllers using simulations, the result can be seen in Figures 8.6 and 8.7.

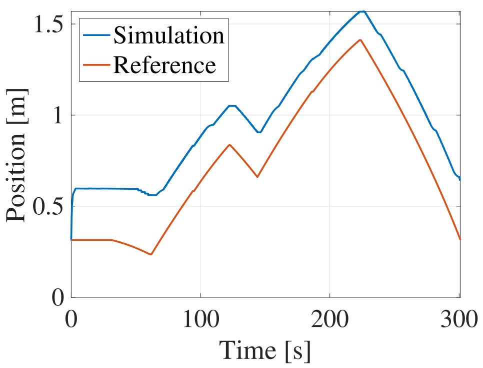

Figure 8.6: Tracking result for P controller, e_{RMS} = 0.236 m.

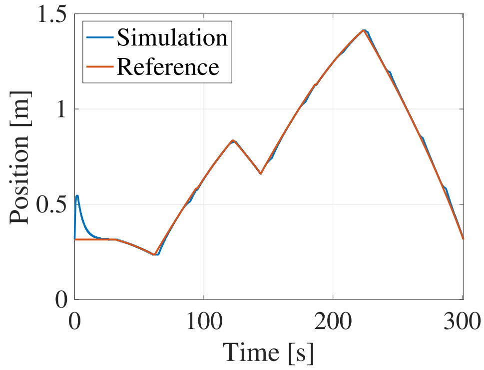

Figure 8.7: Tracking result for PI controller, e_{RMS} = 0.028 m.

As it can be seen in both cases the tracking is not as good as expected, as both controllers result in an bigger error than allowed, where the RMS error is 0.236m and 0.028m for the P and PI controller respectively. Some reasons for this can be due to the disturbance from the load side which have not been modeled with the linear system or the offset in the beginning. The offset in the beginning is believed to be due to the initial condition of the simulation not being at steady state values. However the PI controller is close to the allowable error of 0.02 m. Therefore the controller is manually tuned more aggressive to improve tracking and settling time of the controller. The new controller gains are tuned to be $K_P = 6.3 \cdot 10^6$ and $K_I = 1.3 \cdot 10^6$. The result with this tuned controller compared to the old design can be seen in Figure 8.8.

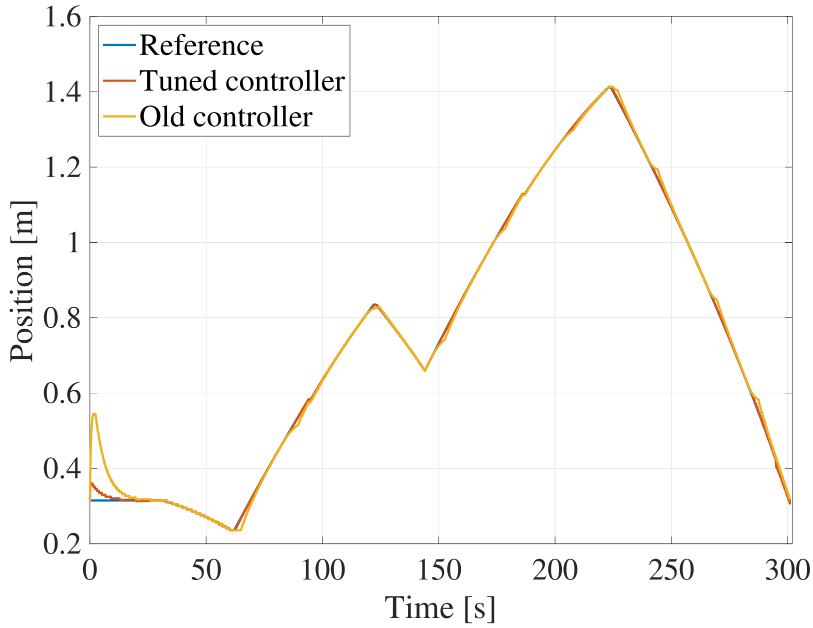

Figure 8.8: Comparison between old and tuned controller.

With a new rms error of 0.0046 m the tracking has improved significantly, thus a controller able to track within the allowable error has been designed.

8.2 Switching Algorithms

As the goal is not only do design a position tracking controller but also to reduce energy cost, the energy losses must also be evaluated. For the designed controller the switching losses (E_{sw}), throttling losses (E_{th}), total losses (E_{tot}), rms tracking error (e_{rms}) and number of force switches (NO_{sw}) are shown in Table 8.2.

e_{rms}	E_{sw}	E_{th}	E_{tot}	NO_{sw}
0.0046 m	3.57 MJ	11.35 MJ	14.92 MJ	2418

Table 8.2: Energy loss, tracking error and number of switches for designed controller

In the designed control structure a way of potentially reducing the energy losses is already available in form of the switching algorithm. The switching algorithm can potentially reduce the switching losses depending on how it is modified. The switching algorithm can be modified in two main ways, one is choosing the delay on how often the discrete force output can be updated. The second method is by modifying how the discrete force is chosen. In this thesis three different algorithms are using these modification methods are designed and tested and then compared to the designed PI controller, from now on called benchmark.

Sample Time

This algorithm simply increases the delay for how often the discrete output force can be updated. When increasing the delay of the controller the switching losses should in theory decrease as the delay would only allow a switch each time a sample occurs. Subsequently a higher sampling time could also have a negative impact on the position tracking as not being able to switch as frequently could increase the tracking errors.

Medium Switch Algorithm

In this algorithm the way the output force is chosen is modified. As mentioned in Section 4.4, the switching losses when switching between the 27 different force levels are lower if the intermediate pressure level is used to switch between HP to LP. Therefore the algorithm is set up to ensure that a switch from HP to LP never happens directly. This is done by comparing the new required force with the current force, if the force switch requires a pressure switch from HP to LP, or vice versa, the algorithm will only chose a force where the MP is used instead. This methods should therefore decrease the overall switching losses, as the switch from e.g. LP to MP to HP will be lower than lower than LP to HP energy wise. The downside of using this method is that it could potentially increase the overall number of switches, as it can require two switches to get the desired output force. Increasing the number of switches could result mechanical fatigue of the valves.

Force Band Algorithm

Lastly another switching method involving a force band is designed. Here the switch between forces will happen to the most energy efficient force within a defined force band. If the force reference is outside the allotted force band the force will switch to the closest available force without taking energy losses into account. The concept of the Force Band Algorithm can be seen in Figure 8.9.

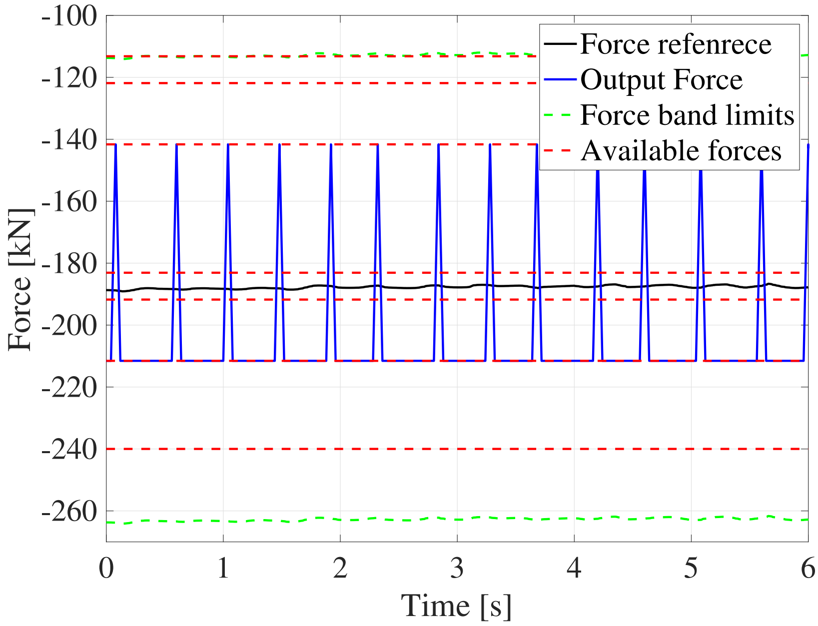

Figure 8.9: Force Band Algorithm with a force band of 75 kN.

On the figure the force reference, the force band limits and the output force generated from this algorithm can be seen together with the available force levels. The algorithm determines the most energy efficient switch to an available force within this force band and hence not just the closest to the reference.

The concept can mathematically be described as the following:

$$k = argmin\{|F_e(k_-)|, |F_e(k_i|, |F_e(k_+)|\} \tag{8.4}$$

In the above equation k is the new force state being switched to, F_e is force error and k_i is the current force state. Lastly the force states k_+ and k_- denotes the new force state associated with the smallest switching loss inside the force band for either the upper or lower force band limit. These force states are found by evaluating the minimum switching loss associated with the allowable forces.

$$\begin{aligned} k_- &= argmin\{E_{sw}(k)\}, k \in S_- \\ k_+ &= argmin\{E_{sw}(k)\}, k \in S_+ \end{aligned} \tag{8.5}$$

Where:

$$\begin{aligned} S_- &= \{K|F_{ref} - F_{fb} < \boldsymbol{F_{vec}} < F_{ref}\} \\ S_+ &= \{K|F_{ref} < \boldsymbol{F_{vec}} < F_{ref} + F_{fb}\} \end{aligned} \tag{8.6}$$

The energy equation used is the one derived in Section 4.4 and is given by:

$$E_{sw} = \sum_{i=1}^{3} \frac{1}{2} \Delta p^2 \frac{V_i(x_c)}{\beta} \tag{8.7}$$

8.3 Results

First the delay algorithm will be tested by using different sampling times. The algorithm has been tested with a sampling time of [0.045 0.05 0.06 0.07 0.08 0.12 0.16] s. The results showing the total switching loss, the RMS error, the total energy loss and the number of switches can be seen in the Figures below.

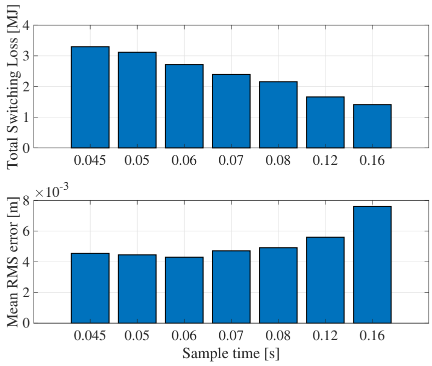

Figure 8.10: Bar plot showing total energy loss and RMS error for different sample times.

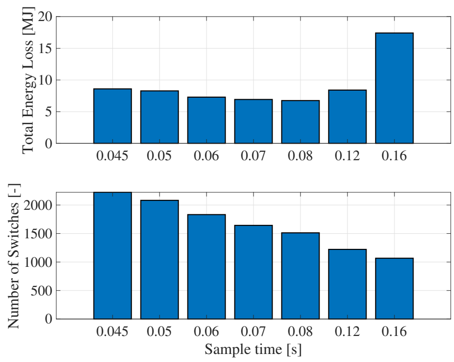

Figure 8.11: Bar plot showing total switching loss and number of switches for different sample times.

From figure 8.10 it can be seen that as the sampling time increases the switching losses decreases as expected. Furthermore the rms error increases which was also expected. When comparing the switching losses to the total energy loss in Figure 8.11 there are some discrepancies, as the total energy loss starts increasing, after a delay 0.12 s. This increase in the total energy loss is due to the throttling loses. This is believed to be due to the velocity of the cylinder. The velocity for sample time of 0.16 s and of 0.08 s can be seen in Figure 8.12. It is believed that these higher velocity spikes are due to the force having to switch between higher force levels due to the delay time. Therefore the output force is also compared which can be seen in Figure 8.13.

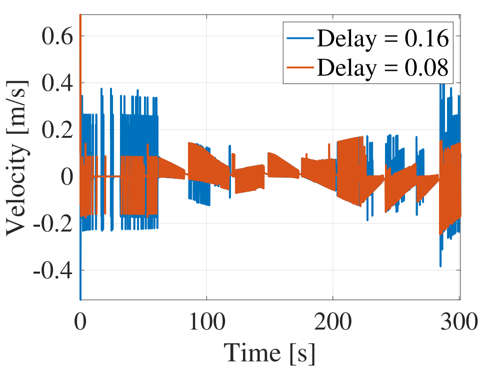

Figure 8.12: Comparison of velocity for a sample time of 0.08 s and 0.16 s.

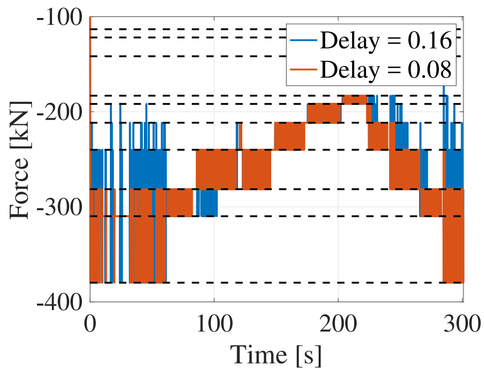

Figure 8.13: Comparison of output force for a sample time of 0.08 s and 0.16 s.

From Figure 8.12 it can be seen that the velocity is higher if a delay of 0.16 s is used compared to a delay of 0.08 s. This confirms the theory of the throttling losses being higher due to higher velocity spikes. Furthermore the theory of having high velocity spikes being caused by the higher force switches can been confirmed when looking at Figure 8.13 where it can be seen that when the velocity spikes are higher, the required force switch is higher, e.g. around 50 seconds.

From the results of the delay method it can be seen that energy losses can be reduced. However there is also a limit on how much the delay can be increased before the effect will be negative, due to the throttling losses.

The next algorithm tested is the Medium Switch Algorithm. This algorithm is tested alone but also in combination with the Sample Time algorithm. Meaning the it has been tested with a sampling time of [0.045 0.05 0.06 0.07 0.08 0.12 0.16] s. The results showing the total switching loss, the RMS error, the total energy loss and the number of switches can be seen in the Figures below.

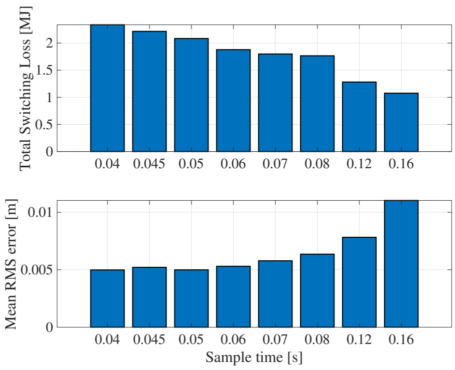

Figure 8.14: Bar plot showing total energy loss and RMS error for different sample times.

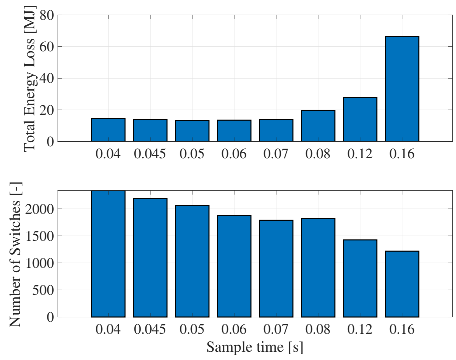

Figure 8.15: Bar plot showing total switching loss and number of switches for different sample times.

Looking at Figure 8.14 and 8.15 the same tendencies as with the delay method, where the switching loss decreases with an increasing sample time. Furthermore the total energy loss starts to increase after 0.08 s, which is due to the velocity as with the delay method. However a noticeable difference between two algorithms is the reduction in the switching losses. This can be seen in Figure 8.16 and 8.17 where a comparison of the two methods is shown.

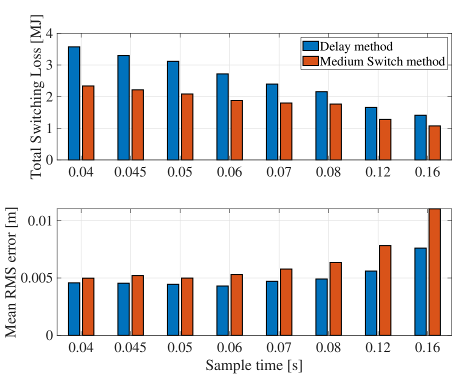

Figure 8.16: Bar plot showing total energy loss and RMS error for different sample times.

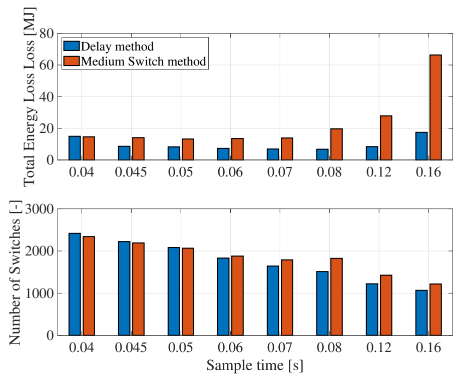

Figure 8.17: Bar plot showing total switching loss and number of switches for different sample times.

As it can be seen for all sampling times the switching losses are reduced compared to the Delay method. However for the Medium Switch method as the sample time increases the RMS error is increasing more than for the Delay method. The total energy loss is thus higher for the Medium Switch method due to the reasons of velocity and force reference discussed before.

An interesting observation is that with a sampling time of 0.06 s and above the number of switches are higher with the Medium Switch Algorithm than with the Delay method, but the total switching loss is lower. This means that just minimizing the amount of switches does not necessarily equal the most energy efficient option.

The next algorithm that is tested is the Force Band Algorithm. To test the influence of the force band size the following force bands where used in the testing [5 10 25 50 75 100 150 200] kN. The results showing the total switching loss, the RMS error, the total energy loss and the number of switches can be seen in the Figures below.

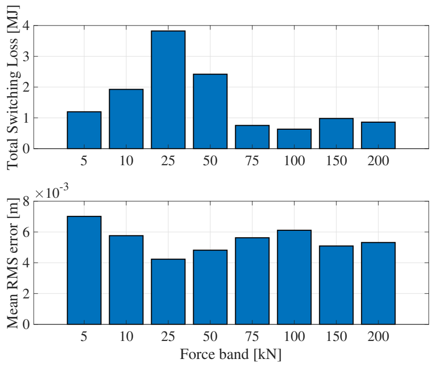

Figure 8.18: Bar plot showing total energy loss and RMS error for different force bands.

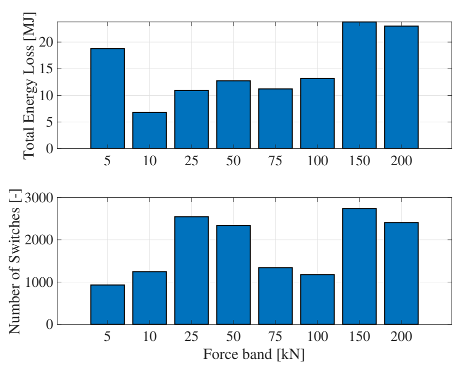

Figure 8.19: Bar plot showing total switching loss and number of switches for different force bands.

When looking at the results of Figure 8.18 and 8.19 no clear tendency can be seen from the data. As an example if looking at a force band of 5 kN and 25 kN, when comparing the switching losses a force band of 5 kN results in the lowest switching loss. However with a force band of 25 kN the overall energy losses are significantly lower than with the lower force band. Subsequently if looking at a force band of 50 kN and 75 kN the force band with the lowest switching loss is having the lowest total loss (75 kN). As the different observations can be seen with different force bands it seems there is no logical way of determining how to choose the best force band.

From the Force Band Algorithm it is found that the force band with the lowest total energy loss, is with a force band of 10 kN. To test the effect of the the sampling time combined with the Force Band Algorithm further test are performed. In the new test a sampling time of [0.045 0.05 0.06 0.07 0.08 0.12] s are used in combination with a force band of 10 kN. The results showing the total switching loss, the RMS error, the total energy loss and the number of switches can be seen in the Figures below.

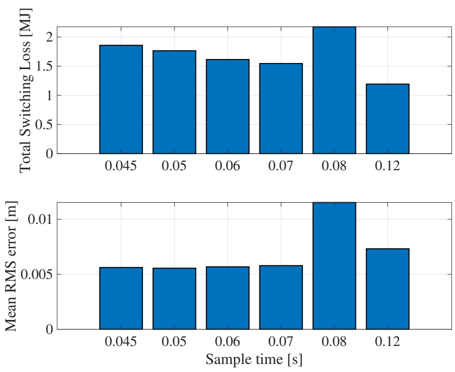

Figure 8.20: Bar plot showing total energy loss and RMS error for different sample times.

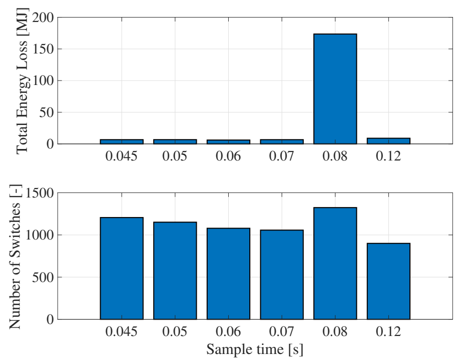

Figure 8.21: Bar plot showing total switching loss and number of switches for different sample times.

From Figure 8.21 it can be seen that with a sample time of 0.08 s it has a huge total energy loss caused by the throttling losses. This is again believed to be due to the velocity of the cylinder. As it was shown for the delay method, the velocity and force switches are shown in Figure 8.22 and 8.23.

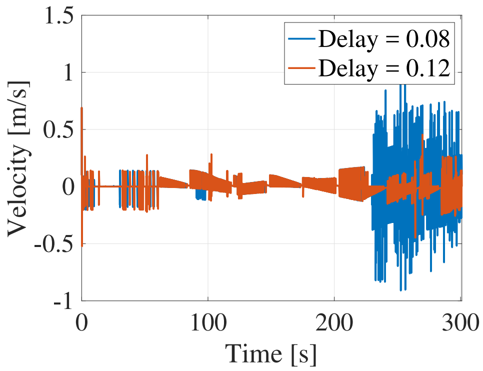

Figure 8.22: Comparison of velocity for a sample time of 0.08 s and 0.12 s.

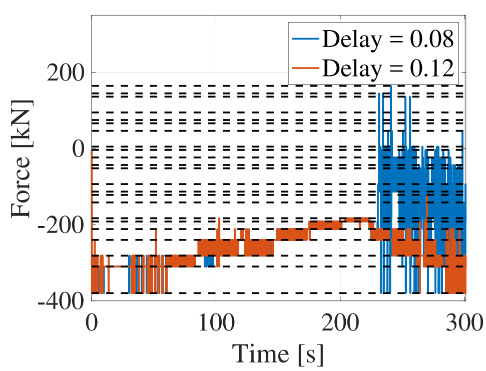

Figure 8.23: Comparison of output force for a sample time of 0.08 s and 0.12 s.

As it can be seen in the figures again the velocity spikes and the output force increases for a sample time of 0.08 s resulting in higher throttle losses. However as this increase is centered around a specific area it is not believed to due tracking problems caused by the delay. Further investigation showed that the one of the cylinder chamber pressures reached a value of 0 when these spikes occurred. This can be seen in Figure 8.24.

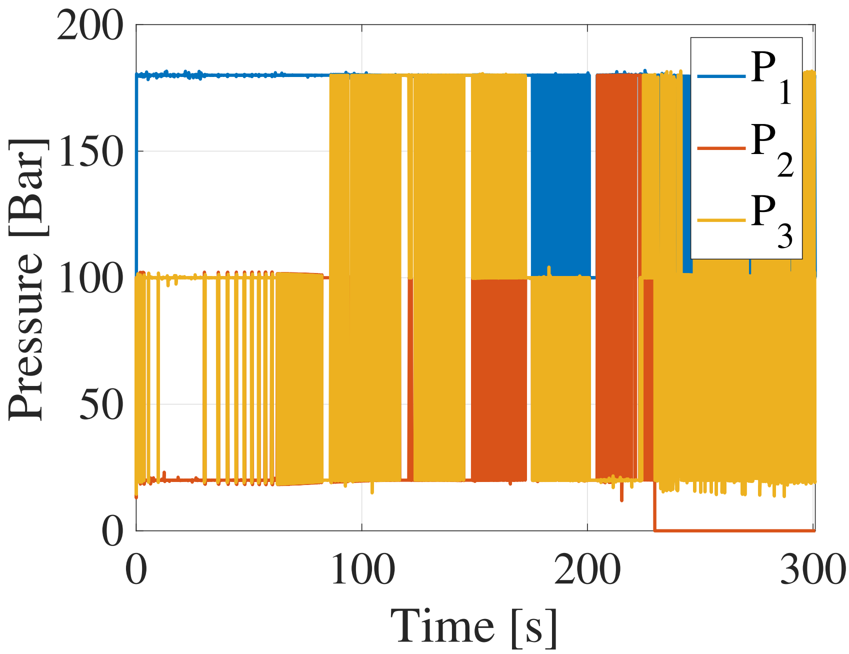

Figure 8.24: Cylinder chamber pressures.

As reaching a value of zero should be impossible it is believed to happen due to a simulation error. As no clear fix for this was found this data point is has been omitted in the following figures to better compare the energy loss for the other data points.

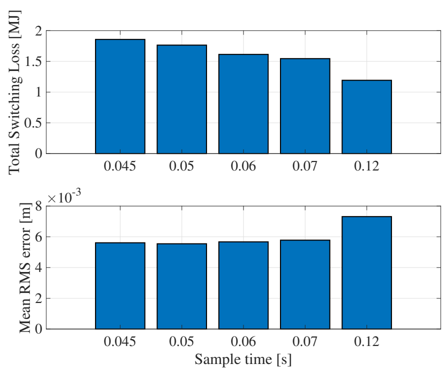

Figure 8.25: Bar plot showing total energy loss and RMS error for different sample times.

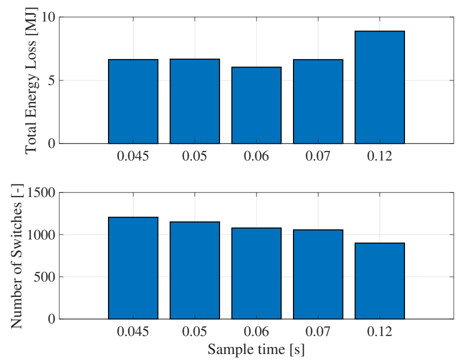

Figure 8.26: Bar plot showing total switching loss and number of switches for different sample times.

As it can be seen having a higher sampling time also reduces the energy losses as with the other two methods where the sampling time was varied. If all three algorithms are compared it can be seen that the using the Force Band Algorithm is the best option.

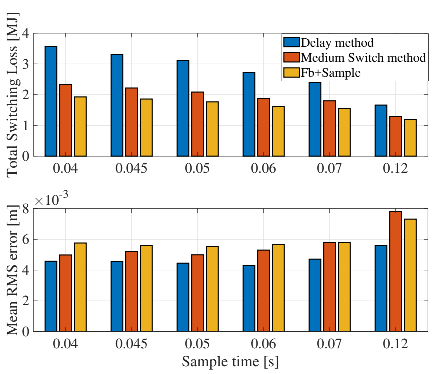

Figure 8.27: Bar plot showing total energy loss and RMS error for different sample times.

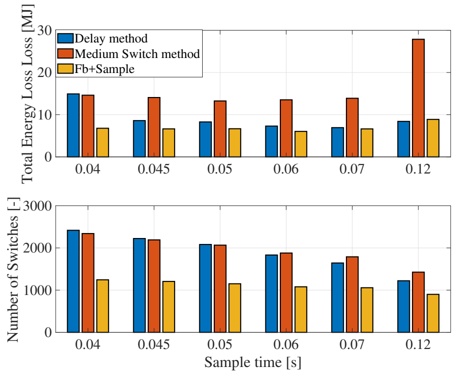

Figure 8.28: Bar plot showing total switching loss and number of switches for different sample times.

However when comparing the result of the total energy loss for all the different algorithms, it is not only choosing the option with the lowest switching loss that will result in the most energy efficient controller. This can be seen in Figure 8.29 where the most energy efficient result from each test are compared together with the benchmark.

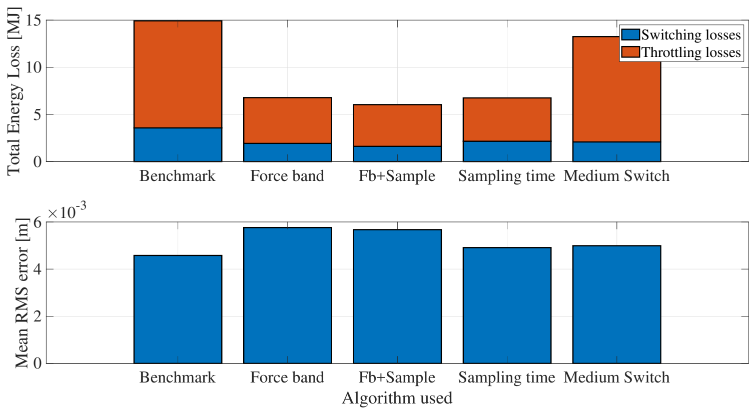

Figure 8.29: Comparison of tracking abilities for the two force shifting algorithms.

In the figure the total energy loss is split up into the switching losses and throttling losses. All four algorithms has a similar RMS error. From the results it can be seen that if a switching algorithm is used to minimize the energy loss, the option combining a force band of 10 kN combined with a sampling time of 0.06 s results in the lowest over all energy loss. The reduction of the total energy loss compared to the benchmark is at 59 %.

The tracking result from the best of all four algorithms together with the benchmark and the reference can be seen in Figure 8.30. This is plotted together with the error between the position and the reference to see the difference more clearly in Figure 8.31 .

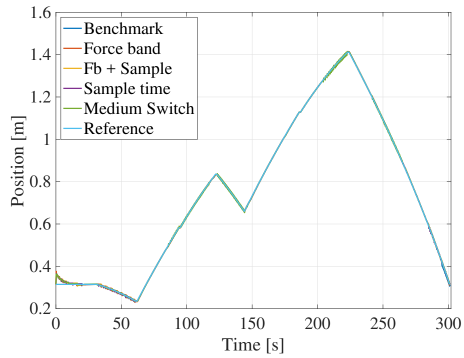

Figure 8.30: Tracking result of different algorithms.

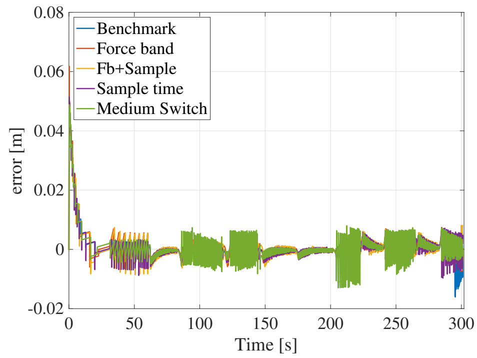

Figure 8.31: Position error of different algorithms.

When zooming in on the tracking figure it can clearly be seen why the tracking is worse when using the different algorithms. This is seen in Figure 8.32. Furthermore from 8.33 it can be seen that the areas with small errors correspond to areas where the output force is switching between close discrete forces. Similarly high errors occur when swathing between higher force levels.

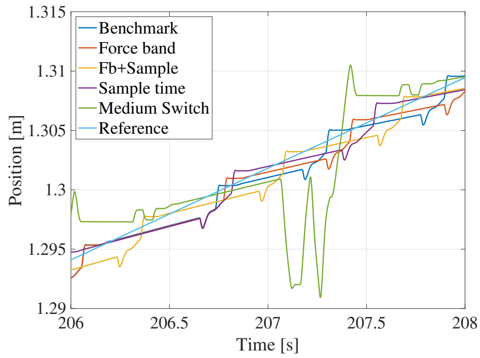

Figure 8.32: Zoomed version of tracking result for the different algorithms.

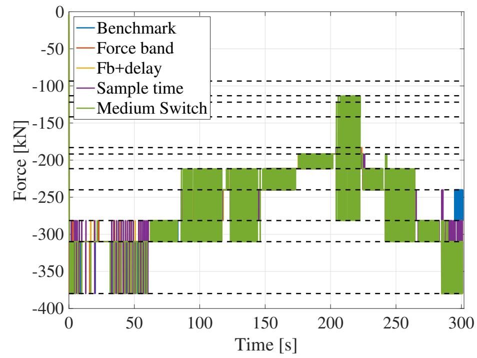

Figure 8.33: Output force of different algorithms.

From this it can then be concluded that the trajectory of the position will influence both the RMS error and the total energy loss. If the continuous force reference required to follow the operation trajectory are close to the available discrete forces both the RMS error and the total energy loss could be reduced further using these designed algorithms.

9 | Valve switching algorithm

In this chapter it will be investigated if the throttling losses can be reduced if some valve algorithm is implemented. The purpose of this algorithm is to chose the number of open valves in each DFCU under operation.

From Chapter 8 it was shown that using a switching algorithm with a force band 10 kN combined with a sampling time of 0.06 s resulted in lowest total energy loss from the conducted simulations. Therefore this will be used as a benchmark for the new valve algorithms.

From the investigation performed in the previous chapter it was noted that for all algorithms that the velocity had a lot of spikes. This can be seen in Figure 9.1 where the force band benchmark is shown together with the velocity reference.

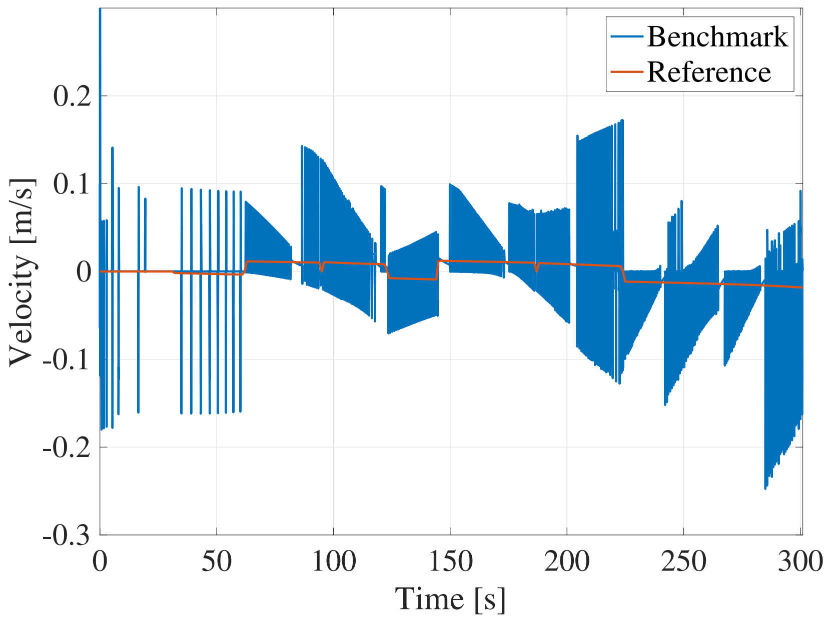

Figure 9.1: Velocity of the benchmark together with velocity reference.

For the simulations done with the switching algorithms all valves in the DFCU were turned on and off. By implementing an algorithm that can control the number of valves opened, the hope is that these velocity oscillations can be reduced.

In theory changing the number of valves that are opened in the DFCU, is equivalent to throttling a proportional valve. Throttling a proportional valve would normally increase the throttling losses. However when looking at Eq. 9.1 it can be seen that the velocity is cubed and the number of opened valves is squared.

$$E_{th} = \sum_{i=1}^{3} \frac{|A_i v_c|^3}{(n_i k_v)^2} \tag{9.1}$$

To reduce the velocity the number of valves will also have to be reduced. If the number of valves is reduced the denominator will decrease thereby increasing the throttling losses. However reducing the velocity will reduce the nominator and thereby also the throttling losses. What will be investigated is the hypothesis that the reduction of velocity spikes will result in an overall decrease of the throttling losses even if the denominator as a results is also decreased due to the cubed and squared realtion.

The control structure of the system when also implementing the valve algorithm can be seen in Figure

9.2.

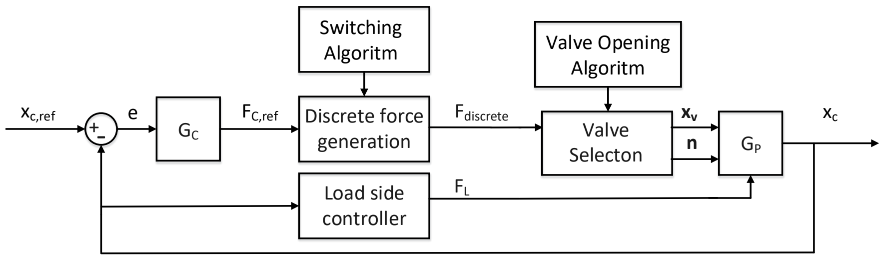

Figure 9.2: Block diagram for the control system with force controller and valve switching algorithm.

Two different algorithms will be developed in order to test the above hypothesis. These algorithms are the Minimum Valve Algorithm and the Switch Valve Algorithm.

Minimum Valve Algorithm

The Minimum Valve Algorithm is fairly simple, it is designed such that only a single valve for chamber 2 and 3 are opened, while 2 valves are opened in the DFCU for chamber 1. This is done in order to match the input and output flows for both sides of the cylinder. By using the smallest amount of opened valves the available flow will be reduced which will reduce the velocity.

Switch Valve Algorithm

For this algorithm each time a DFCU is opened only valve is opened. The algorithm will then increase the number of opened valves if the velocity is smaller than the reference.

Furthermore if the velocity gets larger than the reference the number of opened valves will decrease.

Results

In Figure 9.3 and 9.4 the velocity for the benchmark, the reference and the two algorithms can be seen.

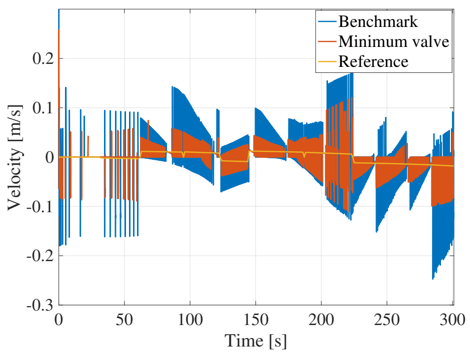

Figure 9.3: Benchmark velocity compared to Velocity using Minimum valve algorithm.

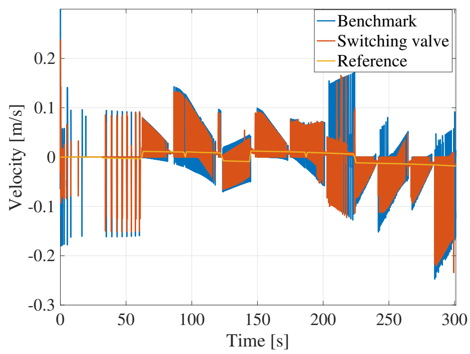

Figure 9.4: Benchmark velocity compared to Velocity using Switch valve algorithm.

From the figure it can be seen that both algorithms reduce the velocity, however they both still oscillate around the reference. The Minimum algorithm can be seen to reduce the velocity the most.

In Figure 9.5 and 9.6 the RMS position error and the throttling losses can be seen for the benchmark and the two algorithms.

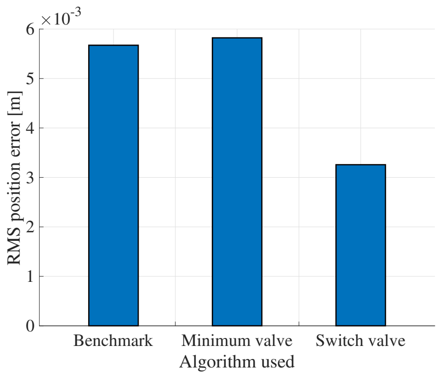

Figure 9.5: RMS position error caparison for the new algorithms.

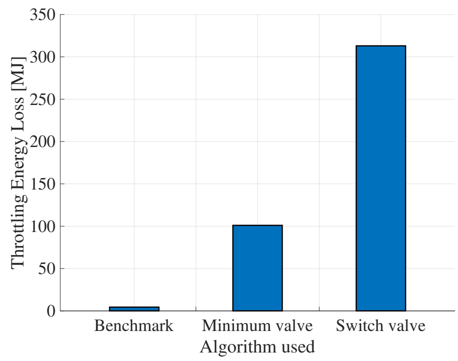

Figure 9.6: Throttling loss for the new algorithms.

As it can be seen from Figure 9.5 by introducing these two algorithm the RMS error is reduced if the Switching valve is used and slightly increased with the Minimum valve algorithm. These results were expected as for the Minimum algorithm, if the flow request in order to track is higher than what can be delivered with only one opened valve, the tracking would decrease. Similarly if the valves can throttle the velocity error compared to the reference would decrease, which would decrease position overshoots and thereby improving the RMS error. However if looking at Figure 9.6 it can be seen that the throttling losses does not improve. The throttling losses of the two algorithms increase significantly for the Minimum algorithm and massively for the Switch algorithm. Therefore it must be concluded that the velocity reduction gained is not enough to reduce the overall throttling losses gained by reducing the number of valves. Therefore valve switching algorithms should not be implemented if energy efficient tracking control is wanted. However if only the RMS position error is of interest these algorithms can potentially improve the results for DDC systems.

10 | Conclusion

In this thesis it was investigated if a control structure could be developed that was able to track a position reference while minimizing the energy loss. Such a control structure will always have to compromise between energy loss and the tracking performance. In order to be able to determine if the controller results in a good compromise i.e. if the energy savings are worth the increased error of the position tracking, control requirements based on a real life system was introduced.

The real life system considered in this thesis was chosen to be a Knuckle Boom crane. From the industry it was found that such a crane had an allowable root mean square (RMS) error of 3 cm for the end effector. This error was translated into an allowable error for the multi-chambered cylinder used in this thesis. The allowable error for the cylinder is $\pm$ 2 cm. If the energy savings does not result in a higher tracking RMS error than this, the compromise is considered good.

The multi-chambered cylinder that is considered, is connected to three different pressure lines. The cylinder consists of three chambers and each chamber is connected to the pressure lines by three digital flow control units (DFCU). As each DFCU is controlled individually the system will effectively be a multiple input single output (MISO) system. As three DFCU's is connected to each chamber a constraint to the control problem was added. The constraint was to only open a single DFCU for each chamber at a time to avoid unnecessary energy losses by shortening the system. As the system is consisting of three chambers and three pressure lines this results in the cylinder being able to produce 27 discrete output force levels. Therefore the controller to be designed has to be able to handle discrete force outputs, multiple inputs and the constraint of only opening one DFCU for each chamber at a time.

A linear quadratic controller was developed as such controller structure is capable of handling MISO systems. This controller was able to track the position reference however the controller was not able to obey the constraint of only opening one DFCU per chamber at a time. Therefore this controller was deemed not viable for such a system.

A combination of a PI controller combined with a force selecting algorithm could be designed without violating the constraints. This controller was able to track the position reference with a RMS error of 0.0046 m and a total energy loss of 14.92 MJ. In order to reduce the energy loss, different force switching algorithms was designed and tested. Using an algorithm with a sample time of 0.06 s consisting of choosing the most energy efficient force within a force band of 10 kN in each direction resulted in the lowest energy loss. By using this algorithm the total energy loss was reduced by 59% while having a RMS position error of 0.0057 m.

Furthermore another algorithm was implemented in order to test, if by choosing the amount of opened valves in the open DFCU would reduce the total energy loss further. However the designed algorithm only increased the total energy loss and it was concluded that such an algorithm could not be used.

To conclude a PI controller combined with a force switching algorithm can be developed in order to track a position reference within an allowable error while still being able to reduce the total energy loss. One problem that this control structure has, is the difficulty of tuning it. No clear relationship between the controller gains and algorithm parameters makes the tuning of the controller heavily reliant on trial and error.

11 | Future works

In this chapter some further work which has not been done in this thesis will be outlined.

Further Analysis of Force Switching Algorithm

It was concluded in this Thesis that by using a linear PI controller in combination with switching logic the energy losses were reduced while still being able to track within the allowable error. However some deeper analysis of the results could be performed in order to get a better understanding of control method:

Reference Trajectory

One conclusion that was made was that that the trajectory of the application had an influence on the RMS error and the energy consumption. Therefore it could be interesting to investigate different trajectories to if a relation can be found.

Different Controller Gains

The results of the force switching algorithms were only performed using one designed controller. However as the system is tested with various sample times it could be interesting to investigate how different controller gains affects the results for the different algorithms. For example for higher delay a less aggressive controller could improve the tracking and energy losses.

Inertia of the System

For the test performed some algorithms resulted in high velocity spikes which produced high throttling losses. The simulated system had a low inertia compared to a real system and hence it could be interesting to investigate how the velocity spikes would look if a system with a higher inertia is tested.

Velocity controller

As a big contribution to the total energy losses came from the throttling losses it could be interesting to see if designing a velocity controller instead of a position controller could improve the energy losses.

Implementation and test of algorithms on physical setup

The results gained in this thesis are only based on simulations of the validated model. It would be interesting to see if the same results could be obtained using the real system. As the model is validated to a satisfactory point it is expected that the results should be somewhat similar, however small changes in the system parameters could potentially have big impacts.

Bibliography

[1] K. F. Group, "Offshore cranes." Website, 2016.
https://www.kenz-figee.com/offshore-cranes.

[2] Moog, "D634-p series." Data sheet, 2009.
https://www.moog.com/literature/ICD/D634PseriesvalvesE.pdf.

[3] P. H. Corporation, "Series d1fp." Data sheet, 2008.
https://www.parker.com/literature/Germany/CD_Rom%20Bauteilfreigabeliste%20Mechanik%20Hydraulik%20UK/D_1FP%20UK.pdf.

[4] V. Donkov, T. Andersen, M. Kjeld Ebbesen, and H. Pedersen, "Applying digital hydraulic technology on a knuckle boom crane," *The Ninth Workshop on Digital Fluid Power*, 09 2017.

[5] S. Ketelsen, L. Schmidt, V. Donkov, and T. Andersen, "Energy saving potential in knuckle boom cranes using a novel pump controlled cylinder drive," *Modeling, Identification and Control: A Norwegian Research Bulletin*, vol. 39, pp. 73–89, 04 2018.

[6] M. Linjama, *Digital Hydraulics slides, MEC-E5004 Fluid Power Systems, Tampere University Of Technology*, 2016.
hhttps://mycourses.aalto.fi/pluginfile.php/572294/mod_resource/content/1/Digital%20Hydraulics%20lecture%20slides.pdf.

[7] M. Linjama, "Digital fluid power state of the art," *The Twelfth Scandinavian International Conference on Fluid Power*, 05 2011.

[8] A. Laamanen, M. Linjama, and M. Vilenius, "On the pressure peak minimization in digital hydraulics," *The Tenth Scandinavian International Conference on Fluid Power, May 21-23, 2007, Tampere, Finland, SICFP 07*, pp. 107–121, 2007.

[9] M. Linjama, H.-P. Vihtanen, A. Sipola, and M. Vilenius, "Secondary controlled multi-chamber hydraulic cylinder," *The 11th Scandinavian International Conference on Fluid Power SICFP 09, Linköping, Sweden, June 2-4 2009*, p. 15 p, 2009.

[10] M. Huova, A. Aalto, M. Linjama, K. Huhtala, T. Lantela, and M. Pietola, "Digital hydraulic multi-pressure actuator the concept, simulation study and first experimental results," *International Journal of Fluid Power*, vol. 18, pp. 1–12, 03 2017.

[11] A. Hansen, M. Asmussen, and M. Bech, "Energy optimal tracking control with discrete fluid power systems using model predictive control," *Proceedings of 9th*

Workshop on Digital Fluid Power, DFP 2017", publisher = "Department of Energy Technology, Aalborg University, 9 2017.

[12] H. Pedersen, R. Hansen, A. Hansen, T. Andersen, and M. Bech, "Design of full scale wave simulator for testing power take off systems for wave energy converters," *International Journal of Marine Energy*, vol. 13, p. 130–156, 4 2016.

[13] R. Wolfson, *Essential University Physics Volume 2*. No. ISBN: 978-1-292-021027 in 2. Edition, Pearson Education Limited, 2014.

[14] A. Nielsen, J.-K. Langkjær, and C. Richter, "Secondary control of discrete displacement cylinder," tech. rep., Aalborg University, 2016.

[15] A. H. Hansen, "Fluid power system," *Lecture note*, 2017.

[16] A. Hansen, H. Pedersen, and R. Hansen, "Validation of simulation model for full scale wave simulator and discrete fuild power pto system," *Proceedings of the 9th JFPS International Symposium on Fluid Power*, 10 2014.

[17] A. Hansen and H. Pedersen, "Energy cost of avoiding pressure oscillations in a discrete fluid power force system," *Proceedings of the ASME/BATH 2015 Symposium on Fluid Power and Motion Control, FPMC 2015*, 10 2015.

[18] G. KG, "Positioning system with dgps." Data sheet, 2000. https://www.goetting-agv.com/dateien/downloads/S_G57650_TD_EI_A_R01.pdf.

[19] C. L. Philips and J. M. Parr, *Feedback Control Systems*. No. ISBN: 978-0131866140 in 5. Edition, Pearson, 2011.

A | Valve Gain Experiments

During the validation of the non-linear model in Chapter 5, it were discovered that using the valve gains from the data sheets for the two load side valves i.e. the Moog and Parker valves, did not give results that fit the experiments performed.

Two experiments are therefore performed, one for each of the two valves, to calculate the valve gain for each valve. The idea behind the experiments are to calculate the valve gain for many different valve voltage inputs, and gathering all the results into a look-up table that is then used during the simulations when validating the model.

To calculate the valve gain the orifice equation is used:

$$Q = k_v(x_{valve})\sqrt{\Delta P} \tag{A.1}$$

Where

x_{valve}	is the normalized valve input for either the Parker or Moog valve	[-]

The flow Q can be written as the velocity of the cylinder divided by the cross-sectional area of the load side cylinder piston, and the valve gain is therefore calculated as:

$$K_v(x_{valve}) = \frac{v_{cyl}}{A_p\sqrt{\Delta P}} \tag{A.2}$$

For the experiment with the Moog valve, inputs are given from -10 volt to 10 volt with an increment of 0.2 volt. For each input given, the velocity of the cylinder together with the pressure on both sides of the valve were measured. Meaning that both pressures for chamber A and B after the valve manifold is measured together with the supply pressure. To calculate the valve gain at each input a mean value for the pressures and velocity were used. These mean values were taken in the period where the cylinder had reached a steady state velocity. Due to different flow direction depending on the valve inputs the pressure differences used in the equation were $P_s - P_B$ for negative valve inputs and for positive inputs $P_s - P_A$. This procedure were done three times for the Moog valve and a mean value for all the experiments were found. The results can be seen in the following figure:

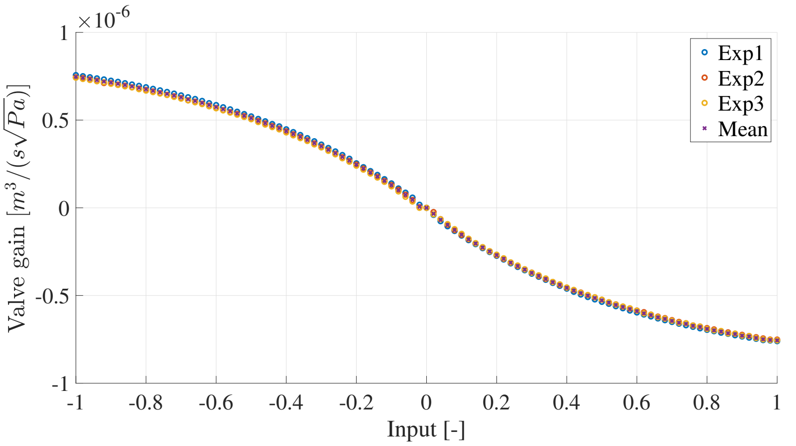

Figure A.1: Calculated valve gains for the Moog valve and the mean valve gains.

If an input is used, that is not part of the experimental collected data points used for the look-up table, linear interpolation between the two nearest points are used to find the corresponding valve gain.

For the Parker valve a very similar procedure as for the Moog valve were used. The difference between the Parker valve experiment and the Moog experiment is that for the Parker experiment the absolute value for the valve gain is calculated. This resulted in the look-up table having a similar shape as in the data sheet an therefore eased the implementation into the model. Furthermore only inputs from -2.3 volt to 2.3 volt were given, with an increment of 0.1 volt. The reason for this is twofold, firstly it were not possible to get a steady state velocity to calculate the valve gain at higher inputs. Secondly higher valve inputs are not expected for the position control, and valve gains for higher inputs are therefore not needed. The results for the Parker valve is seen in Figure A.2

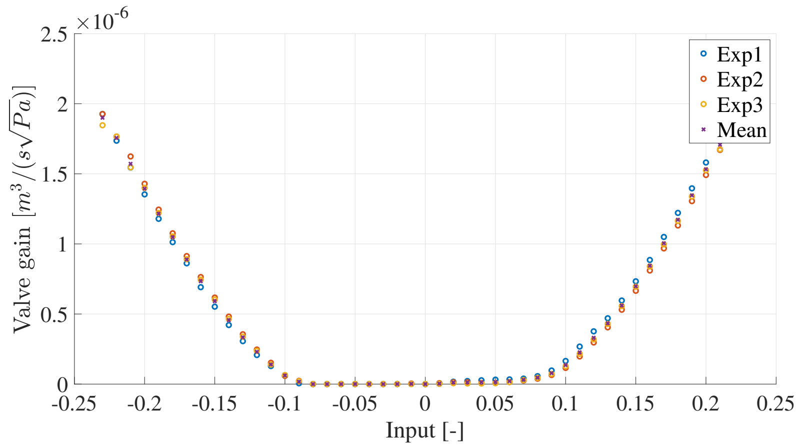

Figure A.2: Calculated valve gains for the Parker valve and the mean valve gains.

As is the case for the Moog valve linear interpolation is also used for the Parker valve for inputs not used in the experiment.

B Model Parameters

In this appendix all parameters used in the model is presented. The parameters have been split up into four tables. One for the DDC side in Table B.1, one for general parameters in Table B.2, one for the transmission line model B.4 and one for the load side in Table B.3.

DDC side parameters			
Symbol	**Description**	**Value**	**Unit**
P_5	Pressure in chamber 5	$1.01 \cdot 10^5$	[Pa]
P_h	Pressure for high pressure line	$180 \cdot 10^5$	[Pa]
P_m	Pressure for medium pressure line	$100 \cdot 10^5$	[Pa]
P_l	Pressure for low pressure line	$20 \cdot 10^5$	[Pa]
$V_{1,0}$	Dead volumen for chamber 1	$48 \cdot 10^{-3}$	[m^3]
$V_{2,0}$	Dead volumen for chamber 2	$1.1 \cdot 10^{-3}$	[m^3]
$V_{3,0}$	Dead volumen for chamber 3	$2.3 \cdot 10^{-3}$	[m^3]
A_1	Cross-sectional area for chamber 1	$235 \cdot 10^{-4}$	[m^2]
A_2	Cross-sectional area for chamber 2	$122 \cdot 10^{-4}$	[m^2]
A_3	Cross-sectional area for chamber 3	$87.4 \cdot 10^{-4}$	[m^2]
A_{idle}	Cross-sectional area for chamber 5	$135 \cdot 10^{-4}$	[m^2]
x_{min}	Minimum cylinder position	0	[m]
x_{max}	Maximum cylinder position	2	[m]
$k_{v,c}$	Valve gain for each on/off valve in the DFCU	$1 \cdot 10^{-6}$	[$m^3/s/Pa^{0.5}$]
on_{delay}	Delay between input given to valve opens	$9 \cdot 10^{-3}$	[s]
off_{delay}	Delay between input stopped to valve closing	$9 \cdot 10^{-3}$	[s]
$\omega_{n,c}$	Natural frequency for the digital valve dynamic	630	[rad/s]
ζ_c	Damping for the digital valve dynamic	0.95	[-]
$n_{v,1}$	Number of valves in each DFCU for chamber 1	18	[-]
$n_{v,2}$	Number of valves in each DFCU for chamber 2	10	[-]
$n_{v,3}$	Number of valves in each DFCU for chamber 3	8	[-]

Table B.1: DDC side parameters.

Transmission line parameters			
Symbol	**Description**	**Value**	**Unit**
κ	Adiabatic constant	1.4	[-]
β_F	Bulk modulus for the fluid	$7500 \cdot 10^5$	[Pa]
μ	Dynamic viscosity of the oil	0.0406	[Pa s]
ρ	Density of the oil	877.9	[kg/m^3]
$F_{coulumb}$	Coulumb friction	11000	[N]
B_c	Viscous friction	80000	[N s/m]
γ_{fric}	slope coeffecient for the friction	$1 \cdot 10^{-4}$	[-]
m_{tot}	Total mass of the cylinder system	2750	[kg]
\$\epsilon_{0}	volumetric ratio of air in the oil	0.01	[-]

Table B.2: General parameters.

Load side parameters			
Symbol	**Description**	**Value**	**Unit**
A_P	Cross-sectional area for piston	$236.405 \cdot 10^{-4}$	[m^2]
$V_{A,0}$	Dead volume for chamber A	$39.6 \cdot 10^{-3}$	[m^3]
$V_{B,0}$	Dead volume for chamber B	$39.6 \cdot 10^{-3}$	[m^3]
P_t	Tank pressure	$0.2 \cdot 10^5$	[Pa]
P_s	Supply pressure	$280 \cdot 10^5$	[Pa]
$k_{v,M}$	Moog valve gain	See Figure 5.3	[m^3/s/Pa$^{0.5}$]
$k_{v,P}$	Parker valve gain	See Figure 5.4	[m^3/s/Pa$^{0.5}$]
$\omega_{n,M}$	Natural frequency for Moog valve dynamics	400	[rad/s]
ζ_M	Damping for Moog valve dynamics	0.8	[-]
$\omega_{n,P}$	Natural frequency for Parker valve dynamics	250	[rad/s]
ζ_P	Damping for Parker valve dynamics	0.8	[-]

Table B.3: Load side parameters.

Transmission line parameters			
Symbol	**Description**	**Value**	**Unit**
$n_{line,1,H}$	Number of hose elements in transmission line 1	4	[-]
$d_{1,H}$	Diameter of the hose in transmission line 1	$3.81 \cdot 10^{-2}$	[m]
$L_{1,H}$	Length of each hose element in transmission line 1	1.0875	[m]
$\xi_{1,1}$	Fitting coefficient at the start of transmission line 1	0.7	[-]
$\xi_{1,2}$	Fitting coefficient at the start of transmission line 1	0.45	[-]
$\xi_{1,3}$	Fitting coefficient at the end of transmission line 1	0.45	[-]
$n_{line,2,H}$	Number of hose elements in transmission line 2	2	[-]
$d_{2,H}$	Diameter of the hose in transmission line 2	$3.18 \cdot 10^{-2}$	[m]
$L_{2,H}$	Length of each hose element in transmission line 2	0.675	[m]
$\xi_{2,1}$	Fitting coefficient at the start of transmission line 2 for the hose	0.35	[-]
$n_{line,2,P}$	Number of pipe elements in transmission line 2	2	[-]
$d_{2,P}$	Diameter of the pipe in transmission line 2	$3.81 \cdot 10^{-2}$	[m]
$L_{2,P}$	Length of each pipe element in transmission line 2	0.6	[m]
$\xi_{2,2}$	Fitting coefficient between hose and pipe for transmission line 2	0.35	[-]
$\xi_{2,3}$	Fitting coefficient at the end of transmission line 2 for the pipe	0.35	[-]
$n_{line,3,H}$	Number of hose elements in transmission line 3	2	[-]
$d_{3,H}$	Diameter of the hose in transmission line 3	$3.18 \cdot 10^{-2}$	[m]
$L_{3,H}$	Length of each hose element in transmission line 3	0.85	[m]
$\xi_{3,1}$	Fitting coefficient at the start of transmission line 3 for the hose	0.45	[-]
$\xi_{3,2}$	Fitting coefficient at the start of transmission line 3 for the hose	0.35	[-]
$n_{line,3,P}$	Number of pipe elements in transmission line 3	2	[-]
$d_{3,P}$	Diameter of the pipe in transmission line 3	$3.81 \cdot 10^{-2}$	[m]
$L_{3,P}$	Length of each pipe element in transmission line 3	0.75	[m]
$\xi_{3,3}$	Fitting coefficient between hose and pipe for transmission line 3	0.35	[-]
$\xi_{3,4}$	Fitting coefficient at the end of transmission line 3 for the pipe	0.35	[-]
$\xi_{3,5}$	Fitting coefficient at the end of transmission line 3 for the pipe	1.2	[-]

Table B.4: Transmission line parameters.

C | Valve Splitting Algortihm

In this Appendix the valve splitting algorithm used in the control of the load side. The algorithm was developed in [14] and the derivation of the algorithm will not be explained.

The purpose of the algorithm is to split the equivalent input x_{eq} used in the control, into a control signal for both the Moog and Parker valve.

The Algorithm used can be seen here in the following equations:

$$x_{v,M} = \begin{cases} \frac{c_{m,max}}{2}(2 - \frac{c_{x,lim}}{|x_{eq}|}) \cdot sign(x_{eq}) & , \quad |x_{eq}| \geq c_{c,lim} \\ \frac{c_{m,max}}{2c_{x,lim}} x_{eq} & , \quad |x_{eq}| < c_{x,lim} \end{cases} \tag{C.1}$$

$$x_{v,P} = \begin{cases} x_{eq} & , \quad |x_{eq}| \geq c_{c,lim} \\ x_{eq} & , \quad |x_{eq}| < c_{x,lim} \end{cases} \tag{C.2}$$

Where:

$c_{m,max}$	is a constant determining the maximum output of the Moog valve	[-]
$c_{x,lim}$	is a constant determining the dead-band limit for the Parker valve	[-]

Using this algorithm the equivalent valve gain can be calculated as:

$$K_v(x_{eq}) = K_{v,M}(x_{v,M}) + K_{v,P}(x_{v,P}) \tag{C.3}$$

To determine the valve gain for each of the two load-side valves the experimental results for the valve gain found in Appendix A are used.

A polynomial fit is done on both of the experiment data-sets so that all inputs can be used. In order to make sure the valve gain for the Parker valve did not reach too high values during the polynomial fit, artificial experiment results where added for the maximum and minimum inputs that can be given. These data points values are the rated maximum valve gains for norminal flow, found in the data sheet.

The polynomial fits together with the data-points can be seen in the following figures:

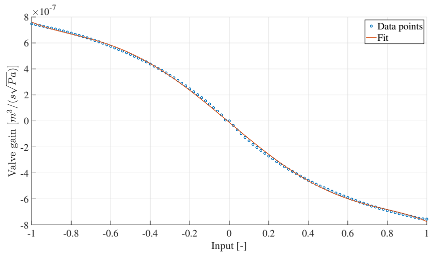

Figure C.1: Data-points together with the polynomial fit for the Moog valve.

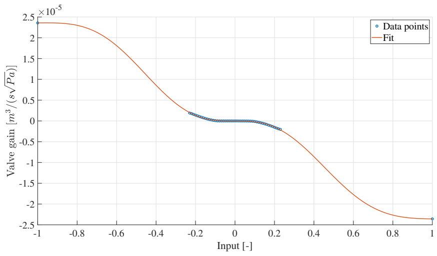

Figure C.2: Data-points together with the polynomial fit for the Parker valve.

Using the algorithm the two valve inputs given to the Parker and Moog valve as a function as the equivalent input can be seen in figure C.3

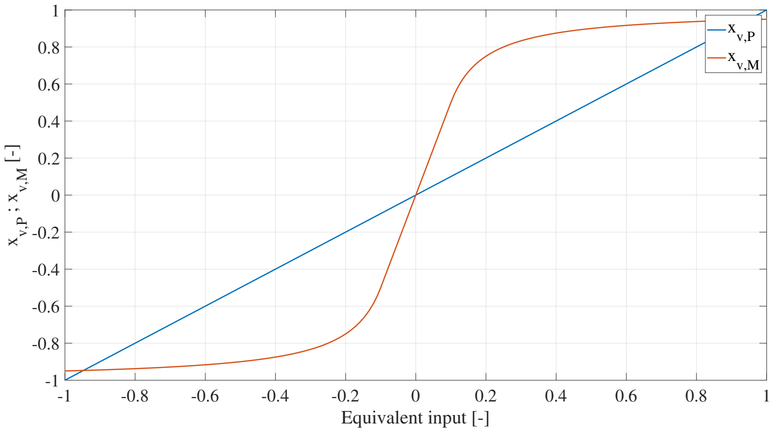

Figure C.3: Inputs to both the Parker and Moog valve as a function of the equivalent input.

Using these two inputs the valve gains together with the equivalent valve gain can be seen in the following figure.

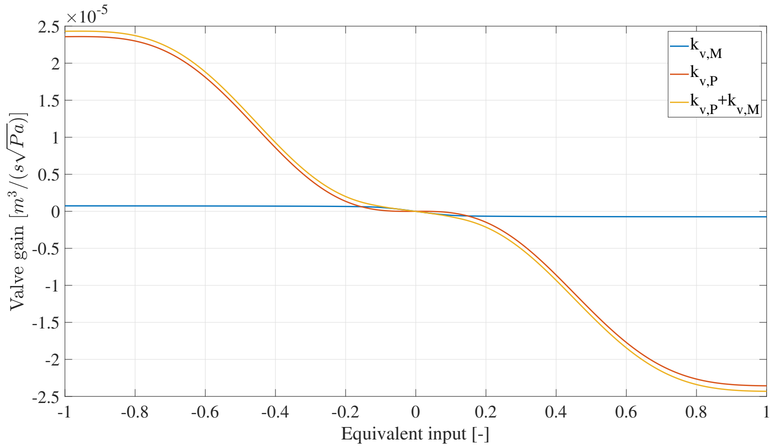

Figure C.4: Valve gains as a function of the equivalent input and individual inputs.

D LQC design for the Digital Displacement Cylinder

In order to design a LQC the non-linear model has to be linearized. The equations used to linearise the DDC side system is the ones derived in Chapter 4. It is the continuity equations (Eq. D.1), the flow equations for each chamber (Eq. D.2) and the equation for movement based on Newtons Second law (Eq. D.3).

$$\begin{aligned}
\dot{p}_1 &= \frac{\beta_{eff}(p_1)}{V_{1.0} - x_c A_1}(Q_1 + \dot{x}_c A_1) \\
\dot{p}_2 &= \frac{\beta_{eff}(p_2)}{V_{2.0} + x_c A_2}(Q_2 - \dot{x}_c A_2) \\
\dot{p}_3 &= \frac{\beta_{eff}(p_3)}{V_{3.0} + x_c A_3}(Q_3 - \dot{x}_c A_3)
\end{aligned} \tag{D.1}$$

$$\begin{aligned}
Q_1 &= n_1\, k_{v,c}\, x_{1h}\sqrt{|P_h - P_1|}\,\mathrm{sign}(P_h - P_1) + n_1\, k_{v,c}\, x_{1m}\sqrt{|P_m - P_1|}\,\mathrm{sign}(P_m - P_1) \\
&\quad + n_1\, k_{v,c}\, x_{1l}\sqrt{|P_L - P_1|}\,\mathrm{sign}(P_l - P_1) \\
Q_2 &= n_2\, k_{v,c}\, x_{2h}\sqrt{|P_h - P_2|}\,\mathrm{sign}(P_h - P_2) + n_2\, k_{v,c}\, x_{2m}\sqrt{|P_m - P_2|}\,\mathrm{sign}(P_m - P_2) \\
&\quad + n_2\, k_{v,c}\, x_{2l}\sqrt{|P_l - P_2|}\,\mathrm{sign}(P_l - P_2) \\
Q_3 &= n_3\, k_{v,c}\, x_{3h}\sqrt{|P_h - P_3|}\,\mathrm{sign}(P_h - P_3) + n_3\, k_{v,c}\, x_{3m}\sqrt{|P_m - P_3|}\,\mathrm{sign}(P_m - P_3) \\
&\quad + n_3\, k_{v,c}\, x_{3l}\sqrt{|P_l - P_3|}\,\mathrm{sign}(P_l - P_3)
\end{aligned} \tag{D.2}$$

$$m_{tot}\ddot{x}_c = F_c - F_L - F_{fric} \tag{D.3}$$

It is assumed that the change of the bulk modulus and the volume are so small it can be neglected. Furthermore the transmission line is disregarded to simplify the controller design. Lastly the Load force, F_L will be seen as a disturbance to the system.

The linearization of Eq. D.2 is done using a first order Taylor approximation which yields the results:

$$\begin{aligned}
\Delta Q_1 &= K_{qx_{1h}}\Delta X_{1h} + K_{qx_{1m}}\Delta X_{1m} + K_{qx_{1}l}\Delta X_{1l} + K_{qp1}\Delta P_1 \\
\Delta Q_2 &= K_{qx_{2h}}\Delta X_{1h} + K_{qx_{2m}}\Delta X_{2m} + K_{qx_{2l}}\Delta X_{2l} + K_{qp2}\Delta P_2 \\
\Delta Q_3 &= K_{qx_{3h}}\Delta X_{3h} + K_{qx_{3m}}\Delta X_{3m} + K_{qx_{3l}}\Delta X_{3l} + K_{qp3}\Delta P_3
\end{aligned} \tag{D.4}$$

Where the linearization constants are given as:

$$K_{qp,i} = \left.\frac{\partial Q_i}{\partial P_i}\right|_{x_{i,lin,0},P_{i,0}} = \sum_{i=1}^{3} -\frac{n_i k_{v,c} x_{i,lin,0}}{2\sqrt{|P_{lin} - P_{i,0}|}} \cdot sign(P_{lin} - P_{i,0}) \tag{D.5}$$

$$K_{qx,i} = \left.\frac{\partial Q_i}{\partial x_{i,lin}}\right|_{x_{i,lin,0},P_{i,0}} = n_i k_{v,c}\sqrt{|P_{lin} - P_{i,0}|} \cdot sign(P_{lin} - P_{i,0}) \tag{D.6}$$

The continuity equation is already linear considering the assumptions made and lastly the movement equation is linerised by ignoring the Coulomb friction and the load force disturbance.

$$\ddot{x}_c = \frac{1}{m_{tot}}(-P_1A_1 + P_2A_2 + P_3A_3 - B_c\dot{x}) \tag{D.7}$$

With the linearisation done a state space of the system can be set up. The equations of a state space system is given by Eq. D.8.

$$\ddot{\boldsymbol{x}} = \boldsymbol{A}\boldsymbol{x} + \boldsymbol{B}\boldsymbol{u} \tag{D.8}$$

$$\boldsymbol{y} = \boldsymbol{C}\boldsymbol{x} + \boldsymbol{D}\boldsymbol{u} \tag{D.9}$$

Where the matrices is given by the following:

$$\boldsymbol{A} = \begin{bmatrix} 0 & 1 & 0 & 0 & 0 \\ 0 & -B_c/M & -A_1/M & A_2/M & A_3/M \\ 0 & K_1 * A_1 & K_1 * Kqp1 & 0 & 0 \\ 0 & -K_2 * A_2 & 0 & K_2 * Kqp2 & 0 \\ 0 & -K_3 * A_3 & 0 & 0 & K_3 * Kqp3 \end{bmatrix} \tag{D.10}$$

Where $K_i = \dfrac{\beta_{eff}}{V_{i.0} - x_c A_i}$

$$\boldsymbol{B} = \begin{bmatrix} 0 & 0 & 0 & 0 & 0 & 0 & 0 & 0 & 0 \\ 0 & 0 & 0 & 0 & 0 & 0 & 0 & 0 & 0 \\ K_1 * Kqxh1 & K_1 * Kqxm1 & K_1 * Kqxl1 & 0 & 0 & 0 & 0 & 0 & 0 \\ 0 & 0 & 0 & K_2 * Kqxh2 & K_2 * Kqxm2 & K_2 * Kqxl2 & 0 & 0 & 0 \\ 0 & 0 & 0 & 0 & 0 & 0 & K_3 * Kqxh3 & K_3 * Kqxm3 & K_3 * Kqxl3 \end{bmatrix} \tag{D.11}$$

$$\boldsymbol{C} = \begin{bmatrix}1 & 0 & 0 & 0 & 0\end{bmatrix} \quad \boldsymbol{x} = \begin{bmatrix} x \\ \dot{x} \\ P_1 \\ P_2 \\ P_3 \end{bmatrix} \quad \boldsymbol{u} = \begin{bmatrix} x_{h1} \\ x_{m1} \\ x_{L1} \\ x_{h2} \\ x_{m2} \\ x_{l2} \\ x_{h3} \\ x_{m3} \\ x_{l3} \end{bmatrix} \quad \boldsymbol{D} = \boldsymbol{0} \tag{D.12}$$

When designing a LQC the goal is to find the control input signal, for a given system in order to minimize the a cost function by making the system states go to zero in an optimal manner.

The cost function of the LQC problem is seen in Eq. D.13.

$$J = x(t_1)^T \boldsymbol{S} x(t_1) + \int_{t_0}^{t_1} (x^T \boldsymbol{Q} x + u^T \boldsymbol{R} u + 2x^T dt \tag{D.13}$$

S, **Q** and **R** are symmetrical quadratic matrices that have to be at least positive semi-definite. This is true when $x^T \boldsymbol{A} \cdot x \geq 0$ for any $x \neq 0$.

By choosing the input u such that

$$\frac{d}{dt}(x^T \boldsymbol{P} x) = x^T \boldsymbol{Q} x + u^T \boldsymbol{R} u + 2x^T \tag{D.14}$$

and choosing $\boldsymbol{S} = \boldsymbol{P}(t_1)$ the cost function can be reduced to:

$$J_{min} = x(t_0)^T \boldsymbol{P}(t_0) x(t_0) \tag{D.15}$$

This matrix $\mathbf{P}$(t) has to satisfy the Riccati equation seen in Eq. D.16, solving the problem in a stationary case where $\bar{\boldsymbol{P}} = \lim_{t \to \infty} \boldsymbol{P}(t)$.

$$\boldsymbol{A}^T \bar{\boldsymbol{P}} + \bar{\boldsymbol{P}} \boldsymbol{A} + \boldsymbol{Q} - (\bar{\boldsymbol{P}} \boldsymbol{B}) \boldsymbol{R}^{-1} (\boldsymbol{B}^T \bar{\boldsymbol{P}} = 0 \tag{D.16}$$

The controller parameters **Q** and **R** are penalty matrices chosen by trial and error. Q penalizes the states and R penalizes the inputs. This results in the control input:

$$u = -\boldsymbol{R}^{-1} (\boldsymbol{B}^T \boldsymbol{P}) x = -\boldsymbol{K} x \tag{D.17}$$

The tracking result with a LQC can be seen in Figure D.1.

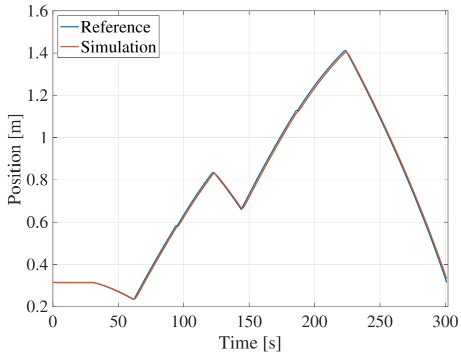

Figure D.1: LQC tracking result.

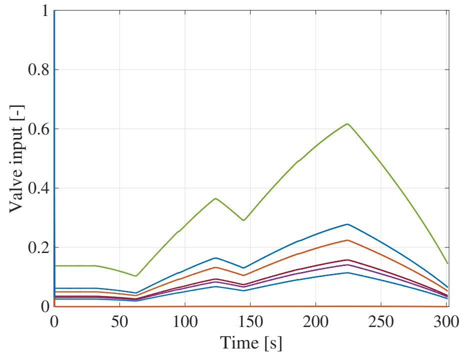

Figure D.2: LQC controller inputs.

As it can be seen the controller is able to track, however if looking at the inputs six valves are opening at the same time which was determined as undesired. Furthermore the inputs are continuous signal between 0 and 1 where the valves are operated as digital. Using only values of 0 or 1 could decrease the tracking and as it has not been able to penalize the opening of only one valve at a time using a LQC controller has been disregarded.